Max-Planck-Institut für Intelligente Systeme
(**ehemals Max-Planck-Institut für Metallforschung)**
Stuttgart

Microstructural Changes and Intermetallic Compound Formation in Metallic Bilayers

Paul J. Rossi

Dissertation
an der
Universität Stuttgart

Bericht Nr. 258
Oktober 2016

Microstructural Changes and Intermetallic Compound Formation in Metallic Bilayers

Von der Fakultät Chemie der Universität Stuttgart zur Erlangung der Würde eines Doktors der Naturwissenschaften (Dr. rer. nat.) genehmigte Abhandlung

vorgelegt von

Paul J. Rossi

aus Massenbachhausen

Hauptberichter:	Prof. Dr. Ir. E. J. Mittemeijer
Mitberichter:	Prof. Dr. J. Bill
Prüfungsvorsitzender:	Prof. Dr. Th. Schleid

Tag der Einreichung:	15.07.2016
Tag der mündlichen Prüfung:	25.10.2016

MAX-PLANCK-INSTITUT FÜR INTELLIGENTE SYSTEME
(EHEMALS MAX-PLANCK-INSTITUT FÜR METALLFORSCHUNG)
INSTITUT FÜR MATERIALWISSENSCHAFT DER UNIVERSITÄT STUTTGART

2016

Contents

Chapter 1

Introduction

Diffusion studies in metals are commonly limited to elevated temperatures, as the activation energy required for the operation of the atomic processes involved during the diffusion process are usually large. Upon lowering the temperature the atomic processes involved in the diffusion mechanism, i.e. vacancy or interstitial diffusion [1], are frozen in. Hence, at moderate and room temperature no measurable concentration gradients develop and diffusion phenomena cannot be observed. Values for the diffusion coefficients at room temperature have to be extrapolated from measurements done at higher temperatures. However, in some binary systems diffusion phenomena can already be observed at ambient temperatures [2], often leading to the nucleation and growth of intermetallic compounds (IMCs), see below. In these systems diffusion processes as well as the phenomena associated with it, i.e. IMC formation, are an interesting and viable field of research, also with respect to technical applications.

Different methods exist for the investigation of diffusion and the determination of the various diffusion coefficients in binary metallic systems [3]. In order to obtain partial or self diffusion coefficients, a thin layer of tracer material, either radioactive or consisting of a certain isotope, can be plated on a bulk sample. The sample is subsequently annealed and sectioned. The concentration of the tracer element can be analyzed in the different sections (i.e. by using a scintillation counter), producing a concentration gradient for the tracer element. In systems exhibiting concentration dependent diffusion coefficients, the Boltzmann-Mantano method can be used to obtain the diffusion coefficients as a function of concentration [4]. A bulk diffusion couple consisting of two "semi-infinite" end members is annealed for a specific time. Again the developing concentration profile can be obtained by sectioning methods or, alternatively, using electron probe micro analysis (EPMA). If inert markers are placed between the two end members the Darken's analysis [5] can be coupled with the Boltzmann-Mantano method to obtain the partial diffusion coefficients of the two elements. The method is based on the observations made by Smigelskas and Kirkendall [6], who discovered the Kirkendall-Effect. The effect strongly indicated that diffusion in metals takes place via vacancy movements. These methods, however, require that the diffusion process is "frozen in" annealing the specimens for a specific time, such

that Fick's second law can be used to obtain diffusion coefficients from the concentration profiles. This is usually realized by quenching the samples to room temperature. When systems exhibiting low-temperature diffusion are studied, a quenching procedure to very low temperatures is necessary to stop the diffusion process. This process is difficult to realize experimentally and in some cases even impossible due to phase transitions at lower temperatures (i.e. the α-Sn to β-Sn transition at about 13.2 °C [7]). In this case, in-situ techniques can be used to follow the diffusion process. Rutherford backscattering (RBS) or X-ray diffraction (XRD) are well suited methods for in-situ studies. However, XRD and RBS require that the samples used for the diffusion experiments are sufficiently thin in order that they can be penetrated by the particles or radiation used in these methods. Samples, composed of two thin metallic layers (i.e. metallic bilayers), which provide the concentration gradient for the interdiffusion, are therefore ideally suited for an in-situ study of the diffusion processes using XRD. The radiation can penetrate both layers and any IMCs that develop during the diffusion experiment will be represented in additional reflections occurring in the XRD patterns, while the amount of all phases can be determined from the intensity of the reflections. Diffusion coefficients can then be obtained from the growth rates of the IMCs.

As the properties of thin-films can be markedly different from their respective bulk materials [8, 9], they have become an important research field with entire scientific journals dedicated to this topic. The increased surface-to-bulk ratio of thin films increases the role of surfaces and interfaces of the films leading to mechanical effects [10, 11] or metastable phases [12] specific to thin films, which cannot be observed in the respective bulk materials. They are also well suited for in-situ diffusion studies due to their increased defect density compared to bulk materials, as these defects represent diffusional fast paths [13] greatly increasing the diffusion rates. Additionally, the small dimensions of thin films can emphasize the effects of the diffusional processes. If the diffusion distances are restricted to the Å- or nm-scale, either due to small diffusion coefficients or in the initial stages of the diffusion process, they are generally irrelevant in bulk materials, whereas they can already significantly alter the properties of thin film materials.

The use of thin films is widespread in technical applications, where they are used as optical coatings, protective layers or for decorative purposes. Metallizations in integrated circuits are often made of thin metallic films [14]. Especially at solder joints these metallizations come into contact with thin films of a different metal. Consequently, bilayer samples of thin metallic films are of great technological importance, providing insight to the processes occurring in the solder joints of integrated circuits.

Therefore, metallic bilayer samples were chosen for the present thesis in order to investigate interdiffusion and IMC formation.

1.1 Systems exhibiting low-temperature diffusion and IMC formation

Systems exhibiting low temperature diffusion are often composed of a combination of group 11 metals with group 13 or 14 metals. Such combinations are characterized by a relatively fast diffusion mechanism, enabled by interstitial diffusion of the noble metals in the group 13 or 14 metals [15]. The activation energy for interstitial diffusion is significantly lower compared to i.e. substitutional vacancy diffusion [13, 1, 3] and thus this diffusion mechanism can operate readily at room temperature. If a group 13 or 14 metal with a low melting point is used, large homologous temperatures (T/T_m, where T is the temperature and T_m is the melting point of the respective element) are obtained already at ambient conditions, further increasing the mobility the binary systems. The large diffusional fluxes coupled with the high mobilities in such systems promote IMC formation even at low temperatures, making such systems ideal candidates for the investigation of the kinetics of IMC formation at room and ambient temperatures. An overview of IMC formation in metallic bilayer samples of these systems can be found in Ref. [16].

Thin film diffusion couples of some of these systems have been extensively studied, as i.e. Au–Sn [17, 18, 19, 20], while only few publications focus on other systems like Ag–Sn and Ag–In. However, recently an increased interest has develop for the latter systems, as solders based on the Ag–Sn and Ag–In systems are one of the most promising candidates Pb-free solders (see below) [21, 22]. The combination of substitutional and interstitial diffusion in these systems, paired with the high mobility of the Sn and In atoms, represents an especially interesting case of interdiffusion and IMC formation at low temperatures [18]. Bilayers of both metals with varying thicknesses can also readily be prepared by physical vapor deposition (PVD) methods.

However, the only data available on IMC formation in Ag–Sn and Ag–In thin films is rather scarce ([23, 2, 24, 16] in case of the Ag–Sn system and [23, 2, 16, 25, 26, 27, 28] in case of the Ag–In system). Hence, bilayers based on the Ag–In and Ag–Sn systems were chosen for the investigation of low temperature diffusion and the kinetics of IMC formation in the present thesis.

1.2 Pb-free solders

In order to reduce the amount of toxic waste caused by electronic devices, the use of certain hazardous materials has since been restricted in their production by the European directive RoHS (Restriction of Hazardous Substances Directive) [29]. Amongst these materials is Pb, which immediately restricts the use of the classical Pb–Sn based solders. Therefore, replacements have to be found for Pb-Sn based solders. Solders based on

compositions near the low-melting temperature eutectic of the Ag–Sn system are the most promising candidates for Pb-free solders [30, 21, 31]. Ag–Sn based solders have a low melting point, good wetability and similar mechanical properties as the classical Pb-Sn solders [21, 32, 33, 31, 34]. The properties of the Ag–Sn based solder systems can be improved by ternary additions of In, which further lowers the melting temperature [35] and improves the wetability of certain surfaces [36]. Similar to the Ag-Sn system, a low-temperature eutectic is present in the Ag-In system which can be used as a basis for Pb-free solders [37, 38]. For some applications the Ag-In based solders are even more promising than the Ag-Sn based solders [22], as the melting point of the eutectic in the Ag–In system is even lower as compared to the Ag–Sn system [38].

As diffusion and IMC formation already takes place at ambient temperatures, which is where most of the solder joints operate, these processes can negatively influence the properties of the solder joints [39, 40, 41, 42]. IMCs that develop during storage of the solder joints can severely influence their bond strength [43, 44], leading to the failure of electronic devices. Since it has been shown that IMCs of the Ag–Sn and Ag–In systems readily form their respective Pb-free solders [45, 46, 22], scientific investigation of the kinetics of IMC formation and the diffusion processes in the Ag–Sn and Ag–In systems is required in order to bring the Pb-free solder technology on par with the Pb-free counterparts.

1.3 The Ag–Sn and Ag–In systems

The IMCs in both, the Ag–Sn and Ag–In systems, are sometimes referred to as Hume-Rothery electron compounds [47, 48]. These Hume-Rothery electron compounds occur in alloys of the metals Cu, Ag and Au. A certain sequence of crystal structures is observed according to the concentration of valence electrons per atom. The basic theory suggests that a certain phase with a specific crystal structure is stable until the Fermi surface comes into contact with the Brillouin zone of that structure [49, 50, 51]. When this happens the structure becomes unstable and another phase with a different structure forms. Therefore, a similar sequence of structures can be observed for certain binary systems as a function of their electron concentration [47, 48].

1.3.1 Ag–Sn

An early version of the Ag–Sn phase diagram was published by Petrenko [53]. Due to some inconsistencies in the work by Petrenko [53], Murphy [54] reinvestigated the Ag–Sn system, and published a revised phase diagram, which remains the commonly accepted version for the Ag–Sn system to this day.

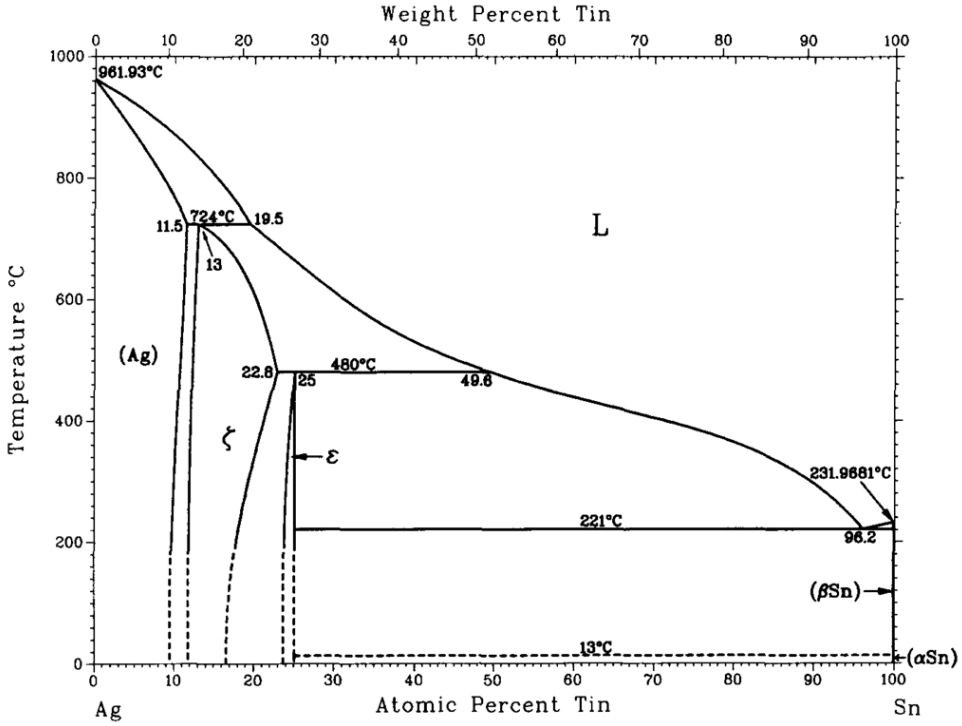

Fig. 1.1: Phase diagram of the Ag–Sn system, reproduced from Ref. [52] with permission of Springer. Two IMCs are present at room temperature. Pb-free solders are based on the low temperature eutectic of the system.

Two IMCs are present at room temperature, Ag_4Sn and Ag_3Sn (see Fig. 1.1). The crystal structure of Ag_4Sn is a hexagonal closed packed (hcp) Mg-type structure [51]. Ag_4Sn has a wide homogeneity range, especially at higher temperatures. Unlike the Ag_4Sn IMC, Ag_3Sn has a narrow homogeneity range of about 1 at.% at room temperature [54].

Preston [55] also claimed a hcp-type structure for Ag_3Sn. However, Nial, Almin, and Westgren [56] first showed that Ag_3Sn has an orthorhombic crystal structure, its unit cell can be obtained from the Mg-type hcp unit cell by an orthorhombic distortion. Burkhardt and Schubert [57] first classified the two types of distortion as λ-type ($2c/b > \sqrt{3}$) distortion and ϰ-type ($2c/b < \sqrt{3}$) distortion, where b and c denote the axis of the orthorhombic unit cell. The same authors also suggested that Ag_3Sn should have an ordered crystal structure, based on its similarity with Cu_3Ge. Fairhurst and Cohen [58] were the first to observe superstructure reflections of Ag_3Sn, which are particularly difficult to observe due to the similar atomic scattering factors of Ag and Sn [59]. A λ-type distortion of the unit cell was obtained. On the contrary, no superstructure reflection were observed in Ref. [60] and additionally a ϰ-type distortion of the unit cell was observed. Most recently Rietveld refinements done by Rönnebro, Yin, Kitano, Wada, and Sakai [61] showed that the unit cell of Ag_3Sn has a ϰ-type orthorhombic distortion. For the

refinements an ordered structure of Ag_3Sn was used, most likely based on the structure published by Fairhurst and Cohen [58]. Superstructure reflections were not shown and the crystal structure of Ag_3Sn was not discussed. As the Ag_3Sn IMC readily forms in Ag-Sn diffusion couples [23] and diffusion couples [39] knowledge of the correct crystal structure of the IMC is extremely important. Against this background high-resolution XRD coupled with Rietveld refinement was used to redetermine the crystal structure of Ag_3Sn.

Two peritectics and one eutectic are present in the system, the eutectic is present at 221 °C and 96.2 at.% Sn [52]. Ag has a relatively high solubility for Sn, about 10 at.% at room temperature, while Sn has basically no solubility for Ag. Sn diffuses substitutionally in Ag [62] with a relatively high activation energy of about 165 kJ mol^{-1}. The substitutional diffusion of Ag in Sn has a much smaller activation energy of about 51 kJ mol^{-1}.

1.3.2 Ag–In

In case of the Ag-In system several phase diagrams have been published in literature. The phase diagrams are mostly based on the early work published by Weibke and Eggers [63] and the work later published by Campbell, Wagemann, and Ferguson [38]. Weibke and Eggers [63] found three different IMCs present at room temperature, however, the published phase diagram contradicts thermodynamic principles (no alternating single- and two-phase regions at constant T). The compositions of the two Ag-rich IMCs were determined as roughly corresponding to Ag_3In and Ag_2In. The crystal structure had previously been determined to be a hcp Mg-type [64] structure. The composition of the third In-rich IMC was reported to be close to 75 wt.% In. Hellner and Laves [65] determined the crystal structures of the remaining IMCs at room temperature, thereby establishing the composition of the In-rich compound to correspond to $AgIn_2$. The results are presented in Refs. [65] and [66]. Complex ordered structures were observed for Ag_2In (cubic Cu_9Al_4-type) and $AgIn_2$ (tetragonal Al_2Cu-type) at room-temperature. A revised phase diagram based on these results is shown in Ref. [65]. Campbell et al. [38] reinvestigated the Ag–In system and claimed that an additional IMC is present at room-temperature with an ordered cubic Cu_3Au-type structure. They published an additional phase diagram including this α' IMC. The existence of the α' IMC has so far not been observed in other publications. Hellner and Laves [65] found high- and low-temperature modifications for the Ag_3In and Ag_2In IMCs, the phase transitions were thought to be of an order-disorder transition. These phase transitions were basically confirmed in Refs. [67] and [68]. However, Satow, Uemura, and Yamakawa [68] found that in case of Ag_2In the transition is not of order-disorder type, they determined the structure of the

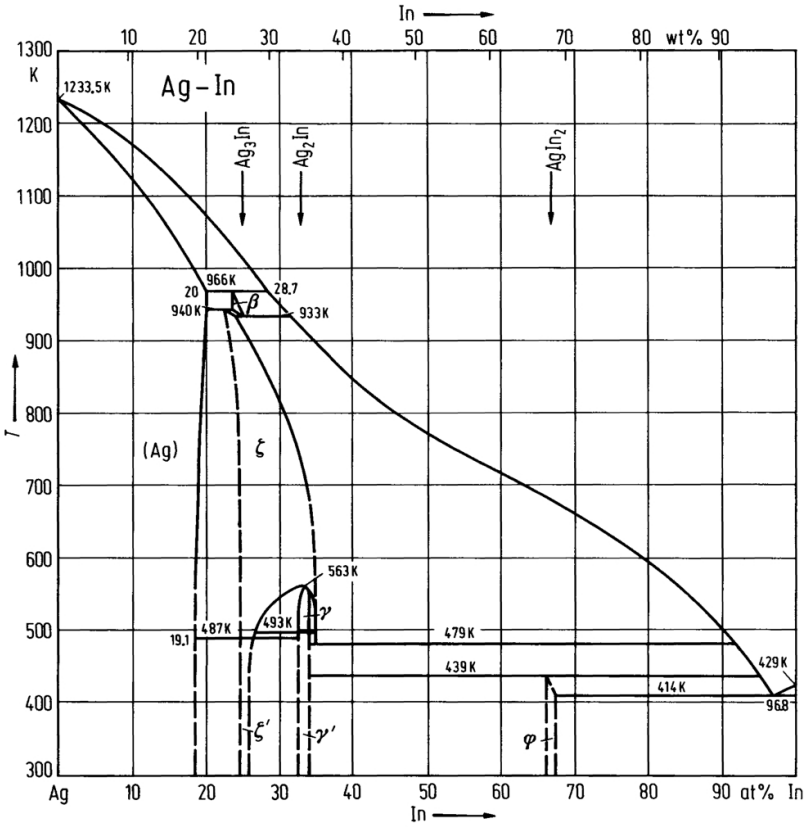

Fig. 1.2: Phase diagram of the Ag–In system, reproduced from Ref. [69] with permission of Springer. Three IMCs are present at room temperature. Pb-free solders are based on the low temperature eutectic of the system.

high-temperature phase as Cu_5Zn_8 γ-brass type. Fig. 1.2 shows the phase diagram as published in [69], which is primarily based on Refs. [63, 65, 66, 67, 68]. As in case of the Ag-Sn system, Ag has a relatively high solubility for In (about 18 at. % at room temperature [70]), while In has practically no solubility for Ag. At room temperature all IMCs have a narrow homogeneity range. The diffusion mechanism are also similar to the Ag–Sn system, Ag diffuses interstitially in In with an activation energy of 54 kJ mol^{-1} [71], while In diffuses substitutionally in Ag with an activation energy of 170 kJ mol^{-1} [72]. A low temperature eutectic is present in the Ag–In phase diagram at 96.8 at. % and 141 °C. Additionally two metatectic reactions occur in the Ag-In system (281 °C and 660 °C [73]), which exhibit the peculiar effect of remelting of an already solidified compound upon lowering the temperature.

1.4 Interdiffusion and IMC formation

Upon nucleation of an IMC in a diffusion couple additional interfaces are created, which are associated with an interfacial energy. The interfacial energy creates a nucleation bar-

rier that has to be overcome before a stable nucleus of an IMC can form. The nucleation barrier can further increase by misfit strains associated with the nucleation process. A discussion of the classical nucleation theory and the nucleation barrier can be found in Ref. [74]. Due to the nucleation barrier, a supersaturation of one of the terminal layers in the diffusion couple is necessary before a stable nucleus of an IMC can form. The supersaturation provides the driving force to overcome the nucleation barrier.

The supersaturation of the terminal layers develops by interdiffusion. Intermixing due to diffusion is therefore a prerequisite before any IMCs can nucleate in a given diffusion couple. A more complete discussion of the matter is given in Ref. [75].

If an IMC eventually nucleates, its growth can proceed by diffusion of the elemental 2 components in IMC. Two growth modes are basically possible [76], distinguished by a different increase of the amount of the IMC as a function of time. Adopting a layer-like growth of the IMC between the two terminal layers, the two regimes can be distinguished depending on the thickness of the IMC layer. As long as the IMC layer is sufficiently thin, the supply of the components necessary for the growth of the IMC is greater than their rate of consumption by the reactions at the interfaces of the IMC layer. A so-called interface-controlled growth holds, where the amount of the IMC increases linearly as a function of time. Upon increasing thickness of the IMC layer, the diffusional flux through the IMC layer will also decrease. Eventually the rate of formation of the IMC at the interfaces becomes faster than the components necessary for the reaction can be supplied by diffusion. IMC formation is now diffusion-controlled and its amount increases as a function of the square root of time. Between the aforementioned growth modes a more or less extended transition occurs, where IMC formation is controlled simultaneously by the reactions at the interfaces as well as the diffusional processes (mixed mode).

If more than one IMC is present in a given system the question arises which of these compounds is the first to form in a diffusion couple. Walser and Bené [77] presented a rule for transition metal-semiconductor systems stating that at low temperatures the first phase to form is the "highest melting temperature congruently melting phase adjacent to the low-temperature eutectic". This rule was expanded by Bené [78] for low temperature IMC formation in metal-metal systems, where the rule states that the "phase immediately adjacent to the low-temperature eutectic" is the first phase to form. The rules from Refs [77, 78] are based on semi-empirical considerations, nucleation barriers account for the differences between both rules. Pretorius, Marais, and Theron [79] present a so-called EHF (Effective Heat of Formation) model, which assumes that in a diffusion couple an interfacial layer of a certain concentration develops. The concentration is assumed to be the liquidus minimum of the system. Due to the different concentrations of the IMCs in a given system, the amount of IMC that can form out of the interfacial layer differs

for every compound. The total energy release upon nucleation of the respective IMCs is determined from the combination of the amount of IMC that can nucleate from the interfacial layer and its respective Gibbs energy of formation. The IMC which leads to the greatest energy release upon nucleation, i.e. "heat of formation", is assumed to form first. Apart from the above mentioned rules and models other thermodynamic considerations should be taken into account. In view of the diffusion that is required before an IMC can nucleate, nucleation of the IMCs from solid solutions of the respective elements of the diffusion couple should also be considered. In case of the absence of mutual solubilities, IMC formation can be considered from the respective pure elements, while simultaneously recognizing in which of the elemental layer IMC formation occurs. Such considerations, which have been lacking so far, will be applied to IMC formation in the Ag–Sn and Ag–In bilayer specimens.

However, which IMC is the first that can be observed in a given diffusion couple is not only controlled by thermodynamics, but may also be governed by kinetic restrictions. Based on such kinetic consideration by Geguzin, Kaganovskiy, Paritskaya, and Solunskiy [80], Gösele and Tu [76] have derived a model for IMC formation in binary diffusion couples. Their results show that in the early stages of IMC formation, where IMC formation is interface-controlled (see above) only one compound may exist. The model predicts that compounds, which are preferentially observed in this stage, are kinetically stable, having wide homogeneity ranges and large reaction rates at the interfaces of their respective layers. The formation of a possible second IMC is kinetically suppressed in this stage, due to the different growth rates of the IMCs. Only if IMC formation becomes diffusion-controlled and additionally a critical thickness is surpassed the second IMC can form. A specific property of thin films diffusion couples is that one of the terminal layers might already be consumed before the transition to diffusion-controlled growth occurs. Hence not all phases as predicted by the phase diagram occur simultaneously in thin-film diffusion couples as opposed to bulk diffusion couples [81, 82].

In case of the Ag-In system $AgIn_2$ was the first IMC to be observed during room temperature aging in thermally evaporated Ag-In bilayers [23, 2, 25]. Until now only diffusion-controlled growth of the $AgIn_2$ IMC was observed in evaporated bilayers [23, 2, 25, 26], as well as electro-deposited bilayers [27, 28]. In samples containing Ag in excess to In, the Ag_2In IMC was eventually observed after prolonged aging [23, 2]. In case of Ag-Sn thin-film bilayer samples only Ag_3Sn was observed during aging at room temperature and [23, 2, 24]. Diffusion-controlled growth of the Ag_3Sn IMC was observed. Ag_4Sn is only observed in diffusion couples at higher temperatures [83].

However, no explanations have been given as to why $AgIn_2$ and Ag_3Sn are the first IMCs to appear in their respective thin-film diffusion couples and no explanations for the

sequence of IMC formation were given. Furthermore, time-resolution was relatively low in the previous works, which hindered the determination of the prevailing growth modes. Additionally, the amount of IMC was usually plotted against the square root of time in order to determine if diffusion-controlled growth prevails. Such a procedure should be avoided as for such a plot the knowledge of the start of the diffusion experiment ($t = 0$) is necessary. This point of time is often unknown if IMC formation occurs already during preparation or measurements of the specimens. Furthermore, if a different growth mechanism occurs before the diffusion-controlled growth of the IMC, $t = 0$ is only hypothetical and only available by a suitable extrapolation. When, using a plot of the squared amount of IMC against aging time to knowledge of $t = 0$ is not necessary. Such plots and should always be preferred for determining if a diffusion controlled growth prevails. Due to the relatively low time resolution of the previous works, the course of IMC formation immediately after specimen preparation remains unknown. If interface-controlled growth prevails in the diffusion couples, it can be expected to occur in the initial stages of aging and might be missed if the time resolution is too low. Against this background the kinetics and sequence of IMC formation was investigated in Ag–In and Ag–Sn thin-film bilayer samples. The results are discussed using kinetic as well as thermodynamic arguments.

In order to improve the time resolution, IMC formation was followed by XRD using a specialized setup consisting of a rotating anode X-ray tube in combination with a 2-dimensional detector (See below). This setup allowed for precise time-resolved measurements and considerably decreased the recording times for the XRD patterns. Hence XRD pattern are available almost directly after preparation of the bilayers. The fast recording time and high time resolution enables the possibility to reveal any growth regimes of the IMCs that were missed until now and allows investigation of the precise sequence of IMC occurring in the Ag–In and Ag–In bilayer samples.

The interdiffusion coefficients that have been determined for the Ag-In system (see Tab. 1.1) in the previous works were obtained using only simplified calculations [2], using only the initial thicknesses of the layers in combination with the reaction times. A regression analysis, including the individual data points was not done and concentration gradients in the specimens were not taken into account. Roy and Sen [25] applied models to the Ag–Sn system, which are strictly valid only for systems exhibiting complete miscibility. In this case the nature of the obtained diffusion coefficients, i.e. whether they are partial or interdiffusion coefficients, is not clear.

Therefore, interdiffusion coefficients were redetermined from the time and temperature resolved XRD measurements of the Ag–In bilayers. The obtained data points were fitted using appropriate models for IMC formation [84], taking into account the developing

Table 1.1: Overview of the published interdiffusion coefficients D and the associated activation energies Q for the Ag–In system.

	Process	D [$cm^2\ s^{-1}$]	Q [$kJ\ mol^{-1}$]
[2]	Ag_2In interdiffusion	$1.1 \cdot 10^{-16}$ at RT	-
[28]	Ag_2In interdiffusion	$4.6 \cdot 10^{-11}$ at 150 °C	-
[2]	$AgIn_2$ interdiffusion	$1.7 \cdot 10^{-15}$ at RT	-
[26]	$AgIn_2$ interdiffusion	$4.9 \cdot 10^{-13}$ at RT	44.4
[28]	$AgIn_2$ interdiffusion	$5.3 \cdot 10^{-13}$ at RT	44.4
[25]	Ag–In diffusion	$1.1 \cdot 10^{-16}$ at RT	41.5
[25]	Ag–In diffusion (grain boundary)	$3.9 \cdot 10^{-11}$ at RT	32.8

Note that in case of Ref. [25] it is not clear to which type of diffusion process is meant, as inappropriate models were used for the calculation of the diffusion coefficients.

concentration gradients, allowing for the calculation of reliable interdiffusion coefficients in the Ag–In system.

1.5 Thermal Evaporation and Magnetron Sputtering

The thin-film bilayer samples used in this work have been prepared by Physical Vapor Deposition Methods (PVD). Two different methods (i.e. thermal (resistance) evaporation and magnetron sputtering) were used, in order to compare the effect of deposition method on interdiffusion, IMC formation and the microstructure of the bilayer samples.

Growth of the thin films in PVD processes takes places by condensation out of the supersaturated vapor phase, when atoms or molecules condense onto the substrates. The condensed particles are mobile on the substrate surface and can form clusters of varying sizes. Clusters smaller than a certain critical size will shrink as they increase the Gibbs free energy of the model system due to the associated surface and interfacial energies, while clusters larger than the critical size become stable nuclei and decrease the Gibbs free energy of the system. The process is similar to the classical nucleation theory (cf. 1.4), a thermodynamic description of this process is available from the the capillarity theory [8]. The theory offers a relation of the effect of deposition rate and temperature on the nucleation process and the resulting microstructure.

Upon further growth the microstructure of PVD-layers is strongly determined by the homologous temperature (T/T_m, where T_m is the melting temperature) of the substrate

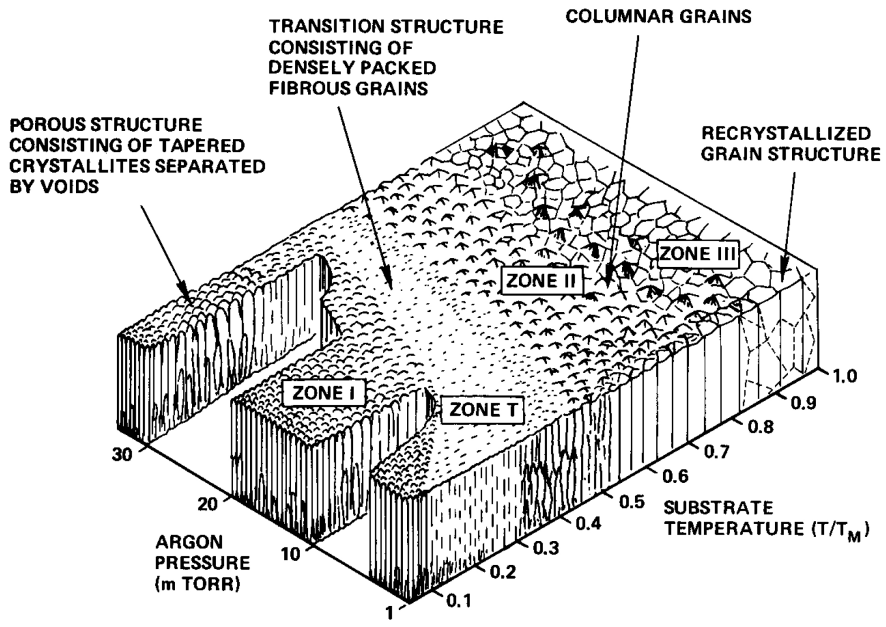

Fig. 1.3: Structure zone model for magnetron sputtered thin films according to Thornton [85], showing the microstructures of the thin films as function of the homologous temperature and the sputtering gas pressure. Reproduced from [85], with the permission of the American Vacuum Society.

during deposition of the layers. The homologous temperature determines the mobility of the atoms of the respective film materials and thereby greatly influences the microstructure of the layers. On this basis, so-called structure zone models have been developed for the microstructure of PVD-layers, defining different structure zones according to the homologous temperature [86, 87, 88]. Each structure zone exhibits a distinct microstructure of the film. The most well known structure zone model, shown in Fig. 1.3, has been published by Thornton [87] for magnetron sputtered films. At low homologous temperatures in zone 1, the mobility of the adatoms on the growing film surface is low and shadowing processes dominate the microstructure. A porous layer with small tapered crystallites develops. At higher temperatures the transition zone T is reached, where surface diffusion processes become active. The pores are partially filled by the diffusing atoms resulting in a more dense layer of fibrous grains. In zone 2 the temperature is high enough for bulk diffusion processes to become active. The shadowing processes are overcome and a dense microstructure consisting of columnar grains results. At the highest temperatures in zone 3 grain growth and recrystallization dominates the structure, resulting in films with coarse and equiaxed grains. Increasing the pressure of the sputtering gas reduces the kinetic energy of the sputtered particles and therefore shifts the respective zones to higher temperatures. Very similar structure zone models have been published for evaporated layers, see e.g. Ref. [88].

Although the processes and the developing microstructures of evaporated and magnetron sputtered layers are similar, marked differences can exist in the microstructures of the respective layers [89, 90, 91]. A major difference between both processes is the kinetic energy of the particles in the vapor phase. The kinetic energy of magnetron sputtered atoms can be as high as several eV, which is up to two magnitudes larger compared to thermal evaporation [92]. Furthermore up to 1 % of the sputtered particles are ionized, whereas in thermal evaporation only about 0.1 % are ionized [93]. The ionized particles can be accelerated towards the substrate in the applied electric field in the DC sputter processes and impinge on the surface of the substrate and the growing films with very high kinetic energies [94]. Consequently the energy transferred to the substrate and the growing films during magnetron sputtering is considerably larger than in thermally evaporated films. This can induce defects in the growing films, which can act as nucleation sites. The nucleation process in sputtered films is therefore more random as compared to evaporated films, producing only weakly- or non-textured films. Additionally, some of the sputtered target material is already present as clusters of up to 7 atoms [93] in the vapor phase. These impinging clusters could basically already be above the critical nucleus size [93, 8], further facilitating the nucleation process and leading to less textured films. Evaporated layers, on the other hand, often exhibit strong fibre textures [90, 95], as the selective nucleation process promotes the nucleation of grains with the most-densely packed planes, having the lowest surface energy [96, 97], parallel to the substrate.

These differences in both processes can be expected to effect the formation of IMCs as well as the diffusion processes in thin-film bilayer couples. Although several articles exist discussing the effect of deposition methods on the microstructure of single layers (see i.e. [89, 90, 91, 92]), publications dealing with their effect on interdiffusion and IMC formation are relatively scarce. Against this background the effect of deposition method on interdiffusion and IMC formation was investigated in the Ag–Sn bilayer thin-film specimens.

1.6 Characterization Methods

1.6.1 Phase analysis

A variety of methods is available in order to investigate the kinetics of IMC formation in thin-film specimens, i.e. resistivity measurements can be used to follow he development of a given phase in a thin films specimen. However, only the amount of the given phase is available from resistivity measurements and a second method is necessary in order to identify the phases occurring in the samples [98]. Similarly, electron microscopy can be

used to determine IMC layer thicknesses from cross-section of thin film specimens, again a second method is necessary for phase identification [99]. Rutherford backscattering (RBS) provides information on the amount as well as the compositions of the individual phases in a given thin-film specimen [18]. However, analysis of the RBS spectra is not trivial. XRD, on the other hand, is a method which can be used to simultaneously obtain information on the amount as well as the type of IMCs present in a thin film specimen. The crystal structure of the phases is obtained from the various reflections in the XRD patterns, while the amount of the different phases is available from the integrated intensities of their respective reflections [2]. Additionally, microstructural information is available from the shape and the relative intensities of the reflections in the XRD patterns. The use of thin films ensures that the X-ray penetration depth is greater than the cross-section of the specimens, ensuring that all phases present in the specimen occur in the XRD patterns.

Hence, XRD was used as the main experimental method to identify the phase composition and development of the IMCs in the bilayer samples. The kinetics of IMC formation were available from the course of the integrated intensities of the reflections of the corresponding phases as a function of time. In order to improve the time resolution and to reduce the acquisition time of the XRD patterns, compared to previous works, a 2 dimensional VÅNTEC-500 2D detector was used. The 2 dimensional detector was combined with a rotating Cu-Kα X-ray source in a Bruker Turbo X-ray Source (TXS) diffractometer as shown in Fig. 1.4. A Xenocs Fox 2D collimating mirror was used in to obtain a monochromatic parallel X-ray beam. The setup produces a X-ray beam of high brilliance, restricted to a relatively small spot. This ensures a high resolution of the 2 dimensional XRD patterns, compared to previous studies. Temperature resolved measurements were carried out using a BTS heating stage (MRI Physikalische Gerärte GmbH, Karlsruhe, Germany) equipped with a X-ray transparent Be-dome that can be evacuated using a turbomolecular pump.

In order to redetermine the crystal structure of the Ag_3Sn IMC, high-resolution XRD patterns were recorded with a Philips (PANalytical) MPD diffractometer operating in Bragg-Brentano geometry using Cu-Kα_1 radiation. A X'Celerator linear position sensitive detector (PSD) was used to obtain high quality XRD patterns with a good signal-to-background ratio, necessary to investigate the possible presence of superstructure reflections of very low intensity. Monochromatic radiation was obtained using a (111) curved Ge single crystal Johannson monochromator placed in the incident beam (see Chapter 12 of Mittemeijer and Welzel [100]).

The structure of the Ag_3Sn IMC was determined from the XRD patterns using the Rietveld method [101]. Unlike in other refinement methods, where only integrated intensities of the XRD reflections are used, the Rietveld method uses all points present in

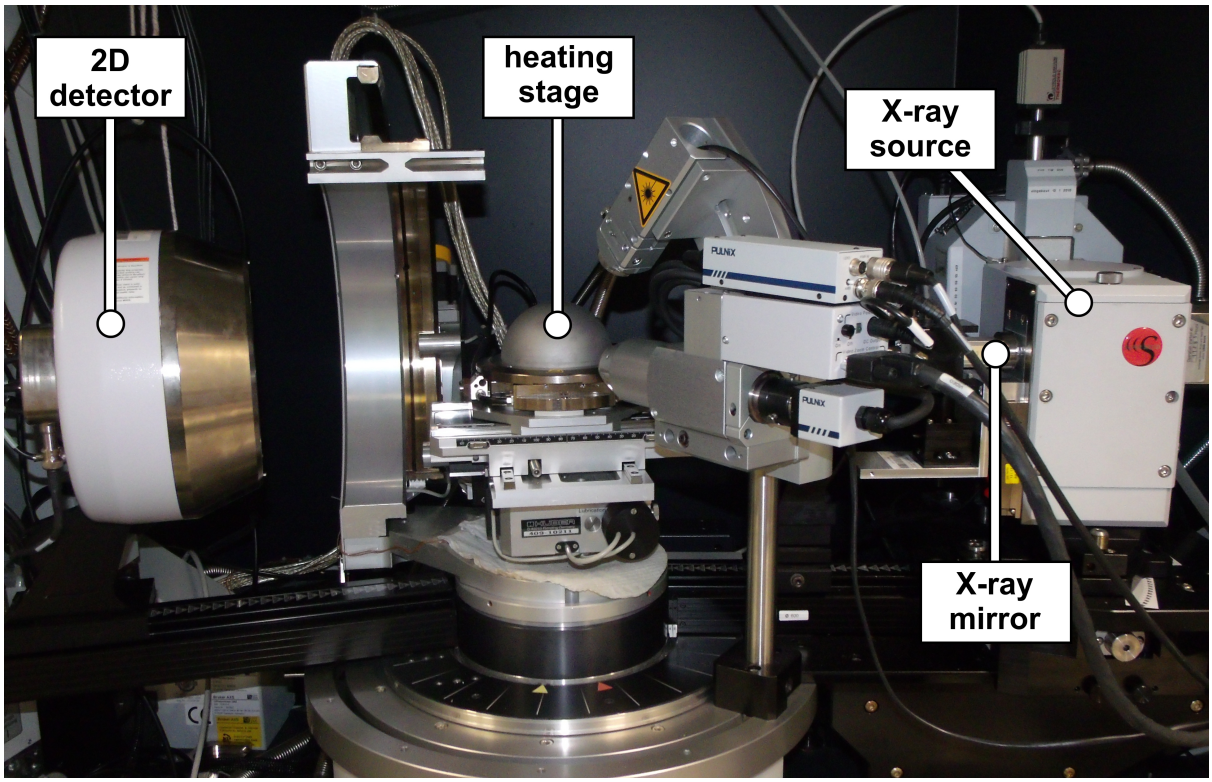

Fig. 1.4: Experimental setup of the Bruker TXS diffractometer. A 2 dimensional (2D) detector is used in connection with a rotating anode X-ray source, for fast acquisition times. Samples are mounted to a heating stage equipped with a Be-dome for the temperature-resolved measurements. A X-ray mirror is used for monochromatization and beam-shaping-

the step-wise recorded XRD pattern. This enables the determination of a larger amount of refinement parameters from the XRD patterns. In the Rietveld method the observed intensity $Y_{\mathrm{obs,i}}$ at the point i is calculated according to [100]:

$$Y_{\mathrm{calc,i}} = \sum_{\mathrm{ph}=1}^{\mathrm{phases}} \left(S_{\mathrm{ph}} \sum_{hkl(\mathrm{ph})} \left(K_{hkl(\mathrm{ph})} |F_{hkl(\mathrm{ph})}|^2 \Phi_{hkl(\mathrm{ph})} \Big(2\theta_i - 2\theta_{hkl(\mathrm{ph})} \Big) \right) \right) + b_i(obs). \quad (1.1)$$

The first sum contains all phases contributing to the XRD pattern and the second sum runs over all reflections of the corresponding phase, ph. S_{ph} is the scaling factor proportional to the relative amount of the phase in the sample. $K_{hkl(\mathrm{ph})}$ contains several corrections factors for the intensities of the reflections, as i.e. Lorentz-polarization factor, multiplicity factors and absorption corrections. $F_{hkl(\mathrm{ph})}$ is the structure factor of reflection hkl of phase ph and $\Phi_{hkl(\mathrm{ph})}(2\theta_i - 2\theta_{hkl(\mathrm{ph})})$ is the value of the profile function describing the peak shape relative to the position of the Bragg reflection $(2\theta_i - 2\theta_{hkl(\mathrm{ph})})$. $b_i(obs)$ is the value of the contribution of the background at position i. The individual components in Eq. 1.1 are functions of refineable model parameters, which can be obtain by minimization of the sum:

$$\sum_{i=0}^{n-1} \left(w_i (Y_{\mathrm{obs,i}} - Y_{\mathrm{calc,i}})^2 \right), \quad (1.2)$$

where w_i are weighting factors. Mathematically the minimum is found from the first derivative of Eq. 1.2, where $Y_{\mathrm{calc,i}}$ is approximated by a Taylor series. The procedure results in a set of normal equations, which is usually solved using the Levenberg-Marquardt algorithm [102, 103]. The structure factors $F_{hkl(\mathrm{ph})}$ and the position of the Bragg reflection contain the parameters describing the crystal structure of the respective phase, thus enabling crystal structure refinement and/or determination with the Rietveld method.

1.6.2 Microstructure

It is to be expected that interdiffusion and IMC formation alter the microstructure of the bilayer specimens. Additionally, a microstructural characterization of the bilayer specimens was necessary in order to reveal the effect of different deposition methods on the microstructure of the bilayers (see Section 1.5). However, due to the small dimensions in the thin-film bilayer specimens, light optical methods are only of limited used. Electron microscopy and focused ion beam (FIB) techniques are necessary in order to investigate the microstructure of the bilayer specimens. Scanning electron microscopy (SEM) as well as FIB were used in order to reveal the microstructure of the surface and grain size of the

thin-films. Especially the grain size is easily accessible using FIB due to the channeling-contrast of the method. Moreover, the combination of a Ga-ion beam (FIB mode) with a electron beam (SEM mode), in a so-called dual-beam or cross-beam instrument, combines the milling capability of the Ga-ion beam with the high-resolution imaging capabilities of the electron beam (SEM mode). This allowed for the in-situ preparation and imaging of cross-sections during aging of the bilayer specimens.

The microstructure of individual grains, as well as their composition and orientation were investigated using transmission electron microscopy (TEM) and energy dispersive X-ray spectroscopy (EDX). The cross-sectional TEM samples of the bilayer specimens were prepared, using the lift-out technique [104], with the Ga-ion beam (FIB) of the dual-beam microscope.

Pole figures of the individual sublayers of the bilayer specimens were recorded using XRD, in order to reveal their respective microstructure.

Chapter 2

Dependence of Intermetallic Compound Formation on the Sublayer Stacking Sequence in Ag–Sn Bilayer Thin Films

P.J. Rossi[1], N. Zotov[1], E. Bischoff[1] and E.J. Mittemeijer[1,2]

[1] *Max Planck Institute for Intelligent Systems (formerly Max Planck Institute for Metals Research), Heisenbergstraße 3, D-70569 Stuttgart, Germany*

[2] *Institute for Materials Science, University of Stuttgart, Heisenbergstraße 3, D-70569 Stuttgart, Germany*

Abstract

Intermetallic compound (IMC) formation in thermally-evaporated Ag–Sn bilayer thin films has been investigated employing especially X-ray diffraction (XRD) and (S)TEM methods. The specific IMCs that are present in the as-deposited state depend sensitively on the stacking sequence of the sublayers. In case of Sn on top of Ag, predominantly Ag_3Sn is formed, whereas Ag_4Sn is predominantly present in the as-deposited state for Ag on top of Sn. In the latter case this is accompanied by an extremely fast uptake of a large amount of Sn by the Ag sublayer, leaving behind macroscopic voids in the Sn sublayer. The results are discussed on the basis of the thermodynamics and kinetics of (IMC) product-layer growth in thin films. It is shown that both thermodynamic and kinetic arguments explain the contrasting phenomena observed.

2.1 Introduction

The introduction of the European directive ROHS (Restriction of Hazardous Substances Directive) [29] prohibits the further use of Pb-based solders in electrical and electronical equipment. Pb-free solders based on the Ag–Sn, Ag–Sn–In, Ag–Sn–Cu and Ag–Sn–Bi systems are promising candidates for substitution of the classical Pb–Sn solders [32, 33,

21, 31], since they have a low melting point and good wettability, as well as mechanical properties comparable to those of the classical Pb–Sn solders [34].

Development of intermetallic compounds (IMCs) upon soldering can greatly influence the properties and lifetime of solder joints [39, 40, 41, 42]. Two IMCs have been identified in the Ag–Sn system [54], Ag_3Sn, with a narrow homogeneity range of about 1 at.% (between 24 at.% Sn and 25 at.% Sn) at room temperature (RT), and Ag_4Sn, with a homogeneity range of about 5 at.% (between 13 at.% Sn and 18 at.% Sn) at RT [54]. Ag can dissolve a considerable amount of Sn; the solubility limit at RT is about 10 at.% [52], whereas Sn has practically no solubility for Ag at RT [54]. Ag diffuses in Sn by an interstitial mechanism [105, 15], whereas Sn diffuses substitutionally in Ag [62] and thus the diffusion coefficient for the latter process is relatively small [72]. IMC Interdiffusion coefficients are large at RT: a value of $D = 6.6 \cdot 10^{-16}$ cm^2s^{-1} has been obtained for the Ag_3Sn phase [2]. This diffusion coefficient is much larger as compared to the diffusion coefficient for substitutional Sn diffusion in Ag [72] and comparable to the diffusion coefficient for interstitial Ag diffusion in Sn [105]. Therefore, it may be expected that interdiffusion can lead to IMC formation even at RT. Consequently, knowledge of the evolution of IMCs and the corresponding microstructure at RT is of particular importance in view of a possible long-term stability of Ag–Sn based solder joints.

A few papers on the RT aging of evaporated Ag–Sn bilayers have been published [24, 2, 16, 23]. In these early works only the formation of Ag_3Sn was reported.

The main goal of the present study is the investigation of IMC formation in Ag–Sn thin films in the as-deposited state in more detail. In particular, it will be shown that the stacking order of the sublayers controls which IMC is formed.[1] This peculiar observation is discussed and explained in terms of the thermodynamics and kinetics associated with phase formation in this system.

2.2 Experimental Procedures

2.2.1 Specimen preparation

Thermally evaporated Sn–Ag bilayer films were prepared using a Lesker Nano 36 machine. The materials Ag (purity: 99.99 wt.%, Lesker) and Sn (purity: 99.999 wt.%, Heraeus) were placed in separate evaporation boats, made of Mo in the case of Sn evaporation and made of W in the case of Ag evaporation. Single crystalline Si (100) wafers, covered with an amorphous 50 nm SiO_2 layer, were used as substrates for all evaporated bilayers.

[1] In case of IMC formation in Au–Sn bilayers a similar dependence on sublayer stacking sequence was observed [106], which was explained as a consequence of oxide formation. Such trivial origin, for the effect observed, can be excluded in the present case (see Section 2.2.1).

The substrates were ultrasonically cleaned in acetone and subsequently in isopropanol; cleaning was done for 20 min in each solvent. Next, the substrates were placed in a solution of 1 part of 32 wt.% H_2O_2 and 2 parts of 96 wt.% H_2SO_4 [107]. The solution was heated until the boiling point was reached, and kept at this temperature for about 20 min. Afterwards, the substrates were rinsed with demineralized water and dried in a flow of nitrogen gas. As last step of the cleaning procedure, the substrates were cleaned in an oxygen plasma for 10 min. The substrates were fixed on a rotatable substrate holder. The substrates on the holder were placed at a distance of approximately 35 cm from the evaporation sources. Rotation speed of the substrate holder was about 30 rpm. Depositions were carried out at pressures between 0.6×10^{-5} Pa and 2.6×10^{-3} Pa. The Sn layers as well as the Ag top layers were deposited at RT. The Ag bottom layers were deposited at 200 °C, which was done to increase the Ag grain size in order to decrease the amount of (grain boundary) interdiffusion and IMC formation (cf. Section 2.3.1), thereby preserving the as-deposited state for a longer period of time. Thicknesses of the sublayers varied from 50 nm to 500 nm. The subsequent depositions of the sublayers were carried out without breaking the vacuum; Auger electron spectroscopy, done with a Jeol Jamp 7830 F, revealed that no oxide layer was present between the bottom and the top sublayers.

Thicknesses and deposition rates of the films were monitored with a quartz crystal balance (Lesker), which was separately calibrated for Ag and Sn. A deposition rate of 8 Å s^{-1} was generally used for all Ag layers; in two cases deposition rates of 4 Å s^{-1} and 16 Å s^{-1} were used. A deposition rate of 12 Å s^{-1} was used for Sn, if Sn was the bottom layer. A higher deposition rate of 23 Å s^{-1} was used for Sn, if Sn was the top layer, in order to decrease the roughness of the Sn top layers. Thickness and roughness of the single- and bilayers were measured with a Dektak 8 profilometer (Veeco).

For each material and deposition rate, the substrate-surface temperature was measured with a type-k thermocouple during deposition of single layers. The maximum surface temperatures reached during deposition of the Ag top sublayers at 4 Å s^{-1}, 8 Å s^{-1} and 16 Å s^{-1} were 33 °C, 38 °C and 39 °C, respectively. For Sn deposition rates of 12 Å s^{-1} and 23 Å s^{-1} the maximum surface temperatures were 45 °C and 49 °C, respectively. The indicated temperature for the deposition of the Ag bottom sublayer (200 °C) corresponds to the average temperature as measured with the thermocouple. An overview of all bilayers prepared for this work is given in Table 2.1.

The present study is focused on bilayers in the as-deposited state. However, interdiffusion and phase formation proceed rapidly in the Ag–Sn samples, even at RT (Cooling the samples is no option in view of the β-Sn to α-Sn transition at 13 °C). Therefore, first measurements after bilayer preparation, unavoidably taken some time after bilayer

Table 2.1: Overview of the stacking sequence, thicknesses, depositions rates and deposition temperatures of the Ag and Sn sublayers in the investigated bilayers.

stacking sequence	**thickness [nm]**	**dep. rate [Å/s]**	**dep. temp. [°C]**
Ag on top of Sn	Ag: 500 Sn: 500	Ag: 4 Sn: 12	Ag: room temp. Sn: room temp.
Ag on top of Sn	Ag: 500 Sn: 500	Ag: 8 Sn: 12	Ag: room temp. Sn: room temp.
Ag on top of Sn	Ag: 500 Sn: 500	Ag: 16 Sn: 12	Ag: room temp. Sn: room temp.
Ag on top of Sn	Ag: 75 Sn: 500	Ag: 8 Sn: 12	Ag: room temp. Sn: room temp.
Ag on top of Sn	Ag: 500 Sn: 100	Ag: 8 Sn: 12	Ag: room temp. Sn: room temp.
Sn on top of Ag	Sn: 500 Ag: 500	Sn: 23 Ag: 8	Sn: room temp. Ag: 200
Sn on top of Ag	Sn: 50 Ag: 500	Sn: 23 Ag: 8	Sn: room temp. Ag: 200

deposition, represent a starting stage of aging already; this especially holds for the TEM measurements.

2.2.2 X-ray Diffractometry (XRD)

Phase analysis of the thin films was performed on the basis of $\theta - 2\theta$ scans (2θ = diffraction angle) recorded with a Bruker TXS D8 Discover diffractometer using Cu-K_α radiation from a rotating anode X-ray tube. The tube was operated at 50 kV and 24 mA. A Xenocs Fox 2D collimating mirror was placed in the incident beam path in order to obtain a parallel X-ray beam. The radiation emerged from a 100 × 100 μm^2 spot under a take-off angle of 6°. A VÅNTEC-500 2D detector was used with a recording time of typically 120 s per frame. It covers a 2θ range from 29.8° to 47.0°. The illuminated area on the sample was restricted by cylindrical collimators with diameters of 0.5 mm or 1.5 mm. The intensities recorded by the 2D detector were converted to conventional XRD diffractograms by integrating over a χ range from 73.8° to 106.6°, where χ is the Eulerian tilt angle).

To investigate the textures of the bilayers, Ag {111} and Sn {100} pole figures were recorded with a Philips (PANalytical) MRD Pro diffractometer utilizing {111} Ag and {200} Sn reflections, respectively. The diffractometer was operated in a parallel-beam geometry with a polycapillary X-ray collimator in the incident beam. The spot size of the incident beam was approximately 4 × 4 mm^2. Co-K_α radiation from a conventional X-ray

tube, operating at 40 kV and 40 mA, was used. K_β radiation was removed by a graphite monochromator in the diffracted beam. Intensities were recorded using a proportional counter.

2.2.3 Electron Microscopy (SEM and TEM)

In order to investigate the microstructure of the thin films, cross sections of the bilayers were prepared and investigated with a FEI Nova Nanolab 600 Dual-Beam (Focussed Ion Beam (FIB)) instrument. Before cutting the cross section, a Pt capping layer was deposited in order to obtain a sharp interface to the surface in the cross section, as well as to protect the individual layers. Images were recorded with the electron beam mode of operation (SEM) as well as with the ion beam mode of operation (FIB) using a secondary electron (SE) detector.

Transmission electron microscopy (TEM) specimens were also prepared with the Dual-Beam instrument using the in-situ lift-out technique [104]. Typical thickness of the TEM specimens was about 100 nm. For the TEM investigations a Philips CM200 instrument equipped with a double tilt stage and a LaB_6 cathode operating at an acceleration voltage of 200 kV was used. A Gatan CCD camera, attached to the microscope, was used to capture bright field (BF) and dark field (DF) images and selected area diffraction patterns (SADPs).

2.2.4 Scanning Transmission Electron Microscopy (STEM)

EDX line profiles were recorded from TEM specimens (cf. Section 2.2.3) employing a Zeiss SESAM microscope using a field emission gun operating at 200 kV. EDX measurements were performed at 30 equidistant points along a line across the cross-section of the specimen.

2.3 Results

2.3.1 Phase constitution and preferred orientation

Ag on top

In the case of as-deposited Ag / Sn bilayers, i.e. with Ag on top, the XRD patterns reveal the presence of Ag, Sn and Ag_4Sn phases. Additionally, a significant amount of diffuse intensity is present between the Ag_4Sn (011) and the Ag (200) peak positions (see Fig. 2.1). The XRD pattern shown in Fig. 2.1 pertains to a 500 nm Ag / 500 nm Sn bilayer and was recorded about 30 min after the start of the Ag deposition (cf. end of Section

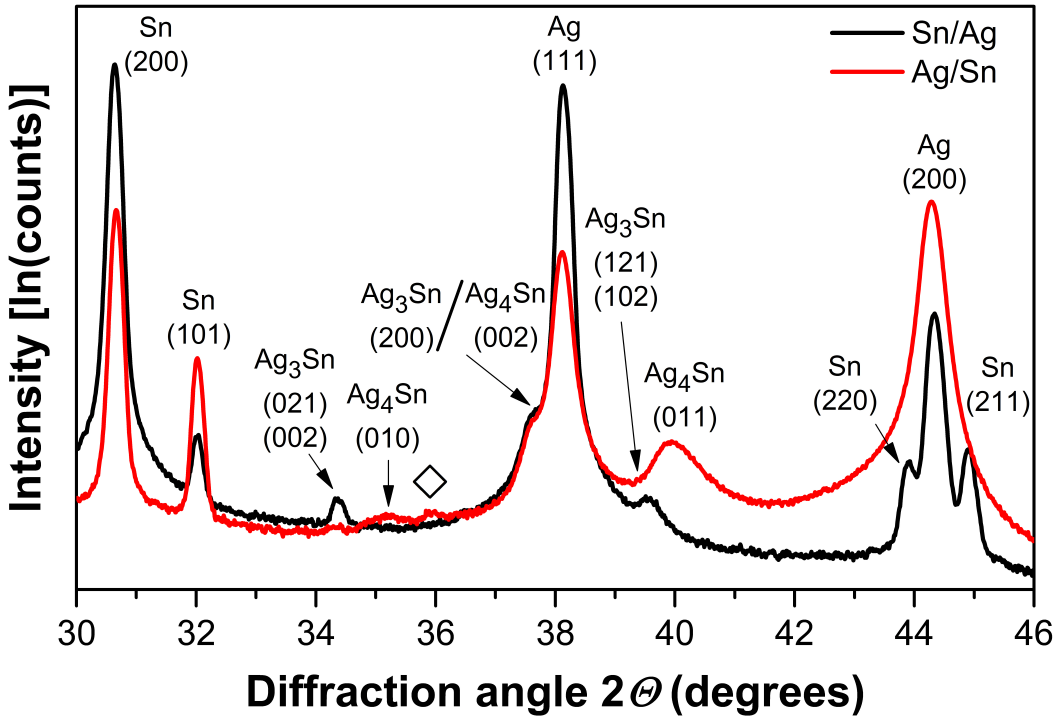

Fig. 2.1: XRD patterns obtained from the as-deposited 500nm Ag / 500 nm Sn and 500 nm Sn / 500 nm Ag bilayers. The symbol ◇ indicates intensity originating from Ag_2O ((002) reflection), which develops at the Ag surface once the bilayer is removed from the deposition chamber.

2.2.1). Neither increase of the diffuse intensity nor increase of the intensity of the Ag_4Sn IMC peaks is observed upon continued aging at RT.

For a bilayer with a thin top Ag sublayer (75 nm Ag / 500 nm Sn), the first diffraction pattern could be obtained only about 15 min after the onset of the Ag deposition, due to the smaller thickness of the Ag layer. Also in the latter case no further increase of the diffuse intensity and the intensity of the Ag_4Sn peaks occurred upon continued aging at RT. The largest intensity of the Ag_4Sn IMC peaks and of the diffuse intensity was observed for 500 nm Ag / 100 nm Sn bilayers. In the case of this thin (100 nm) Sn sublayer, no Sn peaks occur in the XRD pattern of the as-deposited state (see Fig. 2.2); only Ag and Ag_4Sn peaks as well as the diffuse intensity can be detected.

The Ag_4Sn peaks for all bilayers are very broad, which can be due to a variation of composition and/or a heavily faulted microstructure. It was also found that the Ag_4Sn peak intensities and the diffuse intensity decrease with increasing Ag deposition rate, from 4 Å s^{-1} to 16 Å s^{-1}, for Ag / Sn bilayers of identical sublayer thicknesses.

An EDX line profile recorded from an Ag / Sn bilayer with only a 100 nm thick Sn sublayer is given in Fig. 2.3. Two depth ranges can be distinguished; (i) a near surface region (with a thickness of about 200 nm) of constant concentration of about 97 ± 1 at.%

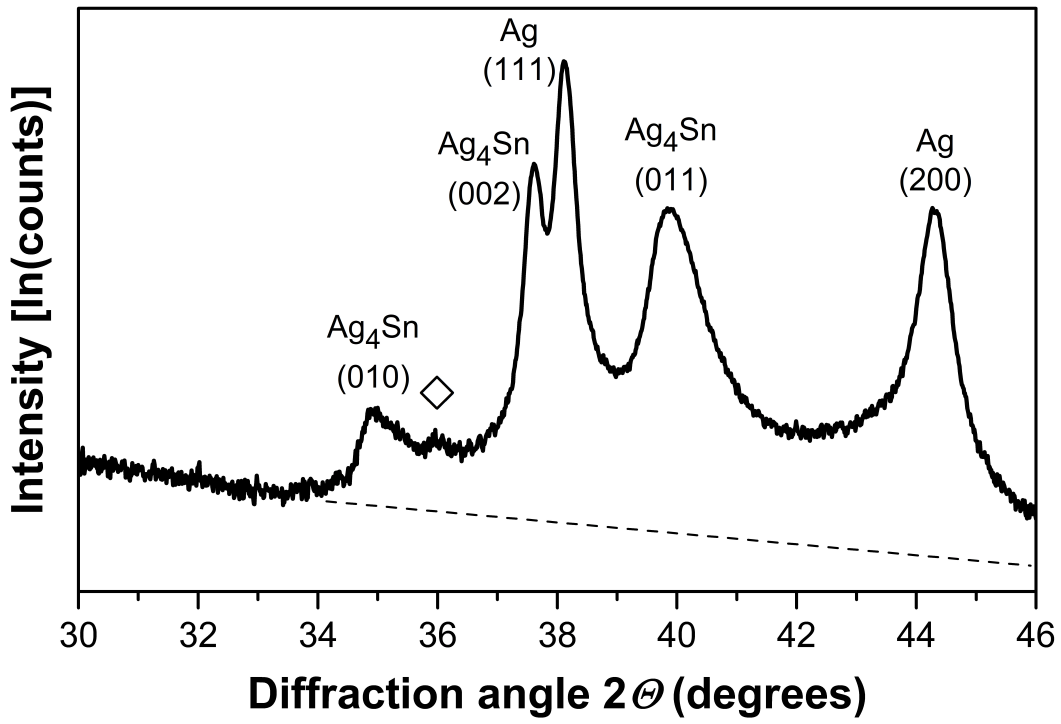

Fig. 2.2: XRD pattern from the as-deposited 500 nm Ag / 100 nm Sn bilayer, showing a large amount of diffuse intensity between the Ag_4Sn (011) and Ag (200) peaks. The dashed line indicates the background, as determined from an 500 nm Sn / 500 nm Ag bilayer, where no diffuse intensity is present (see text). The symbol ◇ indicates intensity originating from Ag_2O ((002) reflection), which develops at the Ag surface once the bilayer is removed from the deposition chamber.

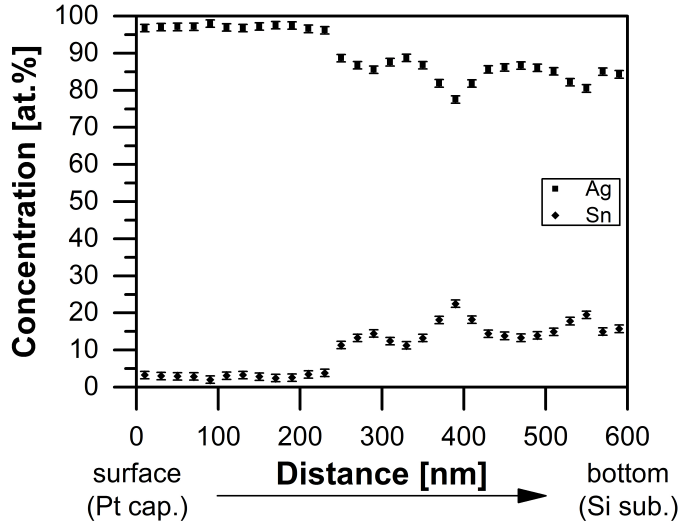

Fig. 2.3: EDX line scan recorded from a cross-section of a 500 nm Ag / 100 nm Sn Ag bilayer. Error bars were obtained from repeated measurements of the Ag layer.

Ag and (ii) a region of average Sn concentration of 15±1 at.% at larger depths. The latter region is identified as the Ag_4Sn layer, since its Sn concentration is in agreement with the homogeneity range of the Ag_4Sn phase at RT [54]. Concentration variations occur within the Ag_4Sn layer, which can cause (contribute to) the distinct line broadening observed for the Ag_4Sn peaks in the XRD patterns (see above and Fig. 2.1).

The Ag layers growing on top of the Sn layers are largely {100} fibre-textured (identified by the strong intensity at $\Psi \approx 55°$ in the {111} pole figures; see Figs. 2.4a and 2.4b) in contrast with the {111} fibre texture observed for a single Ag layer. The observed {111} fibre-texture of the evaporated Ag *single* layers is commonly observed for thin films of fcc metals [87, 90, 95, 96]. In the physical vapor deposition processes nuclei with top surfaces parallel to the most densely packed lattice plane are preferred, since these surfaces posses the lowest surface energy [97, 96]. In Section 2.3.2 it will be shown that some Ag grains on top of the Sn grains directly grow in extension of the underlying Sn grains, indicating that the Ag grains nucleate coherently or at least epitaxially on preexisting grains of the Sn sublayer. This could explain the occurrence of a {100} fibre texture of the evaporated Ag top layers on the crystalline Sn sublayer, instead of a {111} fibre texture as for the Ag layer grown directly on the amorphous SiO_2 layer covering the substrate. The Sn sublayers, both as surface layer and as sublayer under an Ag top layer, grown directly on the amorphous SiO_2-covered substrate, show a sharp {100} fibre texture (Figs. 2.4c and 2.4d). For Sn, the (100) lattice plane is a close-packed plane, which therefore is expected to have the lowest surface energy (cf. above discussion).

Sn on top

In the case of the as-deposited Sn / Ag bilayers, i.e. with Sn on top, the XRD patterns reveal the presence of Sn, Ag and Ag_3Sn phases (see Fig. 2.1). The Ag_3Sn and Ag_4Sn IMCs are structurally closely related. The Ag_4Sn phase has a disordered Mg-type hcp structure [51], and Ag_3Sn has an ordered orthorhombically-distorted hcp structure [108]. The Ag_3Sn IMC can therefore be identified by the presence of peak splitting of the fundamental hcp reflections. As indicated in Fig. 2.1, the (010) and (011) peaks of Ag_4Sn, as observed for "Ag on top" (Section 2.3.1), are "replaced" by, respectively, the (021) and (002) peaks and the (121) and (102) peaks of the Ag_3Sn phase, as observed for "Sn on top". The splitting could be clearly identified in this project using high-resolution XRD on RT aged bilayers where the amount of Ag_3Sn has increased, as compared to the as-deposited state. The shape of the Ag_3Sn peaks does not exclude the presence of Ag_4Sn and indeed TEM analysis shows that a small amount of Ag_4Sn is present (see Section 2.3.2). Unlike in the case "Ag on top" with a thin (100 nm) Sn sublayer, where after

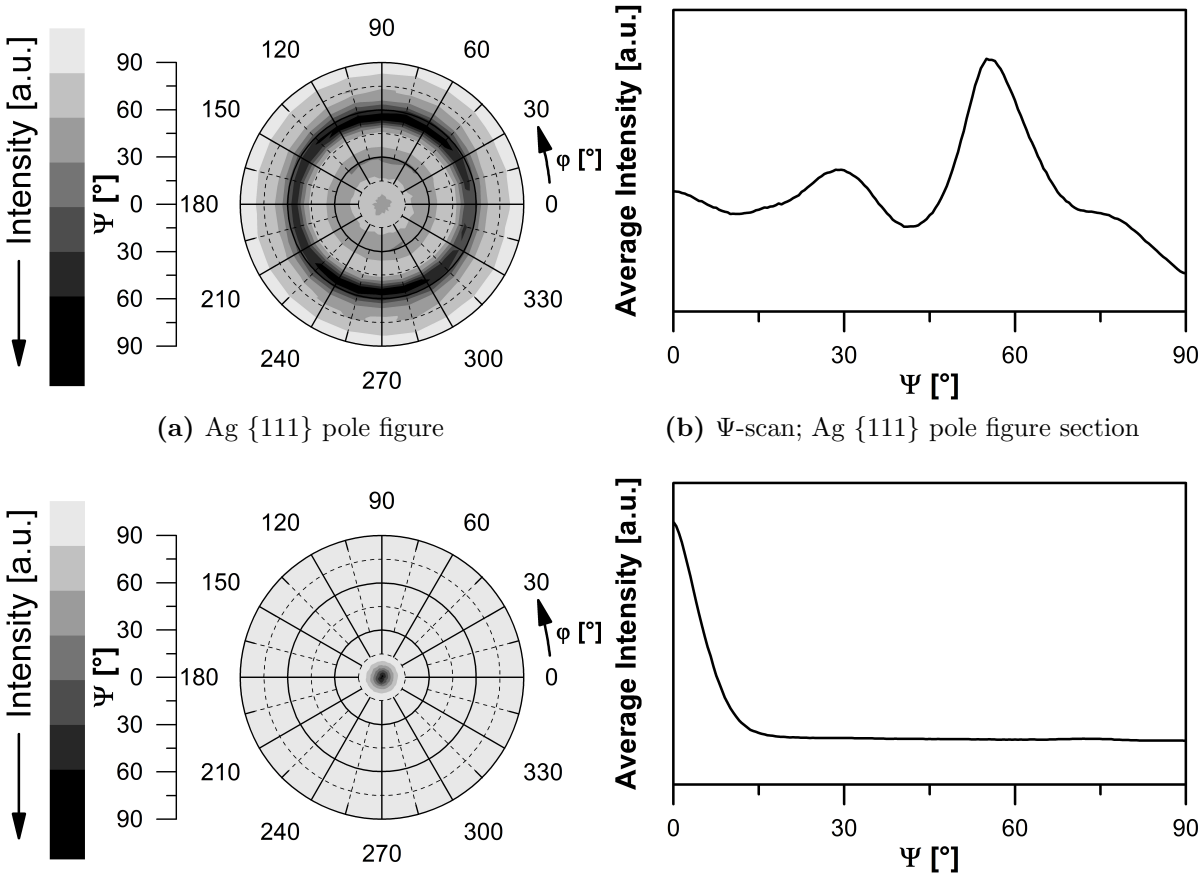

(a) Ag {111} pole figure

(b) Ψ-scan; Ag {111} pole figure section

(c) Sn {100} pole figure

(d) Ψ-scan; Sn {100} pole figure section

Fig. 2.4: Texture analysis of 500 nm Ag / 500 nm Sn bilayers. Ag {111} and Sn {100} pole figures are shown in (a) and (c), respectively. Ψ-profiles averaged over all ϕ-angles are shown in (b) and (d) for the respective pole figures. Both layers are {100} fibre-textured. The Ag layer also shows a weak {111} texture component.

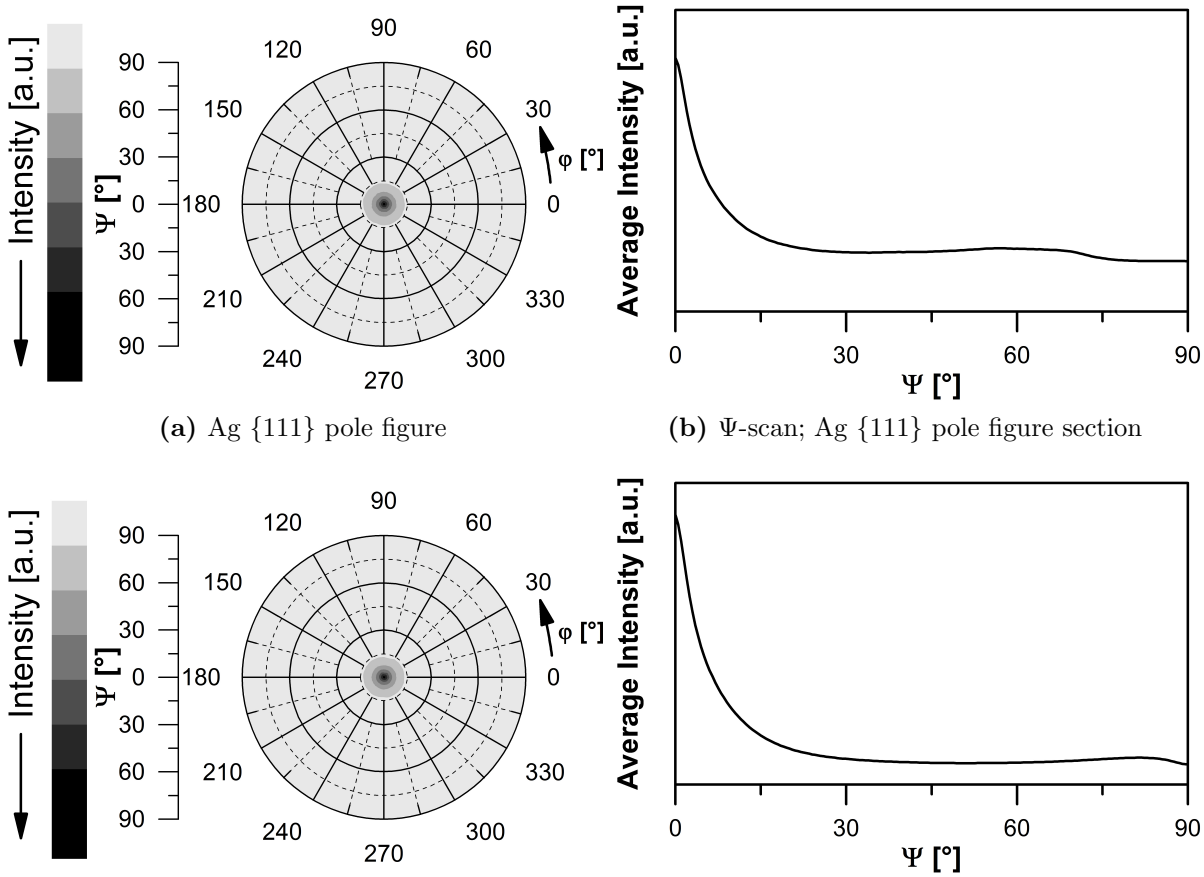

(a) Ag {111} pole figure

(b) Ψ-scan; Ag {111} pole figure section

(c) Sn {100} pole figure

(d) Ψ-scan; Sn {100} pole figure section

Fig. 2.5: Texture analysis of 500 nm Sn / 500 nm Ag bilayers. Ag {111} and Sn {100} pole figures are shown in (a) and (c), respectively. Ψ-profiles averaged over all ϕ-angles are shown in (b) and (d) for the respective pole figures. The Ag layer is {111} fibre-textured and the Sn layer is {100} fibre-textured.

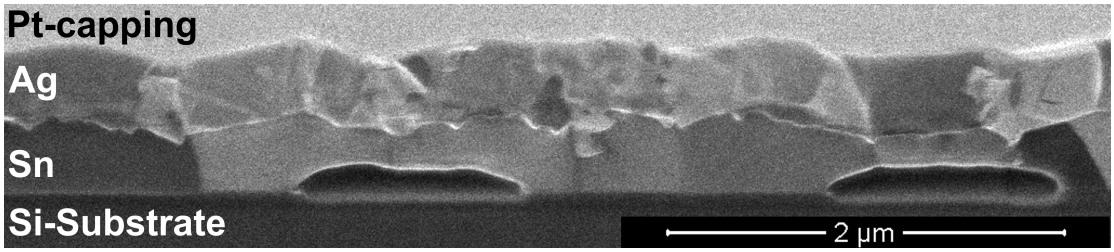

Fig. 2.6: FIB image of an ion-beam prepared cross-section showing a 500 nm Ag / 500 nm Sn bilayer in the as-deposited state. Large macroscopic voids can be seen in the Sn layer.

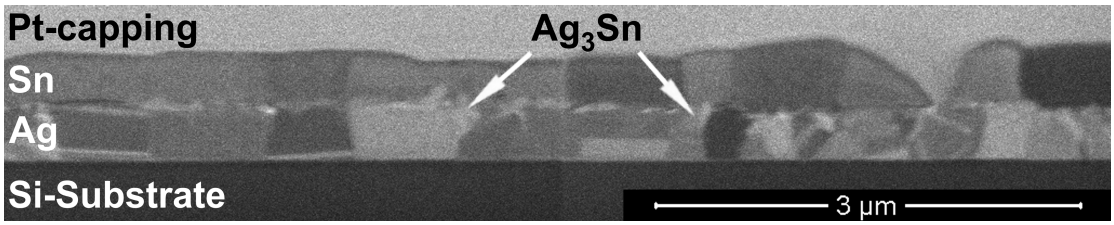

Fig. 2.7: FIB image of an ion-beam prepared cross-section showing a 500 nm Sn / 500 nm Ag bilayer in the as-deposited state. The arrows indicate two sites, as examples, where Ag_3Sn can be discerned.

bilayer deposition no Sn peaks occur in the diffraction pattern (cf. Fig 2.2), even for a 50 nm Sn / 500 nm Ag bilayer, i.e. in the case of "Sn on top" with a very thin Sn sublayer, the XRD pattern exhibited the presence of Sn peaks.

The Ag layers of the Sn / Ag bilayers have a strong {111} fibre texture (Figs 2.5a and 2.5b), and the Sn layers have a strong {100} fibre texture (Figs. 2.5c and 2.5d). Both these textures are similar to those observed for the single layers and reflect the tendency to minimize the surface energy (cf. discussion at the end of Section 2.3.1).

2.3.2 Microstructure of the bilayers

The selected deposition parameters for the thermal evaporation process (see Section 2.2.1) lead to the formation of continuous single and bilayers with smooth surfaces, for thicknesses approaching 500 nm. Typical surface roughnesses for bilayers with Ag and Sn on top are $R_a = 20 \pm 1$ nm and $R_a = 26 \pm 1$ nm, respectively. In cross-sections of both types of bilayers, the interface between the two separate layers in the as-deposited state is sharp, as revealed by Dual-Beam micrographs (see Figs. 2.6, 2.7 and 2.8).

The micrographs reveal a dense, columnar grain morphology of the evaporated bilayers. For the growth conditions pertaining to the films shown (Figs. 2.6 and 2.7), these morphologies are compatible with the zone model for evaporated metal films [88], with the exception of the Ag top layers (see below).

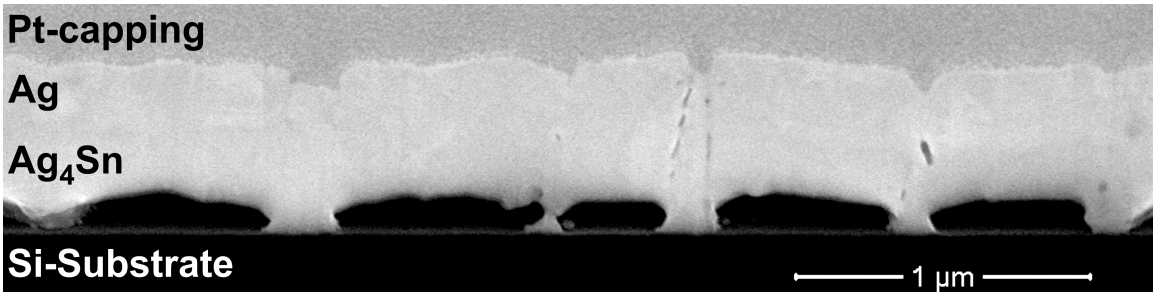

Fig. 2.8: SEM micrograph from the ion-beam prepared cross-section of a 500 nm Ag / 100 nm Sn bilayer in the as-deposited state. Island-shaped voids can be seen, which represent the locations where the Sn "layer" was present before its dissolution into the Ag layer. The Ag_4Sn layer is identified by the EDX linescan in combination with the XRD patterns.

Ag on top

Large grains can be seen in the Sn layers (Fig. 2.6), deposited at $T/T_m = 0.63$, corresponding to Zone 3 of Ref. [88], where extensive grain growth during deposition dominates, leading to large grain sizes. For the Ag top layers the grain morphology is influenced by the Sn layer underneath it (see below) and therefore cannot be directly related to the zone model of Ref [88].

The main difference of the microstructures of the Ag / Sn bilayers and the Sn / Ag bilayers is the presence of macroscopic voids in the Sn layer adjacent to the substrate of the Ag / Sn bilayers (see Fig. 2.6). This phenomenon becomes more pronounced in case of thin (100 nm) Sn sublayers, as holds for the 500 nm Ag / 100 nm Sn bilayer (see Fig. 2.8). In the latter case the voids are faceted and present inside the Ag_4Sn layer.

The XRD patterns of Ag / Sn bilayers clearly show the presence of Ag_4Sn diffraction peaks. The EDX composition-depth profiles measured on cross sections of the 500 nm Ag / 100 nm Sn bilayer are compatible with the presence of an Ag_4Sn layer below the Ag top layer (see Section 2.3.1 and Fig. 2.3). The separate Ag_4Sn layer cannot be identified in the Dual-Beam micrographs shown in Figs. 2.6 and 2.8, owing to too weak (mass) contrast.

TEM BF images, along with corresponding SAD patterns, obtained from the Ag top layer, reveal the presence of heavily faulted Ag regions, i.e. planar faults near to the interface of Ag and Ag_4Sn, in association with the presence of streaks of diffuse intensity in the SAD pattern (see Fig. 2.9). The streaks are oriented perpendicular to a (111) plane of the Ag lattice indicating that the fault planes are {111} planes. (Indeed, Ag is a metal of relatively low stacking fault energy [109, 110, 111]). Since the (111) planes correspond to twinning planes in Ag [112], the planar faults can correspond to twinned Ag regions, with the Ag (111) twin plane approximately parallel to the electron beam, causing the streaks in the SAD pattern. TEM BF images also reveal heavily faulted

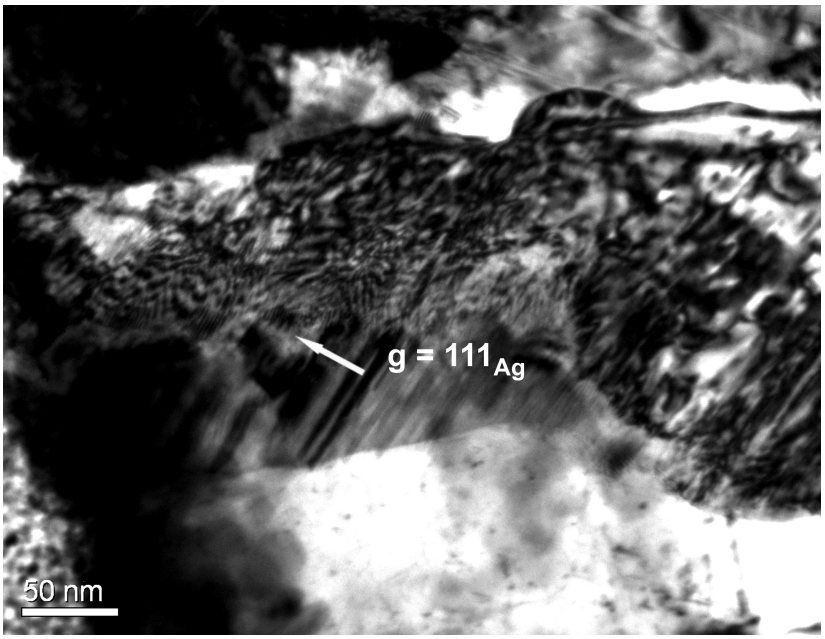

(a)

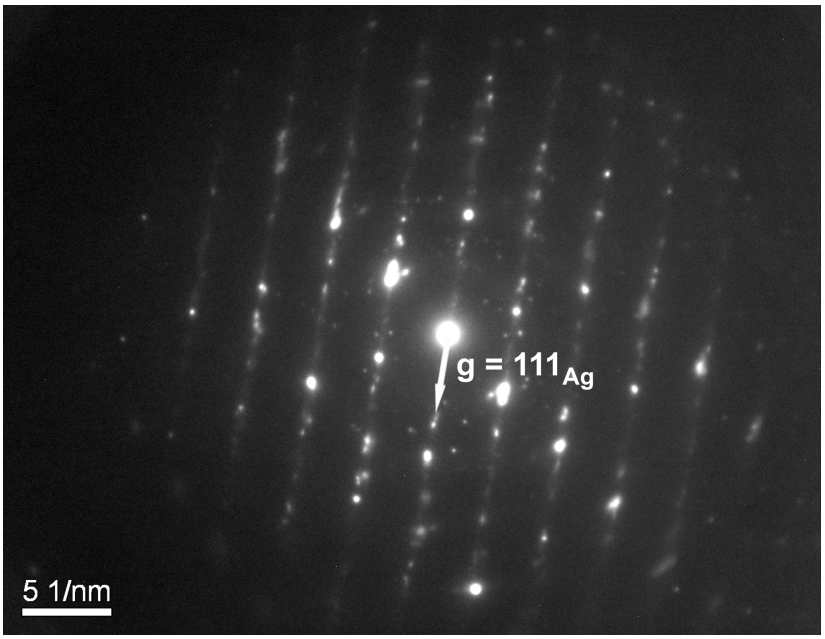

(b)

Fig. 2.9: TEM images obtained from the cross-section of a 500 nm Ag / 100 nm Sn bilayer. (a) The BF image shows a heavily faulted microstructure in the Ag layer. (b) The SAD pattern obtained from the region with planar faults shows a large amount of diffuse intensity streaks. The diffraction vector of a weak spot, compatible with a Ag (111) reflection, with direction along the diffuse streaks, has been indicated. This diffraction vector is perpendicular to the planar faults in the BF image, the planar faults may therefore be interpreted as twinning planes.

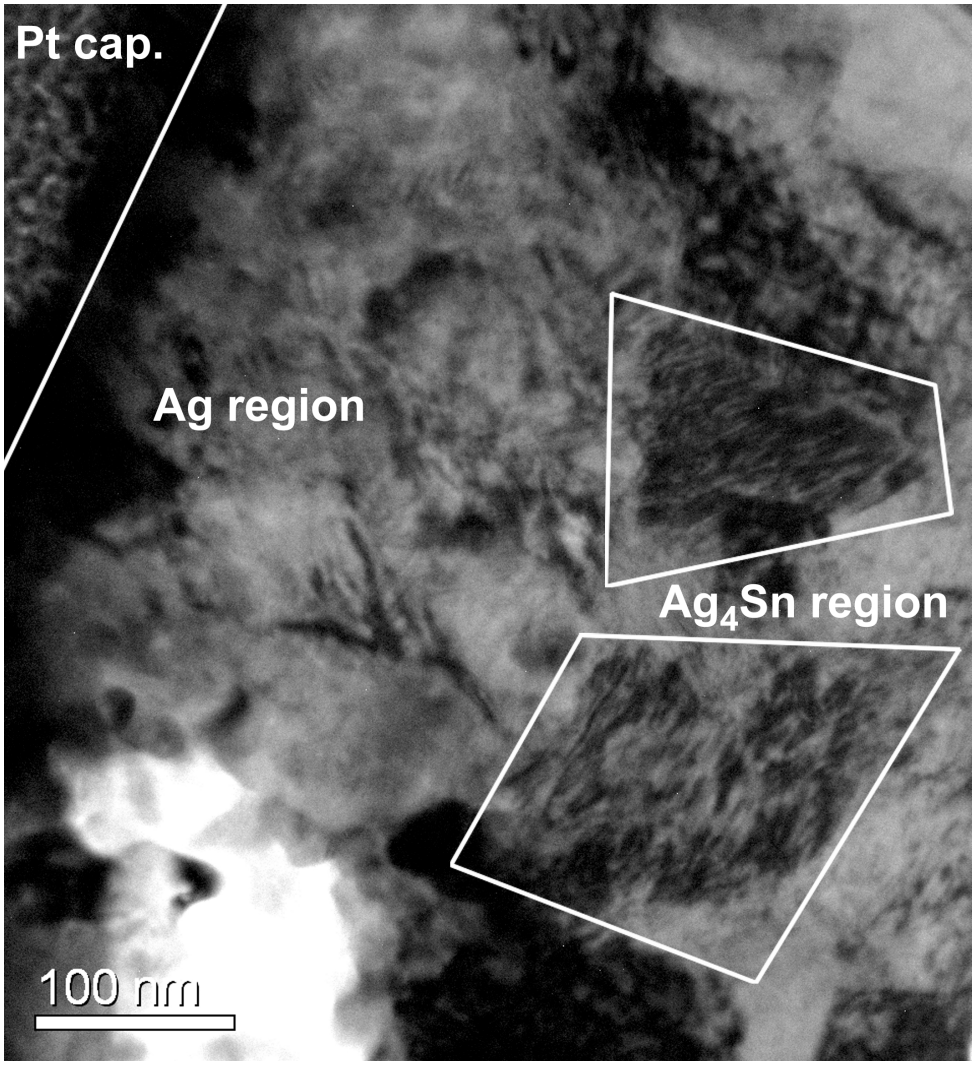

Fig. 2.10: TEM BF image obtained from the cross-section of a 500 nm Ag / 100 nm Sn bilayer, showing heavily faulted regions (within the white boxes) in the depth range where Ag_4Sn is present (cf. Figs. 2.3 and 2.8).

Ag_4Sn grains. One such BF image, taken near a void in the Ag_4Sn layer, is shown in Fig. 2.10. Heavily faulted regions can be seen in the depth range where Ag_4Sn is present (cf. Figs. 2.3 and 2.8).

Sn on top

Again large grains occur in the Sn sublayers (Fig. 2.7), deposited at $T/T_m = 0.64$, corresponding with Zone 3 of Ref. [88] (cf. Section 2.3.2).

The Ag bottom layer shown in Fig. 2.7 was deposited at $T/T_m = 0.38$ (200 °C). Columnar grains along with larger equiaxed grains can be seen in the Dual-Beam micrograph (Fig. 2.7), which corresponds with Zone 2 in Ref. [88]. Such a bimodular nature

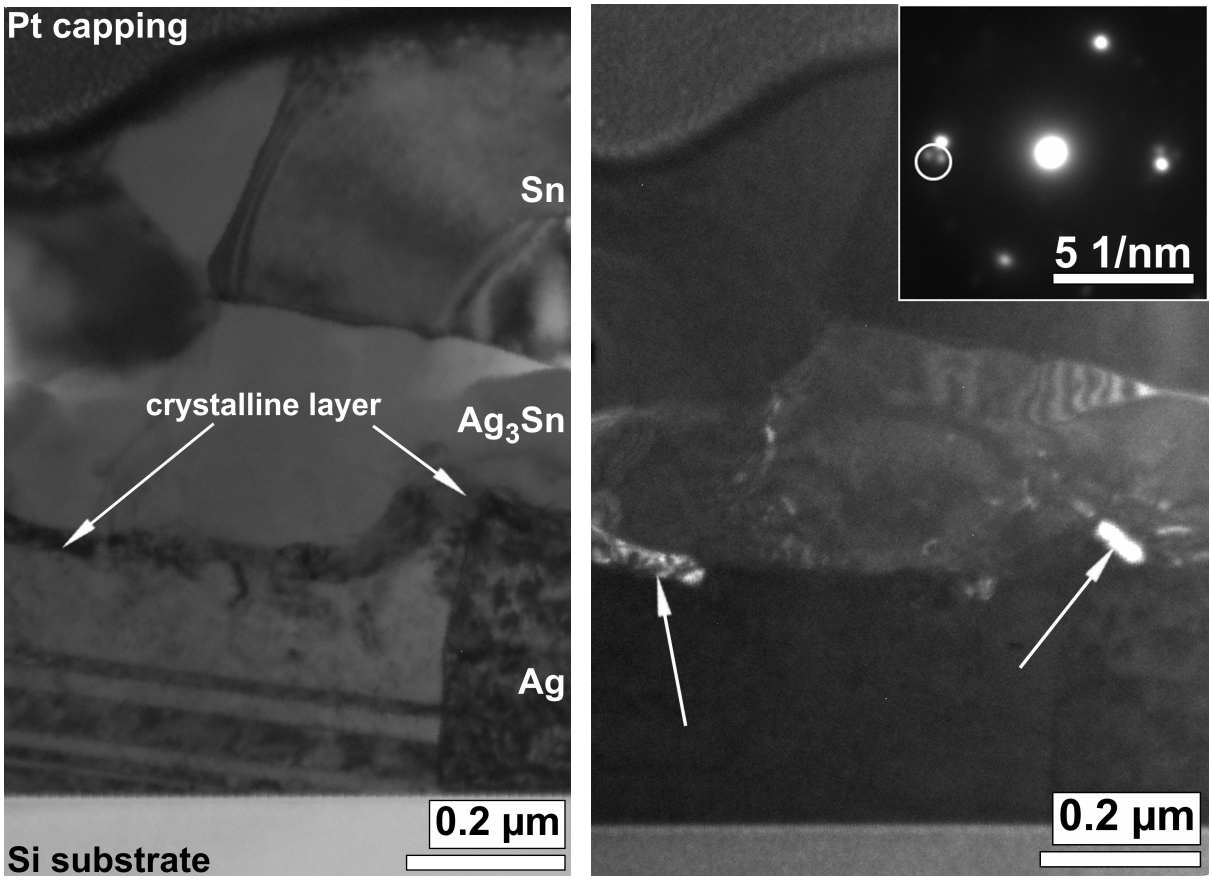

(a) (b)

Fig. 2.11: TEM cross-section showing a 500 nm Sn / 500 nm Ag bilayer. (a) The BF image reveals an extra layer between the Ag_3Sn and Ag layers. (b) Parts of this layer appears as a bright contrast in the DF image (see arrows in (b)), taken with reflections compatible with (010) and (011) of Ag_4Sn (see the SADP (insert)).

of the grain-size distribution can be the result of surface-energy anisotropy as well as strain-energy anisotropy for crystallographically differently oriented grains, in particular for the morphologies of thin films where the surface to bulk ratio of the grains is high [9, 95, 113].

The Ag_3Sn phase that is present in the as-deposited state of the Sn / Ag bilayers (cf. Section 2.3.1) occurs as a very thin layer between the Sn and the Ag sublayers (see Fig. 2.7). For aged specimens (see comments at the end of Section 2.2.1), a thin layer had emerged between the Ag_3Sn layer and the Ag layer, as can be seen in the TEM cross-section of Fig. 2.11. Parts of it appear in bright contrast in the DF image obtained with the diffraction spots compatible with (010) and (011) Ag_4Sn diffraction spots, as indicated in the inset of Fig. 2.11b. Combined with the XRD results (see Section 2.3.1 and Fig. 2.1) it can be deduced that this extra layer is the Ag_4Sn phase, the presence of which is suggested by the Ag_3Sn peak shape in the XRD patterns (see discussion in Section 2.3.1).

2.4 Discussion

The striking difference between the bilayers Ag / Sn ("Ag on top") and Sn / Ag ("Sn on top") is the different IMC present in the as-deposited state: predominantly Ag_4Sn with "Ag on top" and Ag_3Sn with "Sn on top" (see Section 2.3.1). Additionally, only for the Ag / Sn bilayers the Ag sublayer has taken up a considerable amount of Sn in the as-deposited state, leading to the voids in the remaining Sn sublayer and even the complete disappearance of Sn for very thin Sn sublayers, whereas this is not the case for the Sn / Ag bilayers. The next 2 subsections discuss the Ag and Sn intermixing during sublayer growth, and the formation of the IMCs and their subsequent growth.

2.4.1 Intermixing during sublayer growth

In view of the high mobilities of Ag and Sn at RT (see Section 2.1) it is expected that Ag and Sn start to interdiffuse already during layer deposition for both stacking sequences, thus forming a diffusion zone, most pronouncedly within the Ag sublayer (Sn has no distinct solubility for Ag at RT).

The voids in the bottom Sn sublayer in Ag / Sn bilayers are interpreted as the consequence of a net vacancy flux into the Sn layer: a large amount of Sn diffuses substitutionally into the growing Ag layer causing a vacancy flux into the Sn sublayer. Sn has a negligible solubility for Ag at RT, and above all Ag diffuses interstitially in Sn [105, 15], so that no vacancy flux out of the Sn layer can be caused by Ag diffusion into the Sn sublayer. Hence an excess vacancy concentration develops in the Sn layer from which

vacancies can condensate as voids, preferentially at the Sn sublayer / substrate interface, as the nucleation barrier for voids is reduced at an interface: so-called Kirkendall porosity (see also Refs. [114, 17, 18]. If the Sn sublayers are very thin, the XRD patterns show that even no Sn layer is present in the as-deposited state. The faceted voids adjacent to the substrate in the corresponding cross-sections (Fig. 2.8) likely represent an "image" of the very thin Sn sublayer before deposition of the Ag layer: island coalescence had not yet occurred upon Sn film growth leading to the presence of distinctive faceted Sn islands, which "dissolved" entirely into the growing Ag layer upon subsequent Ag deposition.

Two driving forces can be indicated for Sn uptake in Ag: a negative Gibbs energy of mixing, and in case of "Ag on top", the difference in surface energy of Sn and Ag: the surface energy of Sn is about half that of Ag [115, 116] (0.675 J/m^2 for Sn and 1.250 J/m^2 for Ag) and thus segregation of Sn at the surface of the Ag / Sn bilayer lowers the Gibbs energy of the system. A similar driving force for intermixing, i.e. due to a difference in surface energy, is also operating in Cu / Si and Mo / Si bilayers [117, 118, 119, 120].

If Sn is deposited onto Ag the secondly above-mentioned driving force, due to a difference in surface energy, is absent. Indeed, no pronounced intermixing of Sn and Ag occurs during deposition of Sn on Ag (cf. Section 2.3.1).

The high Sn concentration in the Ag top layer due to the larger intermixing in the Ag / Sn bilayers (compared to the Sn / Ag bilayers) lowers (even further) the already low stacking fault energy of the Ag layer [109, 110, 111] promoting the formation of heavily faulted Ag grains, as observed in the TEM micrographs (Fig. 2.9a), particularly close to the interface of the Ag layer and the Ag_4Sn layer. As a consequence, pronounced streaks of diffuse intensity occur in reciprocal space perpendicular to {111} Ag lattice planes (cf. Fig. 2.9b). The diffuse intensity observed between the Ag_4Sn (011) and the Ag (200) peaks in the XRD patterns (cf. Figs. 2.1 and 2.2) can originate from these streaks but may also contain a contribution from compositional variation in Ag_4Sn (see Fig. 2.3). In general residual stresses could also induce faulting. However, XRD stress measurements on the Ag top and bottom layers [121] have shown that residual stresses in the Ag top layer are lower (35 ± 4 MPa) than in the Ag bottom layer (81 ± 3 MPa). Hence, the occurrence of faulting especially in the Ag *top* sublayer is ascribed mainly to the lowering of the Ag stacking fault energy. The compositional variation in the Ag_4Sn grains (Fig. 2.3) and its also heavily faulted microstructure (cf. Fig. 2.10) induce the broadening of the Ag_4Sn peaks observed in the XRD pattern. No such severe faulting and diffuse intensity is observed for the Sn / Ag bilayers. Indeed, during layer deposition much less Sn is taken up by the Ag sublayer in case of "Sn on top" (see above discussion on intermixing driving forces). Therefore, the stacking fault energy of the Ag sublayers in case of "Sn on top" is distinctly less lowered.

The amount of Ag_4Sn in the as-deposited state, i.e. for the bilayers with "Ag on top", decreases with increasing Ag deposition rate (see Section 2.3.1). This can be interpreted as follows: for a larger Ag deposition rate the Ag layer is thicker *at any given time*. Sn atoms diffusing into the growing Ag layer can only reach the sink at the surface of the growing Ag layer if it is sufficiently thin. Consequently, the overall concentration gradient acting very close to the interface of both sublayers is smaller for larger Ag deposition rates and thus less Sn is taken up in the Ag sublayer for larger Ag deposition rates. On a similar basis it can be explained why the size of the intermixed zone in Mo / Si bilayers decreases with increasing Mo deposition rate [120].

2.4.2 Formation of Ag_4Sn vs. Ag_3Sn; Thermodynamics and Kinetics

No literature values for the Gibbs energies of formation of Ag_3Sn and Ag_4Sn are available. They are estimated here as follows: the enthalpies of formation from the elements at 298 K are -16.8 ± 4 kJ mol^{-1} for Ag_3Sn and -18.7 ± 7 kJ mol^{-1} for Ag_4Sn, respectively [122]. Similar values have been obtained in Ref. [123], in this case with indicated uncertainty ranges which do not overlap. In case of the ordered Ag_3Sn IMC the contribution of the configurational entropy is nearly zero in view of its ordered nature [124] and the enthalpy of formation is therefore taken as an estimate for the Gibbs energy of formation. In case of the disordered Ag_4Sn IMC, the configurational entropy can be estimated by the entropy of ideal mixing [124]. Thus adopting an ideal solid solution of 85 at.% Ag and 15 at.% Sn (as estimate for the composition of Ag_4Sn, see results of the EDX measurements shown in Fig. 2.3), the contribution of the entropy of mixing at RT to the Gibbs energy of formation is estimated as -5.2 kJ mol^{-1}. The approximate Gibbs energies of formation of the Ag_3Sn and Ag_4Sn IMCs are therefore -16.8 ± 4 kJ mol^{-1} and -25.6 ± 7 kJ mol^{-1}, respectively.

In case of the Ag / Sn bilayers, Sn from the bottom layer diffuses into the growing Ag top layer. The IMC therefore develops inside the Ag layer (possibly with nucleation at the interface of the Ag and Sn layers), once the Sn concentration in the intermixed zone of the Ag top layer exceeds the solubility limit for Sn in Ag. In the intermixed zone a small amount of Sn is dissolved in an Ag matrix. Then, in order to determine if the largest amount of Gibbs energy is released by precipitation of either Ag_3Sn or Ag_4Sn, the Gibbs energies of the reactions:

$$3[Ag] + [Sn] \rightarrow Ag_3Sn \tag{2.1}$$

and

$$4[Ag] + [Sn] \rightarrow Ag_4Sn \tag{2.2}$$

have to be considered in terms of the amount of Gibbs energy released *per mole reacting Sn*, starting with the solid solution (i.e. [Ag] and [Sn]). Then, the partial Gibbs energies of Ag and Sn in the solid solution (i.e. of [Ag] and [Sn]) have to be known as well. Assuming an ideal solid solution of Ag and Sn, the partial Gibbs energies can be calculated from the standard Gibbs energies of pure Ag and pure Sn and the mole fractions of Ag and Sn in the solid solution. For a pure element the standard Gibbs energy is given by the contribution of the standard entropy of the pure element. Using standard entropies of 42.7 J mol^{-1} for Ag and 51.5 J mol^{-1} for Sn [7] and assuming an ideal solid solution of 10 at.% Sn in Ag (corresponding to the solubility limit of Sn in Ag [52]), the Gibbs energies of formation per mole Sn atoms from the solid solution are -10.3 ± 4 kJ mol^{-1} and -18.5 ± 7 kJ mol^{-1} for Ag_3Sn and Ag_4Sn, respectively. The IMC with the larger energy release will most likely develop first, i.e. Ag_4Sn in the case of an Ag top layer, as observed.

For the "Sn on top" bilayers it cannot be concluded from the present results if the IMCs nucleate inside the Ag or the Sn layer. If the IMCs nucleate inside the Ag layer, the same discussion as for the Ag / Sn bilayers would hold, i.e. initial nucleation of Ag_4Sn is favored. However, the additional driving force for Sn diffusion in the Ag layer, due to surface energy difference, does not operate in the Sn / Ag bilayers. Hence the mobility of the Sn atoms inside the Ag layer of the Sn / Ag bilayers is low, as Sn, moreover, diffuses substitutionally in Ag [62], as compared to the interstitial diffusion of Ag in Sn [105, 15]. Therefore, it is expected that for the Sn / Ag bilayers IMC formation occurs inside the Sn layer. In case of IMC nucleation inside the Sn layer (possibly with nucleation at the interface of the Ag and Sn layers), the Gibbs energy released per mole Ag atoms has to be considered. Additionally, due to the low solubility for Ag in Sn, the solid solution is practically pure Sn and therefore the Gibbs energies of formation from the pure elements can be used in a comparative discussion. The Gibbs energies of formation per mole Ag atoms are -5.6 ± 1 kJ mol^{-1} and -4.5 ± 1 kJ mol^{-1} for Ag_3Sn and Ag_4Sn, respectively (see paragraph above). Hence in this case the formation of Ag_3Sn is preferred, as observed.

Note that nucleation barriers, caused by the interfacial and misfit-strain energies that are associated with the nucleation of an IMC, are not taken into account in the discussion above [74].

It is recognized that in the very beginning of (IMC) product-layer growth the reactions at the interfaces always control the layer-growth kinetics until a changeover thickness x^* is surpassed, beyond which diffusion control prevails. If multiple, here two, IMC reaction layers can form, as in the current, binary Ag-Sn couples, it is possible that the kinetics of interface-controlled or even (see below) diffusion-controlled growth of one of the IMC layers is that fast that the formation of another, competing layer (which must initially

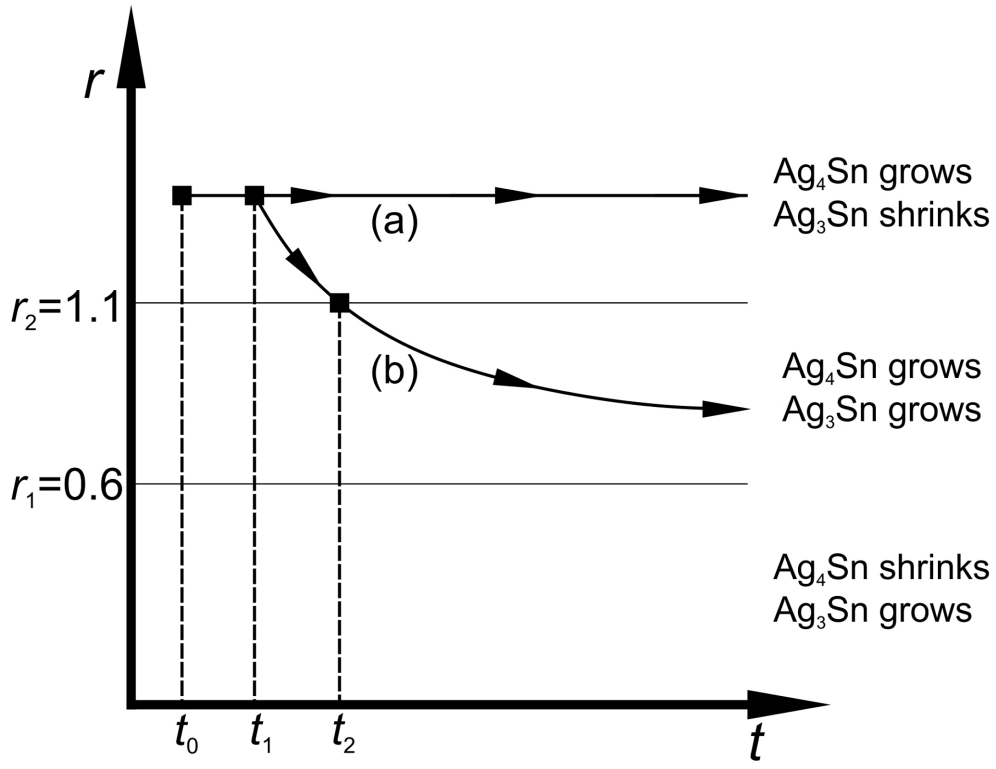

Fig. 2.12: The three different growth regimes as determined by the diffusional Ag flux ratio r of the (hypothetical) Ag_4Sn and Ag_3Sn IMC product layers developing in the Ag–Sn sample (see text and Eq. 2.6). A possible, schematic development of the flux ratio r as a function of time is shown. (a) The flux ratio for the Ag / Sn bilayers (Ag on top) is constant due to the maintenance of an interface-controlled nature of IMC growth for Ag_4Sn, which then is the only IMC product layer present. (b) The flux ratio for the Sn / Ag bilayers (Sn on top) changes with time; after an initial development of an Ag_4Sn layer growing under interface control, a transition to diffusion control occurs and r starts to decrease. If $r < r_2$, an Ag_3Sn layer is no longer kinetically unstable and both IMC layers can grow.

grow by interface control) is obstructed kinetically. Only if the first developed layer grows diffusion-controlled and surpasses a critical thickness x^{crit} (not to be confused with the changeover thickness x^* defining the transition of interface-controlled growth to diffusion-controlled growth for an individual layer, as indicated above), the second layer can form. The theoretical background for these considerations has in particular been provided in Refs. [80, 76]. In the following the treatment of Ref. [76] is adopted to find out, in addition to the above thermodynamic explanation for the preferred formation of either Ag_4Sn or Ag_3Sn, if kinetic arguments may also support the formation of Ag_4Sn with "Ag on top" and Ag_3Sn with "Sn on top".

To this end IMC formation in the model system Ag|Ag_4Sn|Ag_3Sn|Sn is considered. It is assumed that there is no uptake of Sn in the Ag layer and no uptake of Ag in the Sn layer during IMC growth. It follows that three different growth regimes can be distinguished,

depending on the ratio r of the fluxes of the Ag atoms across the Ag_4Sn ($j^{Ag}_{Ag_4Sn}$) and Ag_3Sn ($j^{Ag}_{Ag_3Sn}$) IMC layers:

$$r = \frac{j^{Ag}_{Ag_4Sn}}{j^{Ag}_{Ag_3Sn}}. \tag{2.3}$$

The three growth regimes are separated by the values of the flux ratios r_1 and r_2, which are defined by Ref. [76]:

$$r_1 = \frac{(1+\gamma)(\alpha-\beta)}{(1+\beta)(\alpha-\gamma)} \tag{2.4}$$

and

$$r_2 = \frac{(1+\gamma)(\beta-\delta)}{(1+\beta)(\gamma-\delta)}, \tag{2.5}$$

where α, β, γ and δ are the number of Ag atoms per Sn atom for the Ag, Ag_4Sn, Ag_3Sn and Sn phases, respectively. It holds (see Fig. 2.12):

$$r < r_1 \rightarrow Ag_3Sn \text{ grows; } Ag_4Sn \text{ shrinks} \tag{2.6a}$$

$$r_1 < r < r_2 \rightarrow Ag_3Sn \text{ grows; } Ag_4Sn \text{ grows} \tag{2.6b}$$

$$r > r_2 \rightarrow Ag_3Sn \text{ shrinks; } Ag_4Sn \text{ grows.} \tag{2.6c}$$

Adopting the concentrations for pure Ag, 85 at.% Ag for Ag_4Sn (both according to the results of the EDX measurements; see Fig. 2.3), stoichiometric Ag_3Sn and pure Sn, values for r_1 and r_2 of 0.6 and 1.1, respectively, are obtained.

If the thicknesses of both IMCs are smaller than the changeover thicknesses x^* (see above), the diffusional flux across the IMCs and thereby the growth of the IMCs is interface-controlled, which always holds during the initial stages of IMC-layer growth. In this case the ratio r is independent of the thicknesses of the two IMC layers and the flux ratio r is given by (cf. Eq. (32) in Ref. [76]):

$$r = \frac{\Delta C^{eq}_{Ag_4Sn} \kappa^{eff}_{Ag_4Sn}}{\Delta C^{eq}_{Ag_3Sn} \kappa^{eff}_{Ag_3Sn}}, \tag{2.7}$$

where $\Delta C^{eq}_{Ag_4Sn}$ and $\Delta C^{eq}_{Ag_3Sn}$ are the equilibrium concentration differences across the Ag_4Sn and Ag_3Sn IMC layers, respectively (i.e. "so-called" local equilibrium is supposed at the interfaces [76]), and $\kappa^{eff}_{Ag_4Sn}$ and $\kappa^{eff}_{Ag_3Sn}$ are the effective reaction rate constants for Ag_4Sn and Ag_3Sn formation (cf. Eqs. (4), (5) and (7) in Ref. [76]). The values of $\Delta C^{eq}_{Ag_4Sn}$ and $\Delta C^{eq}_{Ag_3Sn}$ are estimated here, using data from Ref. [54], as 5 at.% and 1 at.%, respectively. The effective reaction rate constant for the Ag_4Sn formation at its interfaces, $\kappa^{eff}_{Ag_4Sn}$, is expected to be larger than that for Ag_3Sn formation at its interfaces, $\kappa^{eff}_{Ag_3Sn}$, due to the ordered structure of the Ag_3Sn IMC. Therefore, as long as the fluxes

through both IMCs are interface controlled, i.e. during the initial stages of the growth of the IMCs, flux ratios r much larger than $r_2 = 1.1$ are expected (cf. Eq. 2.7). The Ag_3Sn IMC is therefore "kinetically unstable" (see above and cf. Eq. 2.6a and Fig. 2.12): even if it would nucleate after the nucleation of the Ag_4Sn IMC, it cannot practically coexist together with the growing Ag_4Sn IMC layer. Hence, for both the Ag / Sn and the Sn / Ag bilayers, after the onset of IMC growth as indicated by t_0 in Fig. 2.12, only Ag_4Sn is present.

In order that, eventually, an Ag_3Sn layer could develop yet, the growth rate of the Ag_4Sn layer must decrease, which will happen for a thickening Ag_4Sn layer once its growth has become diffusion controlled. To this end first the changeover thickness $x^*_{Ag_4Sn}$ for the Ag_4Sn layer must be surpassed.

It is now recalled that, in reality, in particular for the Ag / Sn bilayer system (i.e. "Ag on top"), an enhanced, as compared to "Sn on top", diffusional flux through the Ag_4Sn layer occurs, driven by the surface-energy difference of Ag and Sn (see Section 2.4.1). This will unavoidably delay the transition from interface-controlled growth to diffusion-controlled growth for the Ag_4Sn layer in case of "Ag on top" as compared to "Sn on top". Evidently, growth of Ag_4Sn for "Ag on top" likely remains interface-controlled at least until the deposition process has been completed and the flux ratio remains at its constant value (>1.1) as assesed above (see line (a) in Fig. 2.12) or, if the changeover thickness would have been surpassed yet during deposition, the r value decreases already but is still larger than r_2 (cf. Eq. 2.6c). Hence the IMC Ag_3Sn cannot be observed in the as-deposited state in the case of the Ag / Sn bilayers.

In case of the Sn / Ag bilayers (Sn on top), much less Sn is diffusing into the Ag sublayer (see above and Section 2.4.1), and hence the transition from interface-controlled growth to diffusion-controlled growth can take place for the Ag_4Sn layer during deposition. The time of the transition to diffusion-controlled growth for the Ag_4Sn layer has been indicated with t_1 in Fig. 2.12. The flux ratio r (see below) now steadily decreases. Once it has become smaller than r_2 an Ag_3Sn layer can form (Eq. 2.6b and Fig. 2.12). Its growth at this stage is interface-controlled, due to its vanishing thickness.

In the case of diffusion-controlled growth of Ag_4Sn and interface-controlled growth of Ag_3Sn the flux ratio r is given by Eq. 2.8.

$$r = \frac{\Delta C^{eq}_{Ag_4Sn} \tilde{D}_{Ag_4Sn}}{\Delta C^{eq}_{Ag_3Sn} \kappa^{eff}_{Ag_3Sn} x_{Ag_4Sn}} \tag{2.8}$$

here, $\tilde{D}_{Ag_4Sn}$ is the interdiffusion coefficient in the Ag_4Sn IMC and x_{Ag_4Sn} is its thickness. Note that the present case is different from the one treated in Section III E in Ref. [76]. In the latter case the IMC corresponding to Ag_3Sn ($A_\gamma B$ in Ref. [76]) is treated as

growing diffusion-controlled, while the IMC corresponding to Ag_4Sn ($A_\beta B$ in Ref. [76]) is treated as growing interface-controlled. Hence, Eq. 2.8 differs from Eq. (33) in Ref. [76]. However, Eq. 2.8 can be directly derived from Eqs. (17), (18) and (24) in Ref. [76]. As follows from Eq. 2.8, the flux ratio r decreases with increasing thickness of the Ag_4Sn IMC layer, x_{Ag_4Sn}, as indicated by line (b) in Fig. 2.12. At the time t_2 r will drop below $r_2 = 1.1$ (see Fig. 2.12) and beyond that time simultaneous growth of the Ag_3Sn IMC and the Ag_4Sn IMC is possible (provided that nucleation of Ag_3Sn is possible). On this basis the observed presence of the Ag_4Sn and Ag_3Sn IMCs in the as-deposited state of the Sn / Ag bilayers (Sn on top) can be understood.

2.5 Conclusions

For evaporated Ag–Sn bilayers the phases present in the as-deposited state depend on the stacking sequence of the individual sublayers.

In case of Ag on top of Sn, a considerable amount of Ag_4Sn is present, whereas in the case of Sn on top of Ag predominantly Ag_3Sn is present, together with a small amount of Ag_4Sn.

In case of the Ag on top of Sn bilayers, the Ag_4Sn formation is accompanied by a large uptake of Sn into the growing Ag layer, leaving behind macroscopic Kirkendall voids in the Sn layer. Apart from the driving force for interdiffusion due to the Gibbs energy of mixing, in case of Ag on top of Sn an additional driving force is caused by the difference in surface energy of Sn and Ag. This leads to the observed large uptake of Sn in Ag for the case of Ag on top of Sn. In the opposite case of Sn on top of Ag, no such additional driving force for Sn uptake by Ag is present.

Thermodynamic argumentation shows that in case of Ag on top of Sn, Ag_4Sn is formed preferentially, as observed. Moreover, kinetic analysis indicates that, upon IMC layer growth in the initial stage of interface-controlled growth, a possibly present Ag_3Sn layer is kinetically unstable, i.e. it does not develop, whereas the Ag_4Sn layer grows.

Also on a thermodynamic basis it can be argued that the observed preferred formation of Ag_3Sn in case of Sn on top of Ag, indicates that Ag_3Sn develops within the Sn sublayer. Moreover, kinetic analysis indicates that the transition to a stage of diffusion-controlled growth for the first-developed Ag_4Sn layer takes place, at a (much) earlier stage for the Sn on top of Ag bilayers, thus leading to the observed development of Ag_3Sn.

Strikingly, both thermodynamics and kinetics predict the same, observed dependence of the emergence of the intermetallic compound product layers on the sublayer stacking sequence.

2.6 Acknowledgements

The authors thank Dr. G. Richter (Max Planck Institute for Intelligent Systems) for providing access to the thermal evaporation apparatus, as well Mrs. U. Eigenthaler (Max Planck Institute for Intelligent Systems) for the preparation of the TEM-specimens as well as the Dual-Beam images. The authors are also grateful to K. Hahn (STEM group Max Planck Institute for Intelligent Systems) for performing the S-TEM EDX measurements.

Chapter 3

Effects of deposition method on the microstructure and intermetallic compound formation in Ag–Sn bilayers

P.J. Rossi[1], N. Zotov[1] and E.J. Mittemeijer[1,2]

[1] *Max Planck Institute for Intelligent Systems (formerly Max Planck Institute for Metals Research), Heisenbergstraße 3, D-70569 Stuttgart, Germany*

[2] *Institute for Materials Science, University of Stuttgart, Heisenbergstraße 3, D-70569 Stuttgart, Germany*

Abstract

Thermal evaporation and magnetron sputtering were used for the deposition of bilayers of Ag and Sn with different stacking sequences of the sublayers, Ag on Sn (Ag / Sn) or Sn on Ag (Sn / Ag). The deposition method used significantly affects the intermetallic compound (IMC) formation in these thin films already during film deposition. Comparison of the corresponding microstructures and textures indicates that the observed, striking differences in IMC formation for the case of Ag / Sn bilayers can be related to the interplay of Sn upward diffusion, surface energy and interfacial intermixing for the two deposition methods.

3.1 Introduction

The Sn–Ag and Sn–Ag–Cu alloy systems are promising lead-free solder systems for electronic packaging processes [21, 31, 125, 30]. Ag–Sn alloy nanoparticles are candidates for electrocatalysts and for inkjet printing materials [126, 127, 128]. The Ag–Sn system is an important model system for studying fast diffusion and growth kinetics of intermetallic compound (IMC) formation at room temperature [24, 2]. Understanding of Ag–Sn IMC growth kinetics is essential for optimization of soldering parameters because the formation of IMCs, like Ag_3Sn and/or Cu_6Sn_5, can significantly affect the mechanical properties and the lifetime of Sn–Ag–Cu solders [41, 45]. Generally in *bulk* Sn–Ag–Cu

solders, prepared by solidification, formation of only Ag_3Sn IMC is observed, as may be anticipated on the basis of the Ag–Sn phase diagram [129]: in Sn–Ag–Cu solders with low Ag content (<3.5 wt.% Ag) a thin Ag_3Sn IMC layer is formed [46], whereas in case of higher Ag content (>3.5 wt.% Ag) large Ag_3Sn platelets are formed, especially at the solder-reaction layer interfaces [42]. However, Ag_4Sn IMC was reported at room temperature (RT) in Sn–Ag–Cu/Ag couples, prepared by dipping (for 5 s) of Ag slabs (providing excess Ag) in molten Sn–Ag–Cu solder and subsequent solidification [130]. Interestingly, formation of Ag_4Sn IMC in Ag–Sn nanoparticles with average composition $Ag_{60}Sn_{40}$ was reported in Ref. [128], which was attributed to the *increased solubility* limit of Sn in Ag in nanoparticles.

IMC formation in thick electroplated Ag–Sn bilayers has been discussed controversially in the literature. Ag–Sn IMC layer growth was not detected in Sn 6-10 μm / Ag 1.5-2 μm bilayers electroplated on Cu substrates at RT [131], whereas Ag_3Sn formation was observed in a Sn 1 μm / Ag 4 μm bilayer electroplated on a Ni-coated Cu substrate [83], as well as after annealing at 200 °C of electroplated Sn 6 μm / Ag 14 μm bilayers [132]. Preparation of Sn–Ag–Cu solders by codeposition also leads to formation of only Ag_3Sn IMC [133].

For some thin film bi- and multilayer systems like Mo–Si and Cu–Si [120, 119], it has been reported that the IMC formation depends on the stacking sequence. X-ray diffraction (XRD) of thin Ag–Sn bilayers (thickness ∼70 nm) with different stacking sequences: Ag on top (Ag / Sn) and with Sn on top (Sn / Ag), prepared by thermal evaporation (TE) and *stored* for 24 h at RT in vacuum, showed no effect of the stacking sequence [134]. In both cases (Sn / Ag and Ag / Sn) only Ag_3Sn IMC was observed [134]. More recently it has been demonstrated [121] that IMC formation in TE Ag–Sn bilayers in the '*as-deposited state*', can depend on the stacking sequence: in Sn / Ag bilayers predominantly Ag_3Sn IMC is formed, whereas in Ag / Sn bilayers predominantly Ag_4Sn IMC is formed.

The influence of intrinsic kinetic aspects of the physical vapor deposition (PVD) process on the IMC formation in these TE experiments cannot be ruled out without more ado. In the present paper the phase composition, morphology and texture of Sn / Ag and Ag / Sn bilayers in the *as-deposited state*, as grown by thermal evaporation and by direct current (DC) magnetron sputtering (MS), are compared, in order to expose the influence of specific deposition parameters on especially the IMC formation, recognizing that thin films grown by TE and MS show distinct differences in structure and morphology [89, 90]. The results obtained can be relevant for better understanding and optimization of the so-called diffusion soldering technique based on the interdiffusion in thin-film bilayer and multilayer systems consisting of high- and low-melting materials [83].

3.2 Experimental

Bilayer (Ag / Sn and Sn / Ag) thin films with 500 nm thickness of the two sublayers were prepared by TE and MS. Thermal evaporation was performed with a Lesker Nano 36 evaporator. Separate open dimple boats (Lesker, USA) made of Mo and W were used for evaporation of Sn (99.999 wt.% purity, Heraeus) and Ag (99.99 wt.% purity, Lesker), respectively. The dimple boats were mounted symmetrically at both sides of the rotation axis (30 rpm) of the substrate holder, placed approximately 35 cm above the boats. The deposition rates were monitored by a quartz crystal balance and calibrated separately for Sn and Ag by measuring the thickness of single and bilayers using a Dektak 8 profilometer (Vecco). The depositions of the sublayers were carried out without breaking the vacuum, at pressures in the range from 0.6×10^{-5} to 2.6×10^{-3} Pa at RT. Si (100) wafers, covered with a 50 nm amorphous SiO_2 buffer layer, served as substrates. Before deposition the substrates were cleaned using a wet chemical cleaning procedure, followed by oxygen-plasma cleaning for 10 min. The TE Sn / Ag bilayer was evaporated using a deposition rate of 23 Å/s for Sn and a deposition rate of 8 Å/s for Ag. The TE Ag / Sn bilayer was evaporated using 8 Å/s deposition rate for Ag and 12 Å/s deposition rate for Sn. The higher deposition rate for the Sn sublayer of the TE Sn / Ag bilayer was used in order to reduce the surface roughness (it was established that the roughness of evaporated Sn single layers decreases monotonically with increasing deposition rate). The temperatures of the melts in the dimple boats were measured using an IR thermoscope GD8501 (Goscam, China).

DC MS was performed with a PVD 75 coater (Lesker, USA) using 2 separate targets (diameter 5.08 cm). The planar magnetrons were inclined at 25° with respect to the surface of the substrate. Base pressure was 4×10^{-4} Pa. Ag (99.99 wt.% Ag purity, Lesker) was sputtered under an Ar pressure of 0.27 Pa with a DC power of 100 W, with a deposition rate of 3.1 Å/s. Sn was sputtered under an Ar pressure of 0.29 Pa with a DC power of 50 W, with a deposition rate of 2.4 Å/s. The substrates (glass substrates or Si (111) wafers with 50 nm amorphous SiO_2 layer on top of a 50 nm Si_3N_4 layer), cleaned using a wet chemical procedure, were mounted 17 cm above the target and rotated (at 10 rpm) during deposition.

3.3 Results

Phase analysis of the thin films was performed by XRD using a Bruker TXS D8 Discover diffractometer with Cu-K_α radiation from a rotating anode X-ray tube. The diffractometer was equipped with a Xenocs Fox 2D collimating mirror in the incident beam and a

VÅNTEC-500 2D detector in the diffracted beam. The 2D detector allowed rapid data acquisition (120 s counting time per frame) [135]. The intensities recorded by the 2D detector were converted into conventional XRD diffractograms by integrating along the Eulerian angle from 73.8° to 106.6°, using the GADDS software (Ver. 4.0, Bruker AXS, 1999). The XRD measurements with the Bruker TXS D8 diffractometer were made in the 'as-deposited state' typically 15–20 min after bilayer deposition. Ag (111) and Sn (100) pole figures were recorded with a Philips (PANalytical) MRD Pro diffractometer using Co-K_α radiation. The MRD diffractometer was equipped with a polycapillary X-ray collimator in the incident beam as well as a graphite monochromator and a proportional point detector in the diffracted beam.

Cross-sections of the bilayers (covered with a protective Pt layer) were prepared and corresponding micrographs were made with a focused ion beam/scanning electron microscope (FIB/SEM) FEI Nova Nanolab 600 Dual-Beam instrument. Interdiffusion in the Ag–Sn bilayers takes place rapidly even at RT [24, 2]. That is why the results from FIB/SEM represent an early aging stage.

The XRD patterns of Sn / Ag and Ag / Sn bilayers, deposited by TE and MS, show (Fig. 3.1) that MS leads to the formation of predominantly Ag_3Sn IMC for both types of bilayers, whereas the predominant IMC formed in the TE bilayers depends on the sublayer stacking sequence: Ag_3Sn in the TE Sn / Ag bilayers and Ag_4Sn in the TE Ag / Sn bilayers[1]. Most probably IMC formation starts already during deposition.

The XRD patterns of the TE Ag / Sn bilayers show, in addition, the presence of diffuse scattering between the Ag_4Sn (011) and the Ag (200) peaks. Since the main difference in IMC formation is observed for the TE and MS modes of deposition of the Ag / Sn bilayers, the texture of this type of bilayers will be considered preferentially below.

The relative intensities of the Sn and Ag diffraction peaks (Fig. 3.1b) and the pole figures (Fig. 3.2) indicate substantial differences in the preferred orientation of the Ag and Sn sublayers in the TE and MS Ag / Sn bilayers.

The TE Ag / Sn bilayers exhibit very strong and sharp Ag {111} and Sn {100} fiber textures, whereas the MS Ag / Sn bilayers exhibit very weak and broad fiber (almost random) textures.

The microstructures of the TE and MS bilayers also show significant differences. In the TE bilayers the interfaces between the two sublayers are rather sharp for both stacking sequences (Figs. 3.3a and 3.4a). Large grains can be seen in the Sn bottom layer (Fig. 3.3a). The homologous temperature T/T_m, where T_m is the melting temperature of the

[1]The deposition rate for the Sn layer in the TE Sn / Ag bilayer was 23 Å/s, whereas a deposition rate of 12 Å/s was used for the Sn layer in the TE Ag / Sn bilayer, because the Sn top layer, deposited with 12 Å/s, does not form a continuous layer.However, it was established that the same type of IMC formed (Ag_3Sn) in the case of lower (12 Å/s) deposition rate for the Sn top layer.

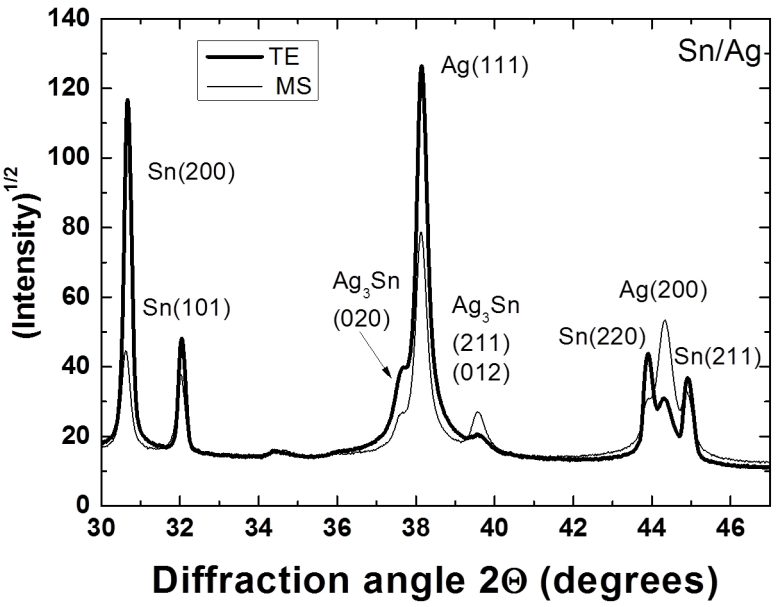

(a)

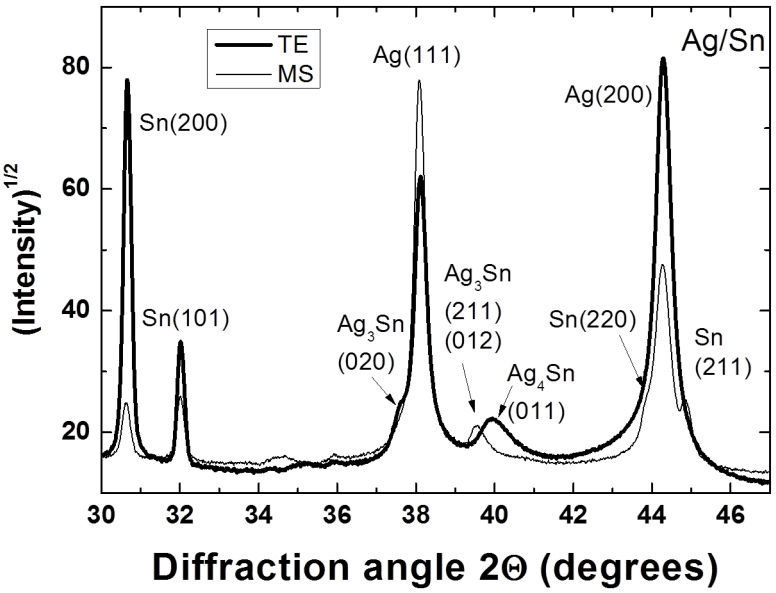

(b)

Fig. 3.1: XRD patterns of thermally evaporated (TE) and magnetron sputtered (MS) (a) Sn / Ag bilayers and (b) Ag / Sn bilayers.

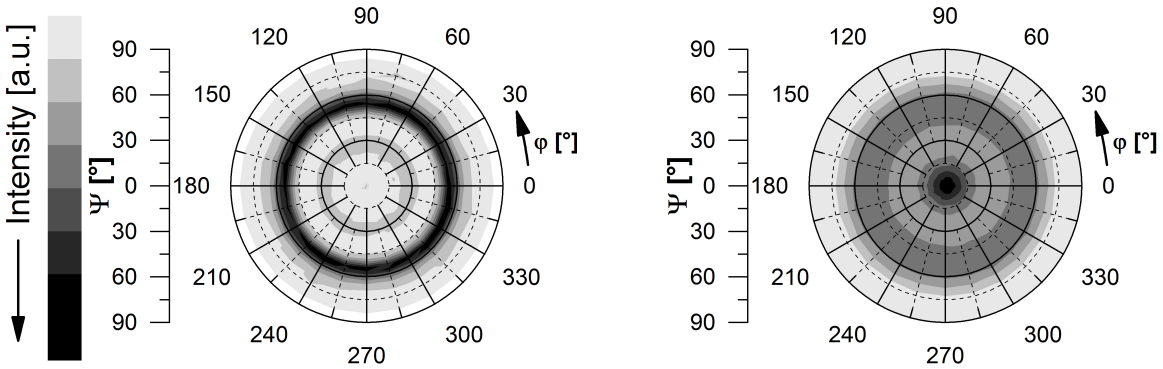

(a) left: TE Ag (111), right: MS Ag (111)

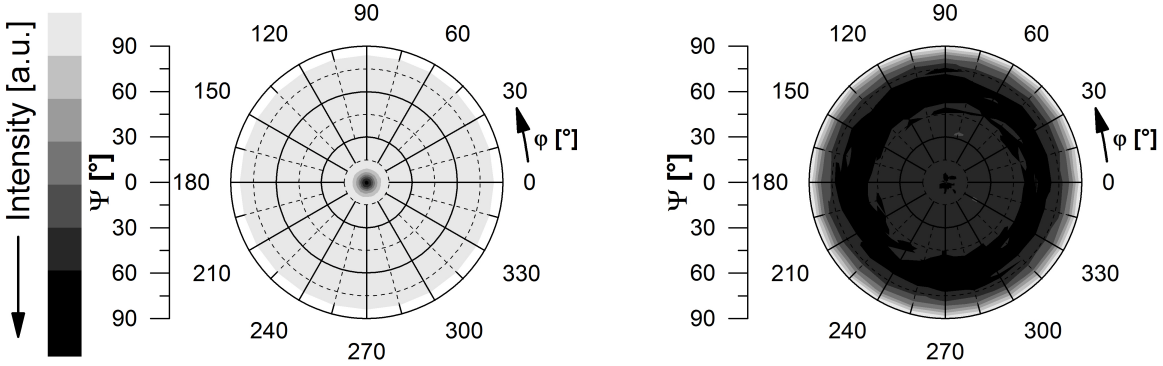

(b) left: TE Sn (100), right: MS Sn (100)

Fig. 3.2: (a) Ag (111) pole figures and (b) Sn (100) pole figures for TE (left) and MS (right) Ag / Sn bilayers.

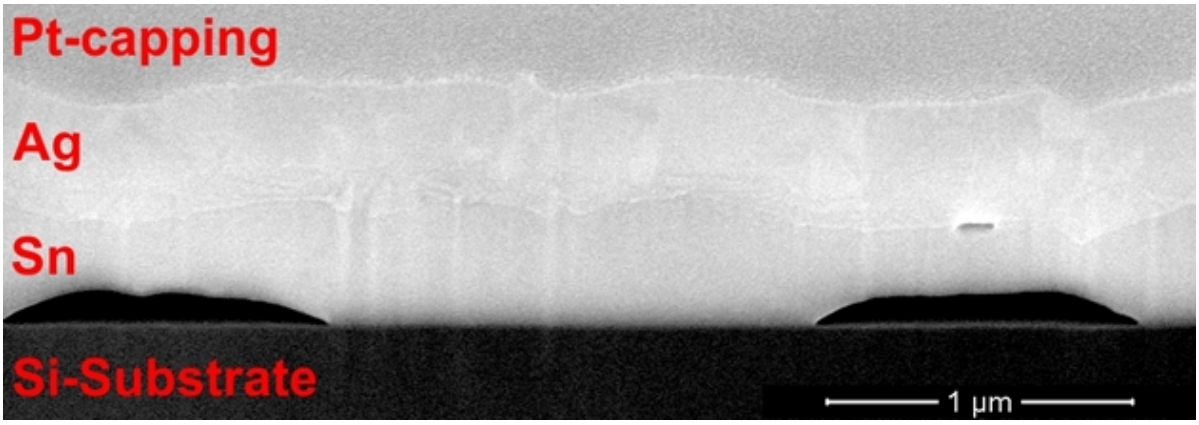

(a)

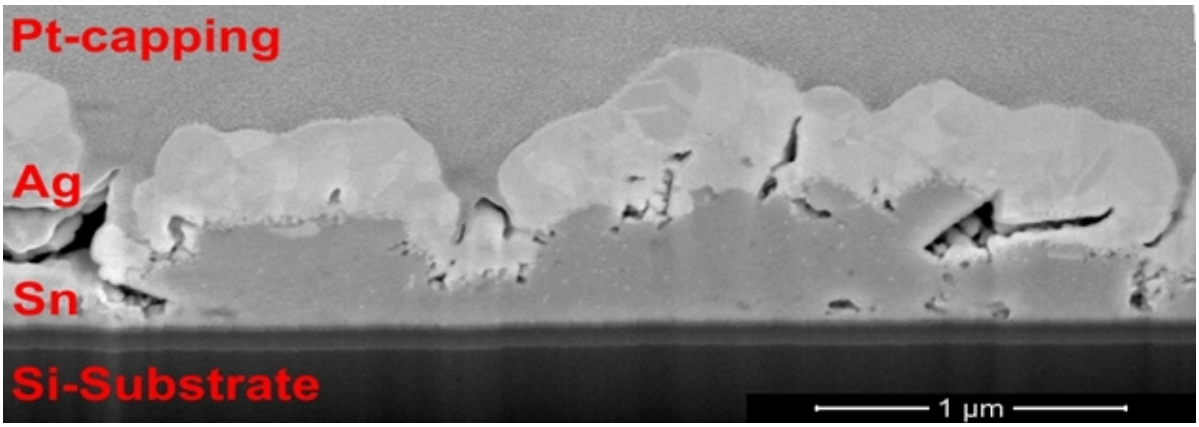

(b)

Fig. 3.3: SEM images, taken with the Dual Beam instrument, of Ag / Sn bilayers deposited by (a) thermal evaporation (TE) and (b) magnetron sputtering (MS).

element, for the Sn evaporation was ∼0.63, which corresponds to Zone 3 of the zone model for *evaporated* thin films [88], where extensive grain growth dominates. Large (Kirkendall) macroscopic voids are observed adjacent to the Si substrate. Kirkendall voids in the Sn sublayer were also observed in Refs. [46, 83]. In the TE Sn / Ag bilayer (Fig. 3.4a), the Ag bottom layer shows columnar growth with average columnar width of about 90 nm and presence of both large and small grains. The homologous temperature T/T_{m}, where T_{m}, for the Ag evaporation was ∼0.24, which corresponds to Zone T of the zone model for *evaporated* thin films [88], where a bimodal grain size distribution is observed.

In the MS bilayers, the interfaces between the Ag and Sn sublayers are rather rough, wavy and the sublayers contain a significant amount of defects, microvoids and microcracks for *both* stacking sequences (Figs. 3.3b and 3.4b). Both the Sn and Ag grains (columns) of the top layers are domed, resembling zone Ic of the extended structure zone model for *sputtered* thin films, presented in Ref. [136]. It is noted that microstructural

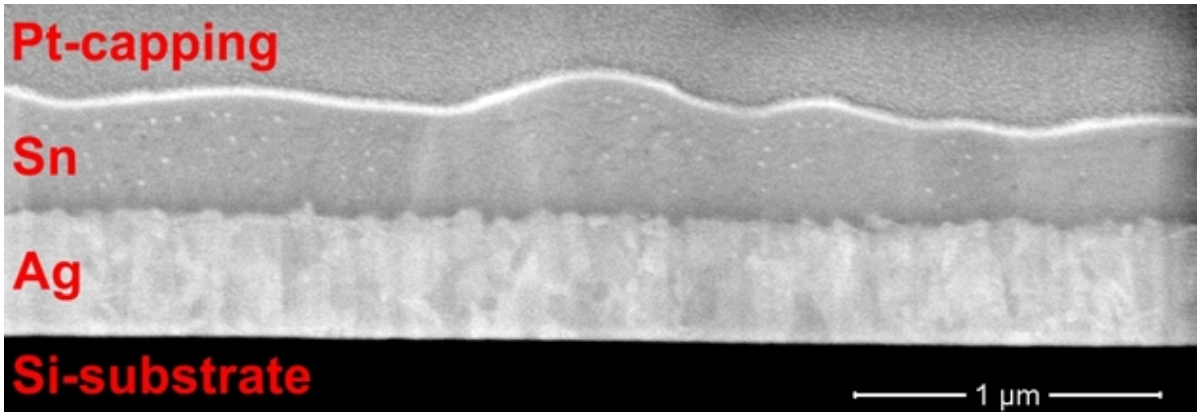

(a)

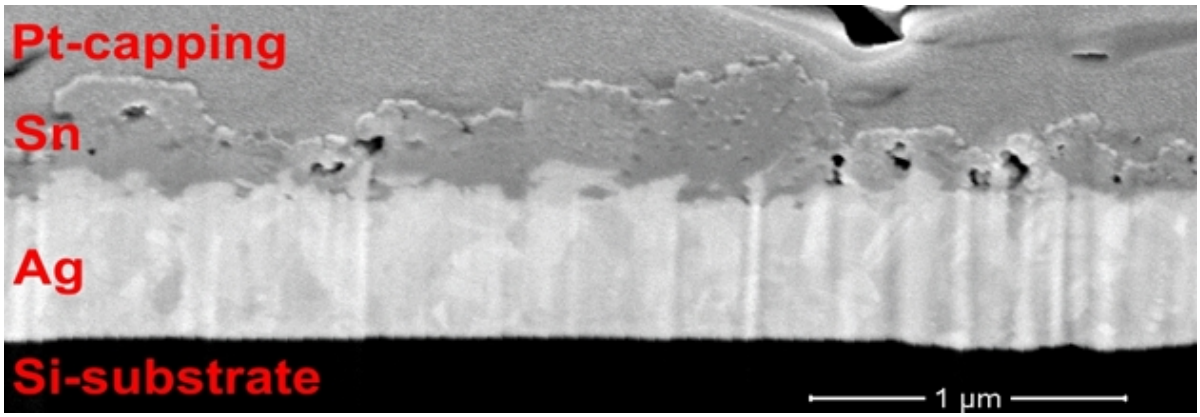

(b)

Fig. 3.4: SEM images, taken with the Dual Beam instrument, of Sn / Ag bilayers deposited by (a) thermal evaporation (TE) and (b) magnetron sputtering (MS).

characterization on the basis of the homologous temperatures, as within structural zone models, has limitations [137].

3.4 Discussion

Thermodynamically, the main difference in the microstructural evolution of the Ag / Sn and Sn / Ag bilayers during deposition for both PVD methods is the presence of an additional driving force, acting in the Ag / Sn bilayers, for Sn upward diffusion through the growing Ag sublayer to its surface, due to the large difference in the surface energies of Sn and Ag (0.675 J/m^2 and 1.250 J/m^2 [115], respectively). The upward (bulk and grain boundary) Sn diffusion through the growing Ag layer reduces the surface energy of the whole system. This is exactly the case for TE Ag / Sn bilayers. The upward Sn diffusion creates an opposite (downward) vacancy flux in the Sn sublayer (Ag does not dissolve substantially (and moreover interstitially) in Sn [129]). Large Kirkendall voids

form (see Fig. 3.3a) upon coalescence of these vacancies in the TE Ag / Sn bilayers. No large Kirkendall voids are observed in the case of both TE and MS Sn / Ag bilayers, because there is no additional driving force for surface energy reduction in this case.

A high density of stacking faults likely forms in the TE Ag / Sn bilayers because the already low stacking fault energy of Ag ($\sim 21 \pm 4$ mJ/m^2 [138]) becomes even smaller with increasing Sn concentration [109, 110], consistent with the pronounced diffuse scattering observed in the corresponding TE Ag / Sn XRD patterns (see Fig. 3.1b, Section 3.3). The presence of stacking faults with hexagonal closed-packed (hcp) stacking sequences facilitates the nucleation of fcc–hcp transformation in fcc metals [139] and in the present case likely favors the formation of the disordered Ag_4Sn phase, which has a *hexagonal* structure (Mg-type, space group $P6_3/mmc$ [51]), rather than formation of the Ag_3Sn phase, which has an ordered orthorhombic structure (β-Cu_3Ti-type, space group $Pmmn$ [108]).

The different effects of the TE and MS deposition processes on the IMC formation in the Ag / Sn bilayers (see Section 3.3) are likely related to differences, discussed below, in the TE and MS deposition parameters (deposition rate, vacuum, particle energies, bombardment of the sublayer), which apparently suppress the formation of the Ag_4Sn IMC in the MS case.

Generally, deposition rates for MS are lower than for TE, due to scattering of the sputtered target atoms by the sputtering (Ar) gas. The present MS Ag / Sn bilayers were deposited with lower Ag deposition rates (3.1 Å/s) than the TE Ag / Sn bilayers (8 Å/s). TE Ag / Sn bilayers, deposited with 4, 8 and 15 Å/s Ag deposition rates in this project, show that the amount of the Ag_4Sn IMC increases with decreasing Ag deposition rate (as qualitatively deduced from the intensity of the (011) Ag_4Sn diffraction peak; see Fig. 3.5). Hence, the lower value of the Ag deposition rate for the MS bilayers cannot be the primary cause for the emergence of the Ag_3Sn IMC (in MS bilayers) instead of the Ag_4Sn IMC (in TE bilayers).

Generally, TE is performed at a higher vacuum (0.6×10^{-5}–2.6×10^{-3} Pa in the present case) than MS (0.28 Pa in the present case). The lower vacuum during MS could lead to some oxygen contamination of the growing film, which might affect (reduce) the upward diffusion of Sn in the case of the MS Ag / Sn bilayers; but no additional oxide phases were detected by XRD analysis, so likely this is also not a primary cause for the differences in the IMC formation observed.

The kinetic energies of the atoms in the vapor phase during TE and MS are quite different. In order to estimate the energies of Ag and Sn in the vapor phase in the case of TE, the following approach was used. The vapor pressure during TE for most materials should be at least 1.3 Pa to achieve deposition rates suitable for practical

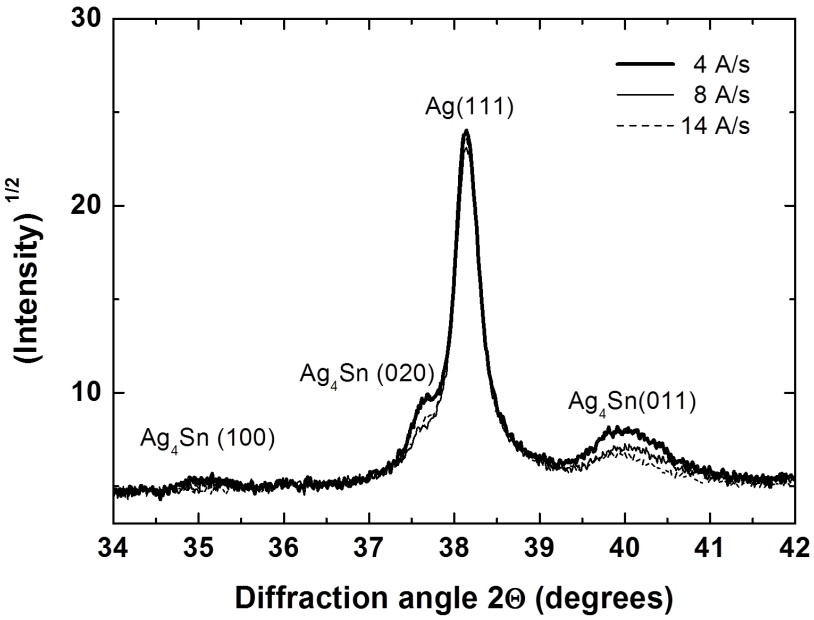

Fig. 3.5: XRD patterns of TE Ag / Sn bilayers deposited with 4 Å/s (thick line), 8 Å/s (thin line) and 15 Å/s (dashed line). Only the range 34–42° 2θ (Cu-K_α radiation) is shown to better expose the dependence of the intensity of the Ag_4Sn (011) peak on the deposition rate.

applications [140]. The melt temperatures at this vapor pressure are 1299 K for Ag and 1510 K for Sn [141], respectively. These values are in reasonable agreement with the present experimental values of 1373 ± 150 K for Ag and 1623 ± 150 K for Sn (due to the experimental errors arising from uncertainties in the optical emissivities of the melts and the absorption in the window of the deposition chamber, the temperatures of the melts were estimated from the vapor pressure). These temperatures correspond to kinetic energies of 0.14 eV for Ag and of 0.17 eV for Sn (calculated from the mean value $E_{\mathrm{TE}} = 4/\pi\ kT$, where k is the Boltzmann constant, of the Maxwellian distribution, which the evaporated atoms obey away from the liquid-vapor interface [142]).

Monte Carlo simulations of MS processes (e.g. Ref. [143]), have shown that the kinetic energy of atoms striking the substrate with masses larger than that of Ar, decreases with increasing atomic number Z. Therefore, it can be expected that the average kinetic energy (E_{MS}) of the sputtered Ag atoms ($Z = 47$) arriving at the substrate will be (slightly) larger than that of the sputtered Sn atoms ($Z = 50$), both kinetic energies being in the range 10–12 eV (for an Ar pressure of about 0.28 Pa) [143]. It should be noted that the energy distribution of the sputtered atoms (Sn or Ag) arriving at the substrates always contains long tails of highly energetic particles ($E_{\mathrm{MS}} > 20$ eV).

The much higher kinetic energies of the sputtered Ag atoms (10–12 eV) in the case of MS, compared to TE (0.14 eV), as well as the presence of Ar atoms impinging on

the Sn bottom layer, can lead to enhanced Ag–Sn intermixing at the interface by both *penetration* of Ag atoms into the Sn bottom layer (although the solubility of Ag in Sn is negligible [129]) and by *resputtering* of Sn atoms into the growing Ag layer. The *enhanced intermixing* of Ag and Sn at the interface during MS Ag top layer growth may lead to reduction of the surface energy of the system (by alloying of Ag with Sn) without the necessity for *substantial* upward diffusion of Sn as in the case of TE Ag / Sn bilayers. The bombardment with Ag as well as Ar atoms of the soft Sn bottom layer also creates more defects in the material at the interface (see Fig. 3.3b), which could reduce the nucleation barrier for nucleation of the more complex (ordered) Ag_3Sn IMC, as compared to the Ag_4Sn IMC. The slightly lower kinetic energy of the Sn atoms during MS (see above) suggests that the material at the interface of the MS Sn / Ag bilayers should contain less defects than of the MS Ag / Sn bilayers, in qualitative agreement with the microstructures observed in Figs. 3.3b and 3.4b.

In addition, computer simulations of Ag {111} growth show that evaporation produces atomic structures with stacking faults, whereas sputtering produces atomic structures without stacking faults, due to the increased kinetic energy of the atoms in the latter case [91]. Indeed, no diffuse scattering (associated with stacking faults) is observed in the XRD patterns of the MS bilayers (Fig. 3.1). As a result of the combined effect of these three factors (decrease of the surface energy of the system due to enhanced intermixing, decrease of the nucleation barrier for nucleation and likely the lack of stacking faults), the formation of the orthorhombic Ag_3Sn IMC can be kinetically favored in the case of MS over the formation of the hexagonal Ag_4Sn IMC.

TE Sn single- and bottom sublayers always show strong and sharp {100} fiber texture (Fig. 3.2), whereas TE Ag bottom sublayers have a {111} fiber texture, because the low kinetic energy of the evaporated atoms leads to layer-by-layer growth with the most dense crystallographic planes parallel to substrate ((100) in the case of Sn and (111) in the case of Ag). Ag thin films, grown on amorphous-SiO_2 buffer layer, as in the present case, by molecular beam epitaxy (where the adatoms possess also low kinetic energies) show strong {111} fiber-textured microstructures as well [137].

The MS Sn and Ag bottom sublayers are both untextured, because the constant bombardment of the growing layer with high energetic particles as well as the higher surface diffusion facilitate the nucleation, inducing a more random texture. Indeed, transmission electron microscopy (TEM) showed, for example, that in the early stages of Ag layer growth the density and mobility of atoms and islands for sputtered Ag are higher than that for evaporated Ag [92] (sputtering of Au also produces thin films with small grains and no crystallographic texture [89]). Indeed, absence of preferred orientation is characteristic for zone Ic for *sputtered* structures because the growth mode is based on

shadowing effects (inclined magnetrons, see Section 3.2) rather than on, e.g., anisotropy of growth rates for different crystallographic planes [136]. Computer simulations have shown that the Sn (100) planes have the lowest surface energy compared to other crystallographic planes like (101), (210), (110), (201) etc. [144]. This result implies that the much more random orientation of the Sn grains in the case of MS would lead to a slightly higher average surface energy of the MS Sn bottom bilayer, compared to the TE Sn bottom layer possessing strong {100} fiber texture (Fig. 3.2b). A higher average surface energy of Sn in the MS Ag / Sn bilayers reduces the surface energy gradient over the Ag sublayer and thus, indirectly (see above), makes the formation of the Ag_4Sn IMC in the case of MS less likely.

3.5 Conclusions

Comparison of the phase constitution and morphology of thermally evaporated (TE) and magnetron sputtered (MS) Ag–Sn bilayers with different stacking sequences in the '*as-deposited*' state reveals distinct differences between the TE and MS bilayers. The intermetallic compound (IMC) formation in the Sn / Ag bilayers (Sn on top) is the same for both types of PVD processes (predominantly Ag_3Sn IMC formation), whereas in the Ag / Sn bilayers (Ag on top) the IMC formation depends on the PVD process: Ag_4Sn IMC formation in the case of TE Ag / Sn bilayers and Ag_3Sn IMC formation in the case of MS Ag / Sn bilayers. The interfaces between the two sublayers are (relatively) sharp in the case of TE bilayers and rather wavy, with high concentration of defects in the material at the interface, in the case of MS bilayers, *regardless* of the stacking sequence.

In TE Ag / Sn bilayers, the interface intermixing is expected to be rather small and Sn upward diffusion, driven by a difference in surface energy, generates high density of stacking faults, likely to promote formation of Ag_4Sn over Ag_3Sn IMC.

In MS Ag / Sn bilayers, the decrease of the surface energy as a result of enhanced intermixing (due to the *high kinetic energy* of the Ag atoms); the decrease of the nucleation barrier due to high (interfacial) density of defects and the lack of stacking faults in the MS Ag sublayer, all favor the formation of Ag_3Sn over the Ag_4Sn IMC.

3.6 Acknowledgments

The authors thank Dr. G. Richter for the access to the Lesker Nano evaporator, R. Völker for the preparation of the magnetron sputtering specimens and U. Eigenthaler for preparation of the Dual-Beam cross-sections.

Chapter 4

Kinetics of Intermetallic Compound Formation in Thermally Evaporated Ag–In Bilayers

P.J. Rossi[1], N. Zotov[1] and E.J. Mittemeijer[1,2]

[1] *Max Planck Institute for Intelligent Systems (formerly Max Planck Institute for Metals Research), Heisenbergstraße 3, D-70569 Stuttgart, Germany*

[2] *Institute for Materials Science, University of Stuttgart, Heisenbergstraße 3, D-70569 Stuttgart, Germany*

Abstract

The kinetics of intermetallic compound (IMC) formation in thermally evaporated Ag-In bilayers, with In on top of Ag, was investigated using X-ray diffractometry (XRD), applied to the surfaces of the bilayer specimens, as well as scanning electron microscopy, applied to cross-sections of the bilayer specimens, prepared by a focused ion beam (FIB) instrument. IMC formation was followed at room temperature (RT) as well as at elevated temperatures of 50°C, 60°C and 70°C. Two distinct growth regimes were observed coinciding with the availability of pure In. The $AgIn_2$ IMC nucleated initially, followed by nucleation of the Ag_2In IMC. The growth of $AgIn_2$ was found to be controlled by both diffusional processes as well as interfacial reactions. The growth of the Ag_2In IMC is dominantly diffusion-controlled. An interdiffusion coefficient of $D = 1.1 \pm 3.9 \cdot 10^{-4}$ cm^2 s^{-1} exp(-60.5 ± 9.2 kJ mol^{-1}R^{-1}T^{-1}) was obtained for the Ag_2In IMC. The observations were discussed in terms of the interplay of thermodynamic and kinetic constraints.

4.1 Introduction

The kinetics of intermetallic compound (IMC) formation are commonly studied at elevated temperatures in order that sufficiently large diffusion coefficients occur. Yet, investigation of IMC formation especially at low or ambient temperatures is of great impor-

tance with a view to technical applications. During manufacturing or usage of technical devices two metals experience intimate contact and interdiffusion and IMC formation occurring already at low temperatures between the two constituents could negatively alter the properties of the devices (see below for Ag–In alloys) [145, 146].

The Ag–In system is ideally suited to investigate interdiffusion and IMC formation at low temperatures: at RT IMC formation is readily observed using X-ray diffraction (XRD) [2, 23] and the interdiffusion coefficients of the system are large [23]. Group 11 metals (as Ag) are known to diffuse in metals of group 13 (as In) and group 14 (as Sn and Pb) via an interstitial mechanism [71], invoking a large mobility of Ag in these metals already at low temperatures. The large amount of grain boundaries in polycrystalline thin film couples, compared to bulk materials, further enhances interdiffusion and IMC formation, as these grain boundaries enhance the transport of especially substitutionally-diffusing metals [13] as holds for In, Sn and Pb in the Ag–In, Ag–Sn and Ag–Pb systems.

At least 3 IMCs occur in the Ag–In system at RT [73, 63]. The nominal compositions of these IMCs correspond to Ag_3In, Ag_2In[1] and $AgIn_2$. All three IMCs have a relatively small homogeneity range of about 1-2 at.% at RT [73] and can be conceived as so-called Hume-Rothery electron compounds [47]. In Ref. [38] it was suggested, based on superstructure reflections observed in XRD patterns, that an additional IMC α', with a composition corresponding to approximately Ag_3In, exists at RT. In has a relatively large solubility in Ag, about 20 at.% at RT, whereas Ag has practically no solubility in In [73].

Due to the low melting points of Ag–In alloys (the Ag–In system exhibits a low melting eutectic at the In-rich side of the phase diagram), Ag–In based solders can be used to replace the classical Pb-Sn based solders [37], the application of which in electrical components has been prohibited by the European directive ROHS (Restriction of Hazardous Substances Directive) [29]. Furthermore, In is frequently added to Ag-Sn based Pb-free solders to further improve the solder properties by lowering its melting temperature [35] and improving its wetting behavior [36]. Development of IMCs upon aging of solders at RT and at moderate operational temperatures can greatly deteriorate the electrical and mechanical properties of the solder joints [39, 40, 41, 42]. It was also shown that IMC formation strongly affects the bond strength of Ag-In joints [43, 44]. Consequently, fundamental knowledge of the kinetics of Ag–In IMC formation is of utmost importance in order to predict and optimize their long-term stability.

The kinetics of IMC formation in Ag–In systems has only scarcely been investigated until now. So far only diffusion-controlled growth of the IMCs has been observed. Available results suffer from simplifications in modeling, as that the presence of concentration

[1]Note that the ideal stoichiometric composition of the structure type of Ag_2In corresponds to a composition of Ag_9In_4 [66].

gradients was not taken into account for the determination of the diffusion coefficients [2, 27, 28]. In other cases, inadequate models were used for the determination of volume and grain boundary diffusion coefficients [25]. The rate controlling mechanisms (grain boundary or volume diffusion) are not properly discussed [25] and it is left unclear which type of diffusion coefficient was determined [25].

Against this background the present study provides a systematic analysis of the kinetics of IMC formation in Ag–In bilayer specimens. To this end, Ag–In thin film bilayer specimens were prepared by thermal evaporation. The sequence of the IMCs formed as well as the rate of their growth were investigated at RT and elevated temperatures using state-of-the-art time-resolved XRD. It has been found that the IMCs present in the as-deposited state depend on the stacking sequence of the Ag and In sublayers. The same observation has already been made for the Ag–Sn system [147]. In the present case only results from bilayers with In on top of Ag are discussed, where cases of simultaneous, mixed interface-diffusion-controlled growth and pure diffusion-controlled growth could be identified. Interdiffusion coefficients in the Ag–In system were derived on the basis of the values for the growth constants of the Ag_2In IMC at various temperatures.

4.2 Experimental Procedures

4.2.1 Specimen preparation

The Ag and In sublayers of the Ag-In bilayers were prepared by thermal evaporation using a Nano 36 (Lesker, Pittsburgh, USA) machine. The materials used were Ag (Lesker, purity 99.99 wt.%) and In (Heraeus, purity 99.9999 wt.%). Mo dimple boats were used as evaporation sources for both metals. The individual sublayers were deposited subsequently without breaking the vacuum. Single crystalline Si (100) wafers, covered with a thin 50 nm amorphous SiO_2 layer, were used as substrates. The substrates were ultrasonically cleaned for 20 min in acetone, followed by 20 min in isopropanol. Afterwards, the substrates were placed in a solution of 1 part of 32 wt.% H_2O_2 and 2 parts of 96 wt.% H_2SO_4 [107]. The solution was heated until the boiling point was reached, and kept at this temperature for about 20 min. Afterwards, the substrates were allowed to cool to RT, rinsed with demineralized water and dried in a flow of nitrogen gas. As last step of the cleaning procedure, the substrates were subjected to an oxygen plasma for 10 minutes. Next, the substrates were fixed on a rotatable substrate holder and placed at a distance of about 35 cm from the evaporation sources. Rotation speed of the substrate holder was 30 rpm. The Ag and In depositions were carried out at RT at pressures between 0.6×10^{-5} Pa and 2.6×10^{-3} Pa.

Thicknesses and deposition rates of the individual sublayers were monitored using a quartz crystal balance from Lesker. The balance was calibrated using a Dektak 8 profilometer (Veeco), which was also used for the roughness measurements. 500 nm of In were deposited on top of 500 nm of Ag. The Ag sublayers were deposited at 8 Å/s and the In sublayers were deposited at 44 Å/s.

If the In layers were deposited on top of Ag with smaller deposition rates, the roughness increased considerably ($R_a = 75 \pm 2$ nm at 15 Å/s), as compared to In single layers ($R_a = 13 \pm 1$ nm at 15 Å/s). Therefore, relatively thick (500 nm) In sublayers were deposited with high deposition rates in order to obtain smooth and dense In top layers. The roughnesses of the Ag and In sublayers in the bilayer specimens were $R_a = 3 \pm 1$ nm and $R_a = 21 \pm 1$ nm, respectively.

4.2.2 X-ray Diffractometry (XRD)

Phase evolution with time and temperature was investigated with a Bruker TXS D8 Discover diffractometer using Cu-K_α radiation from a rotating anode X-ray tube. The tube was operated at 50 kV and 20 mA. A Xenocs Fox 2D collimating multilayer X-ray mirror was placed in the incident beam path in order to obtain a monochromatic parallel beam. The radiation emerged from a (100 x 100) µm spot under a take off angle of 6 °. A VÅNTEC-500 2D detector (Bruker) was used for fast data recording [148]. The acquisition time of one frame was 120 s in case of the RT measurements and 60 s in case of the measurements at elevated temperatures. The acquisition time at elevated temperatures was reduced to maintain sufficient time resolution at the cost of some counting statistical accuracy, recognizing that IMC formation at this temperatures proceeds rapidly. The illuminated area on the specimen surface was restricted by a cylindrical collimator with a diameter of 1.5 mm. The intensities recorded by the 2D detector were converted to conventional XRD diffractograms by integrating over a wide range χ of the Eulerian cradle from 73.8° to 106.6° in order to reduce possible texture effects [148].

Aging of the bilayers was investigated at RT as well as at elevated temperatures. A BTS-Solid heating stage (MRI Physikalische Geräte GmbH, Karlsruhe, Germany) mounted on the diffractometer, was used for the temperature-resolved measurements at elevated temperatures. The heating stage is equipped with a X-ray transparent Be-dome that can be evacuated using a turbomolecular pump. The pressure inside the Be-dome during the measurements was approximately 10^{-3} Pa. The Ag–In bilayers were mounted on the heating stage directly after deposition of the sublayers. The temperature-resolved measurements were carried out at 50 °C, 60 °C and 70 °C. The temperature of the heat-

ing stage was controlled by a K-type thermocouple and the temperatures were stable to ±1°C.

The first XRD patterns, recorded at elevated temperatures, shown in Section 4.3, were recorded as soon as the temperature of the heating stage had reached the desired value; generally less than 5 min were necessary for the heating procedure.

Note that for the measurements at RT, $t = 0$ refers to the point of time when the first XRD was recorded (i.e. about 17 min after the start of the In deposition). For the measurements at elevated temperatures, $t = 0$ refers to the point of time when the heating stage reached the desired temperature and the first XRD pattern was recorded (i.e. about 17 min after the start of the In deposition, plus the time necessary for the heating procedure).

All XRD patterns were fitted using the TOPAS 4.2 software (Bruker, Karlsruhe, Germany) to obtain integrated intensities of the individual reflections. All peaks were fitted with pseudo-Voigt functions. The background was modeled using Chebychev polynomials of the tenth order. Goodness-of-fit (GOF) factors close to 1 were usually obtained for all fits.

Residual stresses in the Ag sublayer were recorded as a function of time at RT. Stress measurements of the In sublayer were not feasible due to the fast consumption of the In sublayer upon IMC formation and because of its strong texture. The stress measurements were performed with a Philips (PANalytical) MRD Pro diffractometer. The diffractometer operates in parallel beam geometry by means of a polycapillary X-ray collimator in the incident beam, using Co K_α radiation from a conventional X-ray tube operating at 40 kV and 40 mA. The beam passes through a graphite monochromator in the diffracted beam path. The spot size of the beam is approximately (4 x 4) mm. The diffracted intensity was recorded with a proportional counter.

The Ag 311 peak was found to be suitable for stress measurements. The corresponding X-ray elastic constants (XECs) were calculated using the Neerfeld-Hill approach (see i.e. Ref [149]), using values for the single-crystal elastic constants, as presented in Ref. [7]. For the calculation of the stress, the $sin^2\psi$ method was used adopting a (proven to be) rotationally-symmetric planar stress state and a macroscopically isotropic elastic specimen [149].

In order to reveal the stacking sequence of the IMC layers grown upon aging/annealing, XRD patterns were recorded in grazing incidence at angles varying from 0.2° to 15°. The measurements were performed using a Philips (PANalytical) MRD Pro diffractometer with the same specifications as the MRD diffractometer used for stress measurement but applying Cu K_α radiation from a conventional X-ray tube, operating at 40 kV and 40 mA.

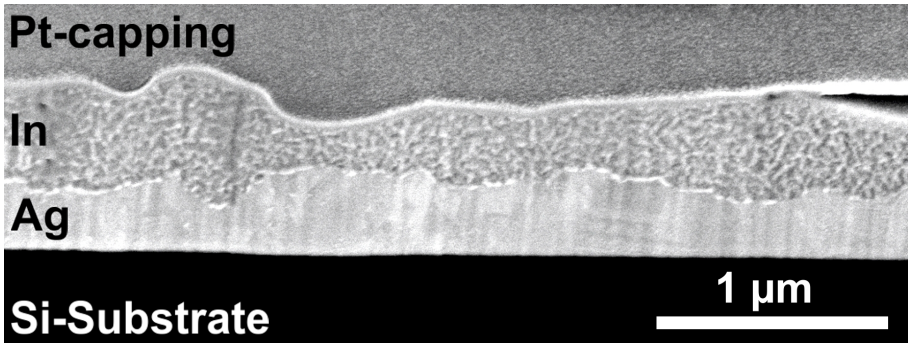

Fig. 4.1: SEM image of the Ga ion-beam prepared cross-section of an Ag–In bilayer sample. The SEM image was taken after about 1 h after preparation of the sample. The scale bar corresponds to distances perpendicular to the surface (see text for details).

4.2.3 Dual-Beam Microscopy

Cross-sections of the bilayers were prepared with the focused Ga ion beam (FIB mode) of a FEI Nova Nanolab 600 Dual-Beam instrument. In order to protect the microstructure of the bilayers during the milling procedure, a Pt capping layer was deposited on top of the bilayers with the Ga ion beam prior to the milling process. Microstructural images of the cross-sections were recorded with the electron beam of the instrument (SEM mode) operating at 5 kV and using a detector for secondary electrons (SE). To record the SEM images the sample was tilted to 52°.

4.3 Results

4.3.1 Microstructure and Phase Constitution

The temperature-resolved reactive interdiffusion measurements were limited to a maximum temperature of 70 °C, as XRD patterns recorded at higher temperatures (i.e. 90 °C) showed that the In layer had already reacted completely during the heating up of the specimen. Investigation of "Ag on top of In" and "In on top of Ag" type bilayers showed that for "In on top of Ag" type bilayers only the $AgIn_2$ IMC was present in the as-deposited state, whereas for the "Ag on top of In" type bilayers both $AgIn_2$ and Ag_2In were present in the as-deposited state. A similar observation was also made and explained for the case of Ag–Sn bilayers [147]. Therefore "In on top of Ag" type bilayers were chosen for the evaluation of the kinetics of IMC formation, as the presence of only one IMC in the as-deposited state allows a more straightforward analysis of the kinetics of IMC formation (cf. Section 4.3.2). Moreover, this sublayer sequence also allows direct comparison with previous studies, all of which pertain to "In on top of Ag" bilayer systems.

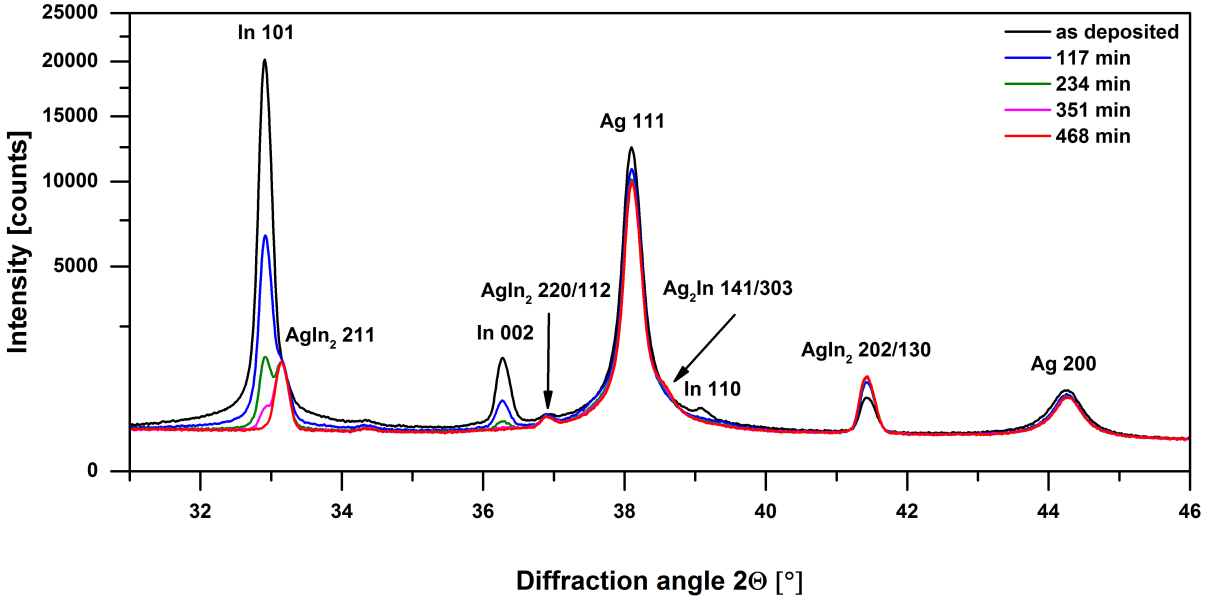

(a)

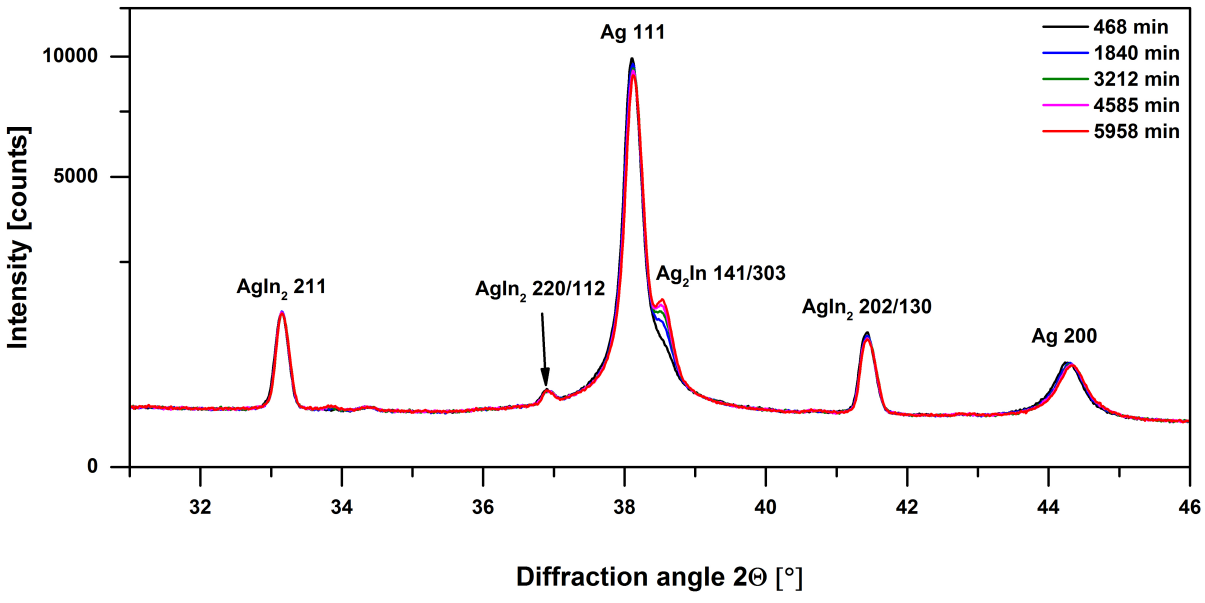

(b)

Fig. 4.2: XRD patterns recorded during RT aging. (a) As long as an In layer is present, the Ag layer reacts with the In layer to form $AgIn_2$. (b) After the In layer has completely reacted, the formed $AgIn_2$ layer reacts with the remaining Ag to form Ag_2In.

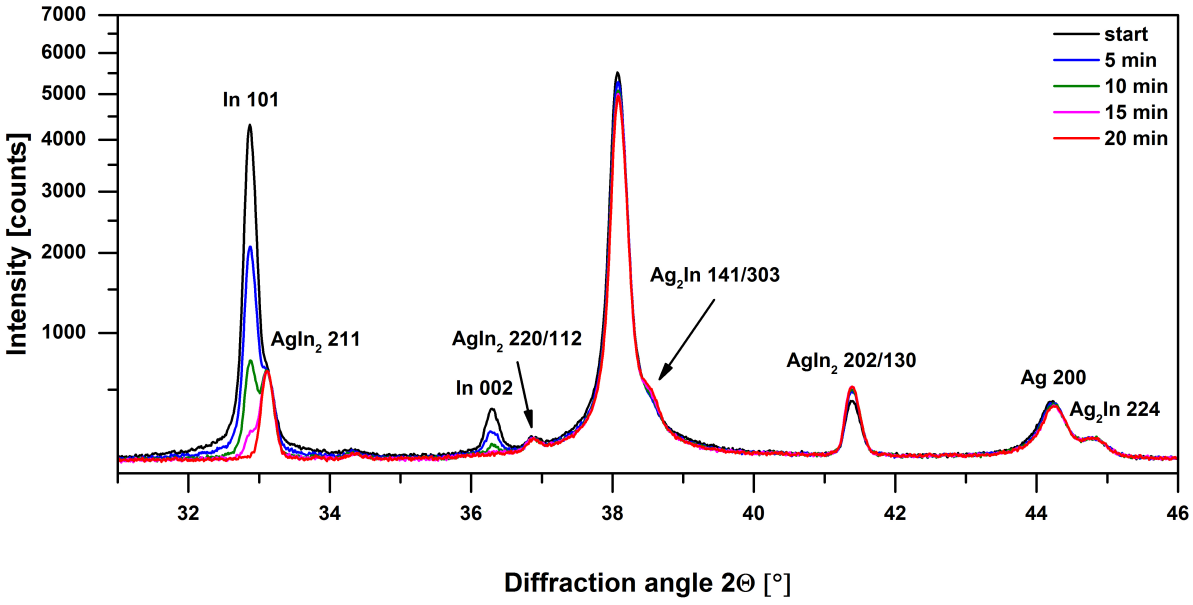

(a)

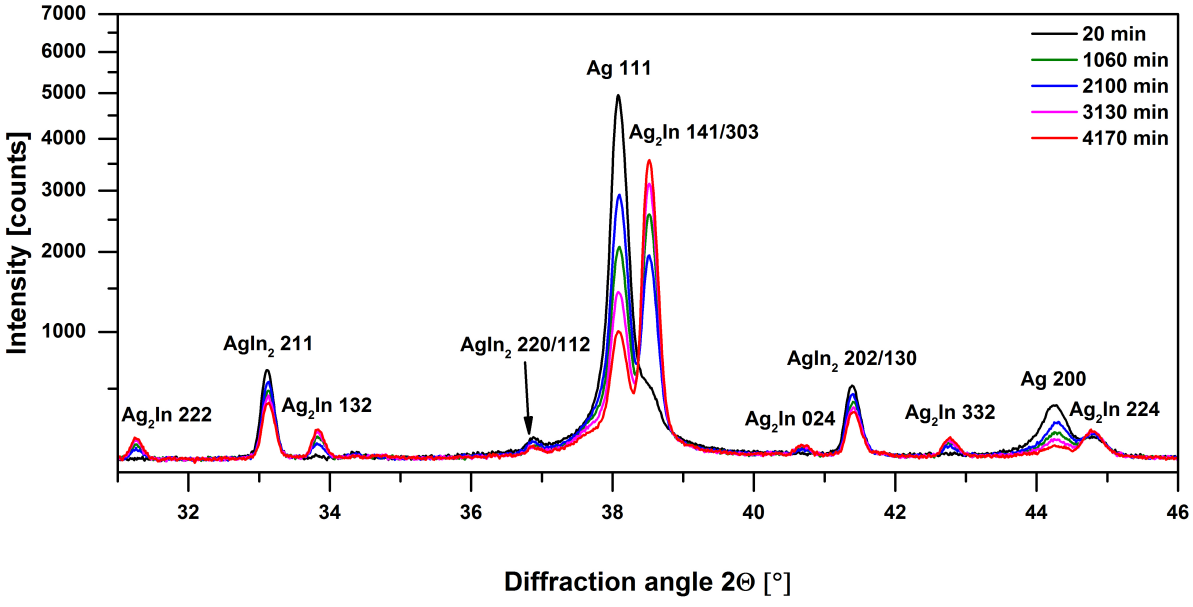

(b)

Fig. 4.3: XRD patterns recorded during aging at 70 °C. The same sequence of IMC formation, as observed at RT (see Fig. 4.2), can be seen. (a) XRD patterns recorded while (a part of) the In layer is present, (b) XRD patterns recorded after the In layer has reacted completely.

The bilayers consist of dense Ag and In sublayers without pores, with a relatively smooth interface and surface and thus are well suited to investigate IMC formation and interdiffusion for a one-dimensional (diffusion) geometry, see Fig. 4.1. The averaged thickness as measured from the cross-section of the bilayer corresponds well with the nominal total thickness of 1000 nm (note the scale bar in Fig. 4.1 only pertains to distances in the plane of the cross-section perpendicular to the specimen surface due to the tilt of the specimen stage). The individual thicknesses of the sublayers are not exactly equal, as a consequence of IMC formation already proceeding at this stage (1 h at RT after bilayer production; see below). Locations can be identified in the In layer (see Fig. 4.1), where the initial thickness of the In layer is smaller than that of the remaining, dominating part of the In layer, which cannot be avoided in the deposition process (cf. Section 4.2.1). However, only a very small amount of trenches is present in the In layers, therefore, these trenches do not significantly influence interdiffusion and IMC formation in the bilayer specimens.

Reflections of the $AgIn_2$ IMC are present in the XRD patterns, recorded in the as-deposited state for all specimens, together with reflections of In and Ag. The XRD patterns also show that the Ag sublayer of the Ag–In bilayers is weakly {111} fibre-textured, while the In layer is strongly {101} fibre-textured. Selected XRD patterns recorded during RT aging and aging at 70 °C, are shown in Figs. 4.2 and 4.3, respectively. The XRD patterns in Figs. 4.2a and 4.3a (beginning stages) show the presence of In, whereas the XRD patterns shown in Figs. 4.2b and 4.3b (later stages) indicate that all In has reacted. In Figs. 4.2b and 4.3b, reflections from the Ag_2In IMC occur in addition to those from $AgIn_2$[2]. Since more Ag_2In is formed at higher temperatures some of the Ag_2In reflections of lower intensity, which are visible in Fig. 4.3b, cannot be observed in Fig. 4.2b. A 2-dimensional representation of the XRD patterns as a function of time is shown in Figs. 4.4 to 4.7, for all aging temperatures. The XRD patterns show an initially fast decrease of the intensity of the In reflections and a fast increase of the intensities of the $AgIn_2$ IMC. Upon continued aging, the Ag_2In IMC starts to form. This sequence of IMC formation is observed at all temperatures.

4.3.2 Kinetics of IMC Formation

Integral intensities of specific reflections of the Ag, In, $AgIn_2$ and Ag_2In phases were determined to track the course of the phase transformations: For the Ag and In phases, the integrated intensities of the Ag 111 and In 101 reflections, respectively; for the $AgIn_2$ IMC the sum of the integrated intensities of the 202 and 130 reflections and for the Ag_2In

[2] A high-temperature modification of the $AgIn_2$ IMC, as proposed in Ref. [23], could not be observed in the XRD patterns.

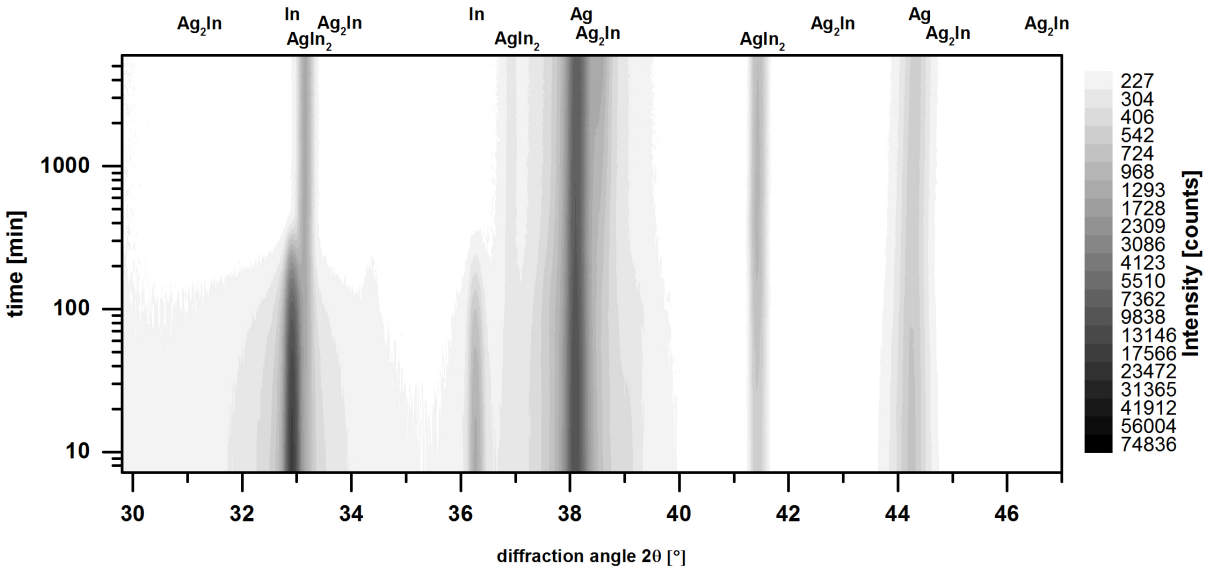

Fig. 4.4: 2-dimensional representation of the XRD patterns recorded as a function of time at RT.

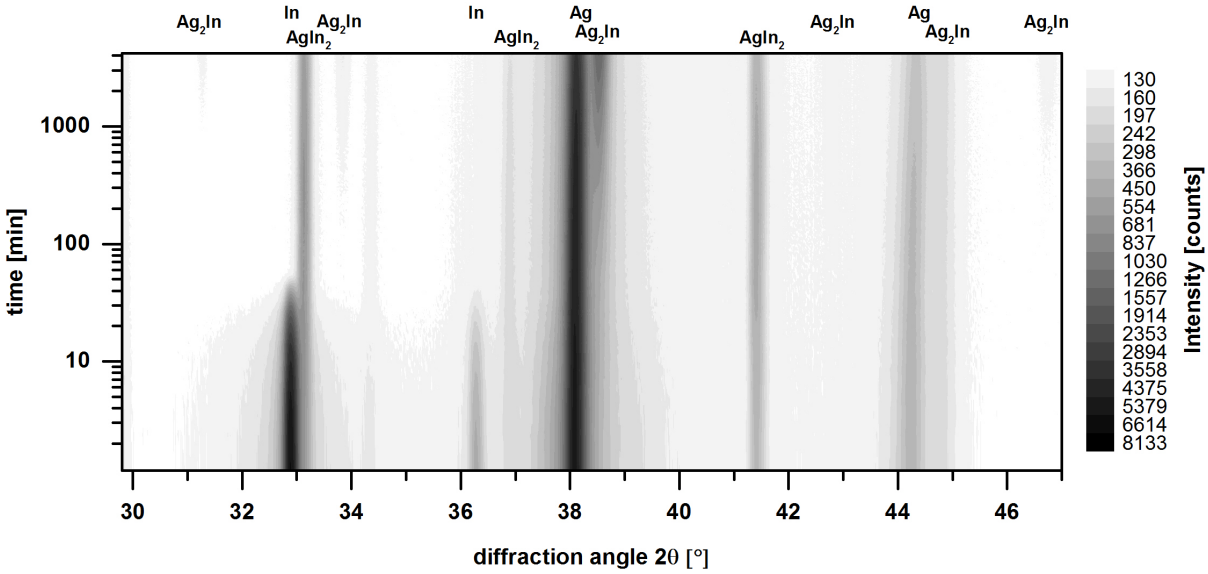

Fig. 4.5: 2-dimensional representation of the XRD patterns recorded as a function of time at 50 °C.

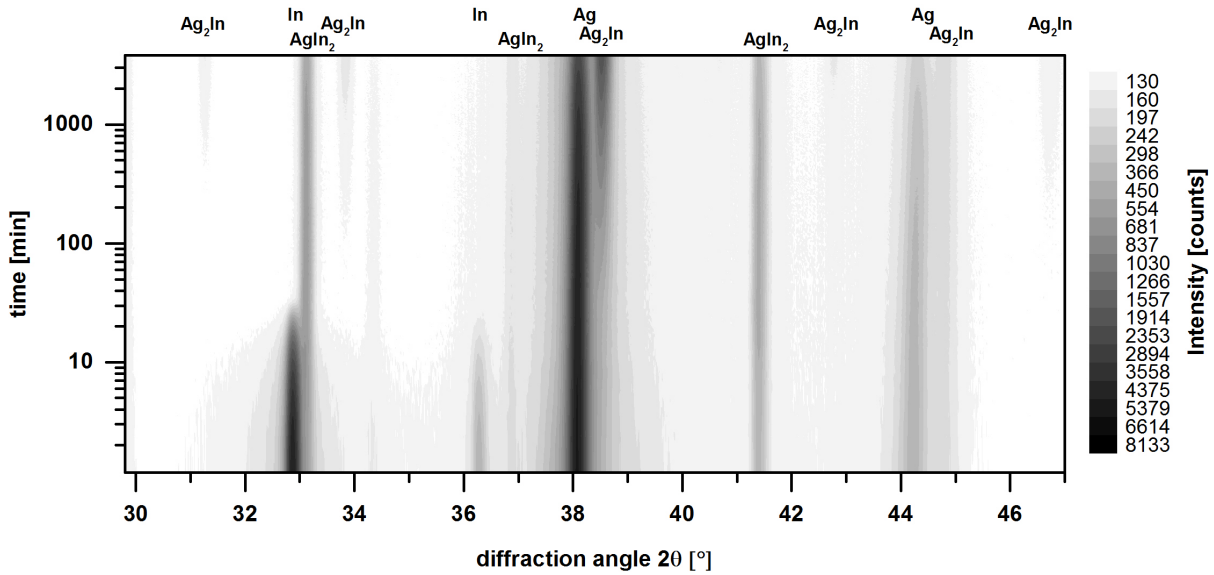

Fig. 4.6: 2-dimensional representation of the XRD patterns recorded as a function of time at 60 °C.

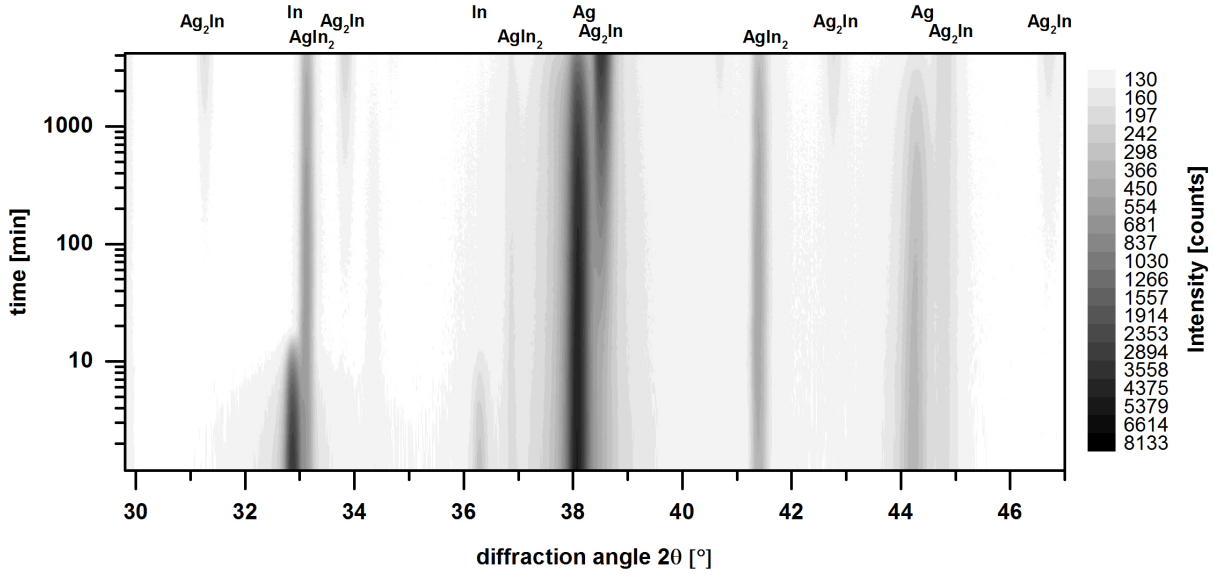

Fig. 4.7: 2-dimensional representation of the XRD patterns recorded as a function of time at 70 °C.

IMC the sum of the integrated intensities of the 141 and 303 reflections. The results are shown in Figs. 4.8, 4.9, 4.10 and 4.11 as a function of aging time at RT, 50 °C, 60 °C and at 70 °C, respectively.

Two distinct regimes of IMC formation can be observed. In the first regime the In phase is present. The second regime starts once all In has reacted. In the first regime the In layer reacts with the Ag layer to form the $AgIn_2$ IMC. This reaction proceeds very fast, the In reflections disappear approximately after about 370 min, 55 min, 30 min and 20 min at RT, 50 °C, 60 °C and at 70 °C, respectively. Neither interface-controlled (linear) growth, nor diffusion-controlled (parabolic) growth alone can well describe the growth of $AgIn_2$ in the first regime. A mixed growth mode, simultaneously controlled by both, the reaction of Ag and In at the interfaces of the IMC with (the remaining parts of) the original sublayers, as well as the diffusional processes in $AgIn_2$, provides an adequate description of the growth of $AgIn_2$ in the first regime. A fit of such a mixed growth mode, based on the equations for mixed IMC layer growth in Ref. [76], to the integrated intensities of $AgIn_2$ in the first regime is presented in Fig. 4.12.

In the second regime, the $AgIn_2$ IMC starts to react with the remaining part of the Ag sublayer to form Ag_2In. At RT a transition from a faster to a slower growth mode can be observed for the Ag_2In IMC (see Fig. 4.8d). At the elevated temperatures only the second, slow, growth mode is observed. The growth of Ag_2In is clearly diffusion-controlled (parabolic growth) at the elevated temperatures and at least in the second growth regime at RT (after about 1000 min), as indicated by the straight lines in Figs. 4.8d, 4.9d, 4.10d and 4.11d (plots of squared intensities vs. annealing/aging time). The non-linearity observed in the decrease of the integrated intensity of the Ag phase at 60 °C and 70 °C in the second regime, could be caused by a slight texture change of Ag, as suggested by the change of the ratio of the Ag 111 and 200 intensities. At higher temperatures a small increase of integrated intensity is observed on the course of overall about linear decrease of the squared integrated intensity of the $AgIn_2$ phase (see Figs. 4.9c, 4.10c and 4.11c). The origin of this increase cannot be identified at the moment, but is possibly again a texture effect as it is not visible in the integrated intensities of the remaining phases. Note that at the elevated temperatures, a very small amount of Ag_2In is already present in the first regime (see Figs. 4.3a, 4.5, 4.6, 4.7 and insets in Figs. 4.9d, 4.10d, 4.11d).

In order to verify the stacking sequence of the IMCs, XRD patterns were measured in grazing incidence geometry (c.f. Section 4.2.2). The measurements were performed on the specimen that had experienced the full aging time (100 h) at RT. The results are shown in Fig. 4.13. At the smallest incidence angles only reflections from $AgIn_2$ are present in the diffraction patterns, implying that $AgIn_2$ is on top of the thin film. Upon increasing

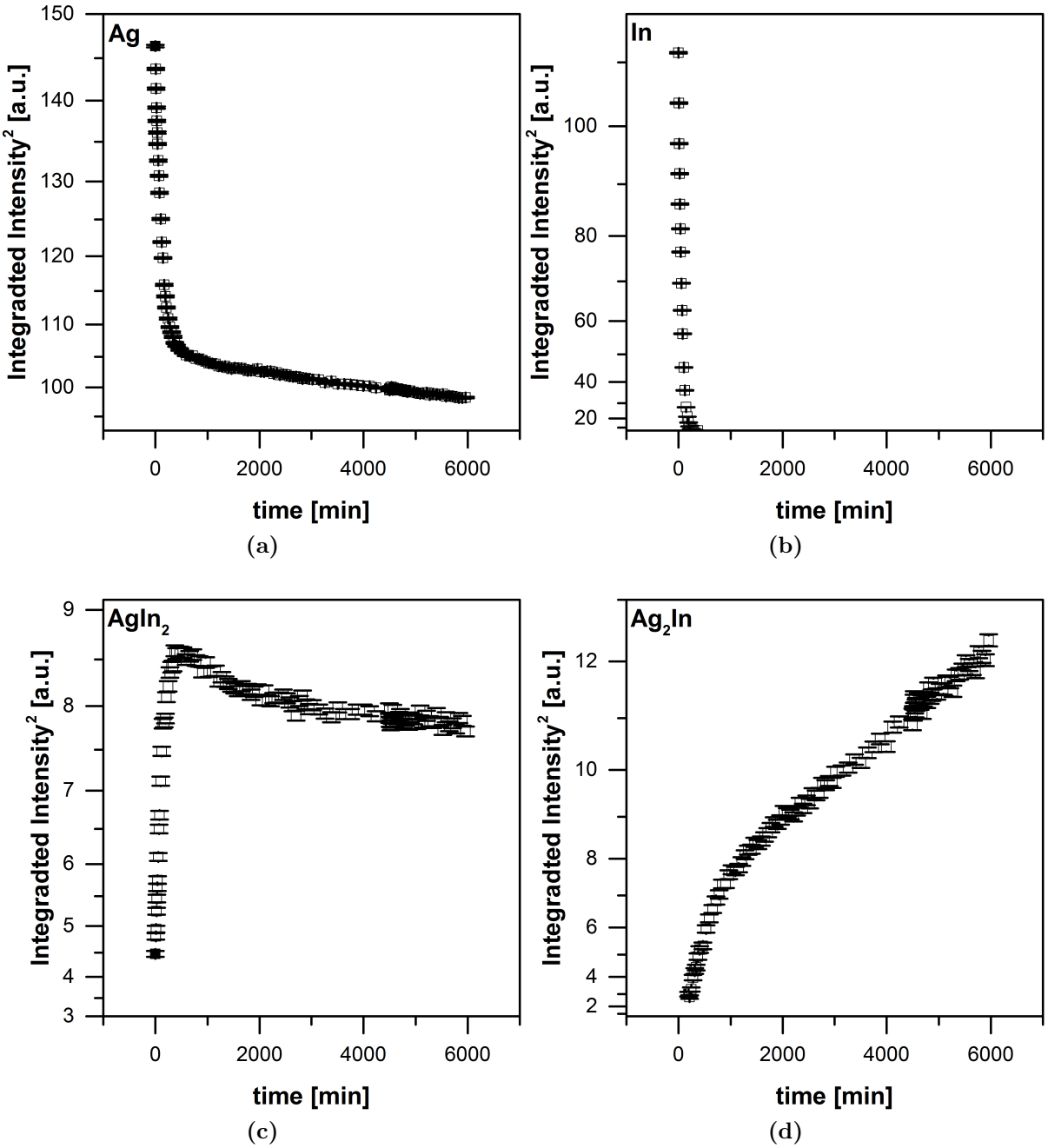

Fig. 4.8: Squared integrated intensities of the Ag, In, $AgIn_2$ and Ag_2In phases obtained from the XRD patterns recorded during RT aging. For the Ag and In phases the 111 and 101 reflections were used, respectively. For the $AgIn_2$ IMC, the sum of the 202 and 130 reflections was used, while for the Ag_2In IMC the sum of the 141 and 303 reflections was used. Two regimes can be distinguished, their occurrence is connected with the presence / absence of the In layer (see text).

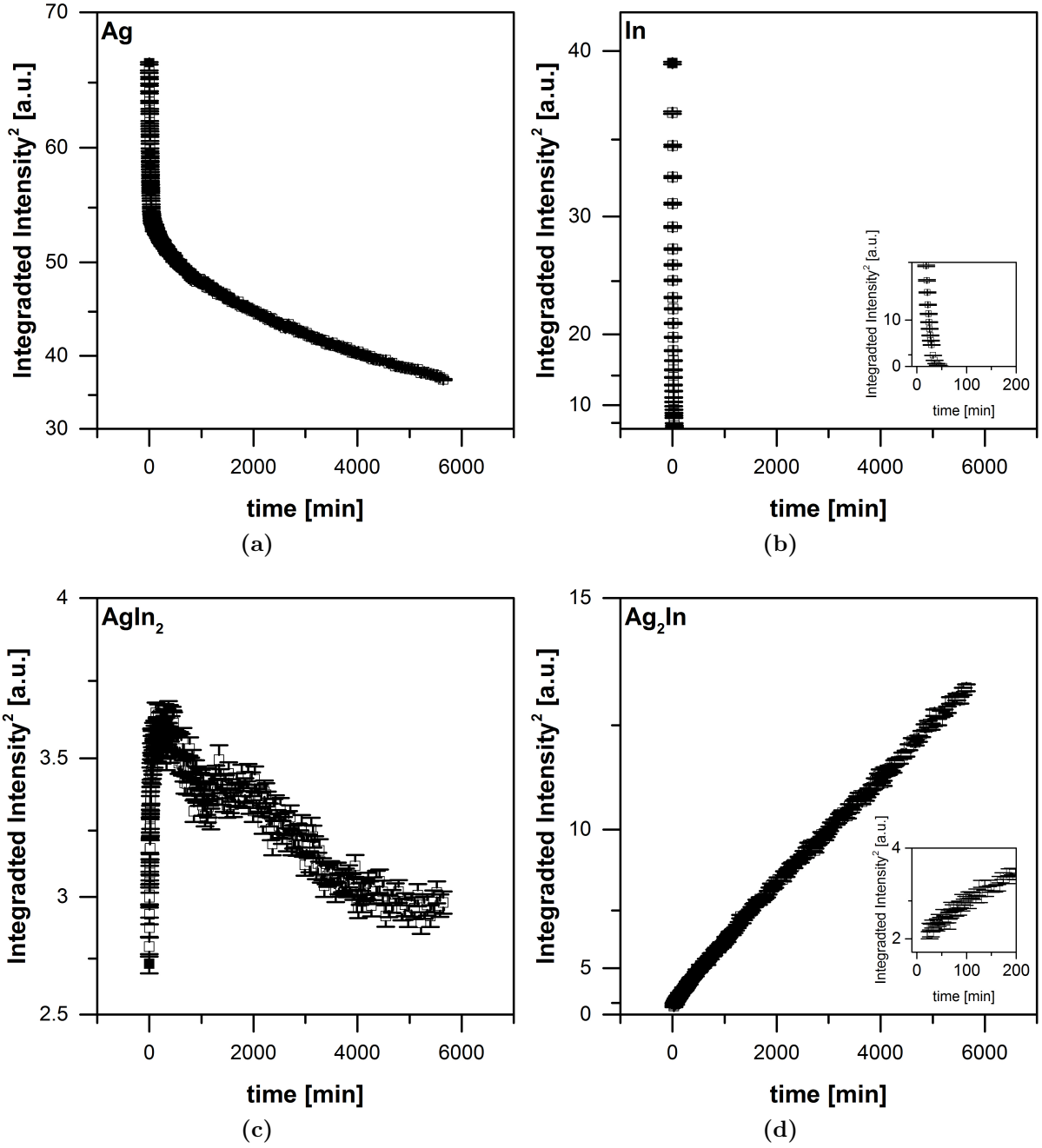

Fig. 4.9: Squared integrated intensities of the Ag, In, $AgIn_2$ and Ag_2In phases obtained from the XRD patterns (see caption of Fig. 4.8), recorded during aging at 50 °C. The same two regimes, as seen in Fig. 4.8, are present but the first regime is considerably shorter, as compared to the data obtained during RT aging (see insets in Figs (b) and (d)).

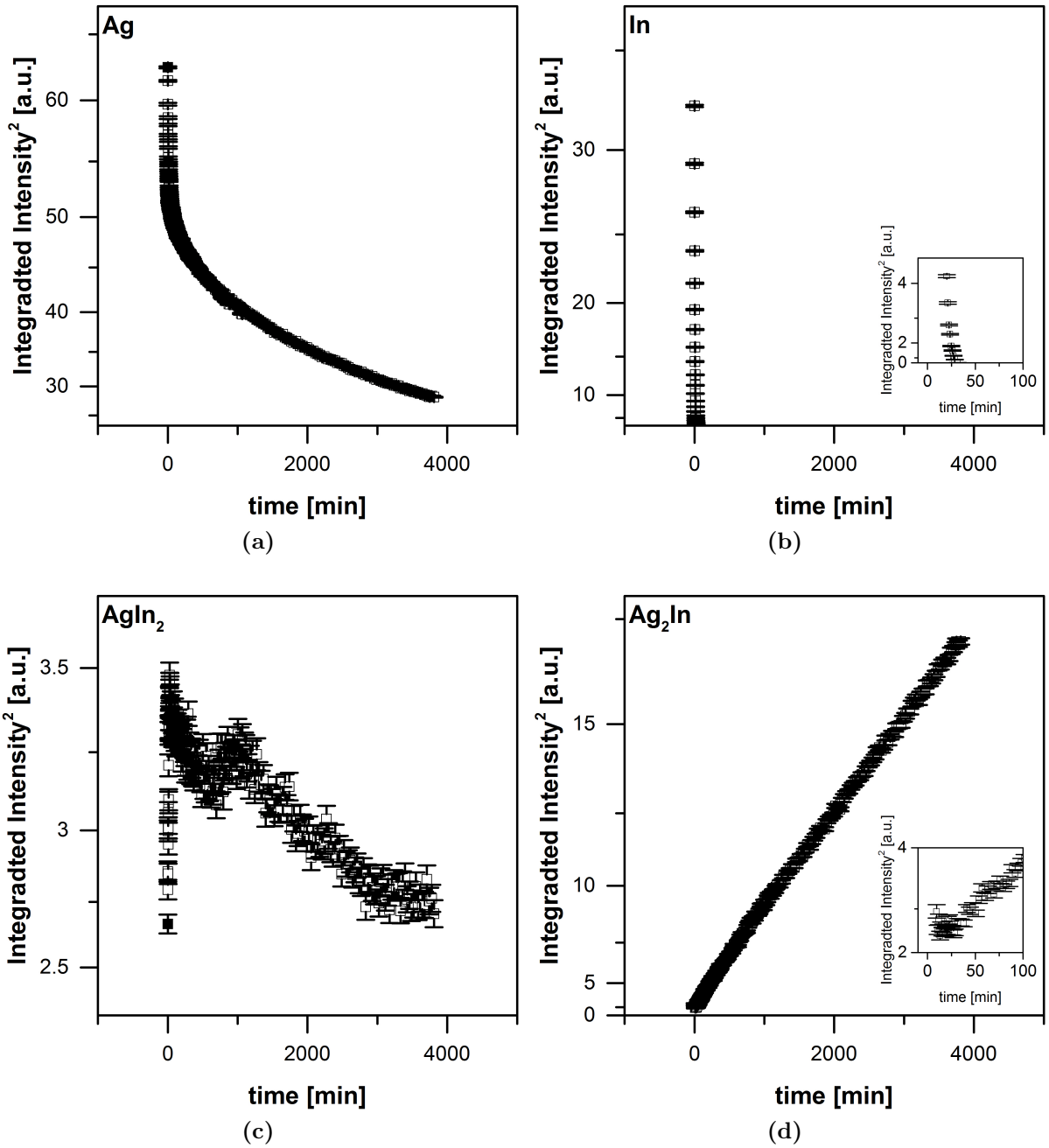

Fig. 4.10: Squared integrated intensities of the Ag, In, $AgIn_2$ and Ag_2In phases obtained from the XRD patterns (see caption of Fig. 4.8), recorded during aging at 60 °C. The same two regimes, as seen in Fig. 4.8, are present but the first regime is considerably shorter as compared to the data obtained during RT aging as well as aging at 50 °C (see insets in Figs (b) and (d)).

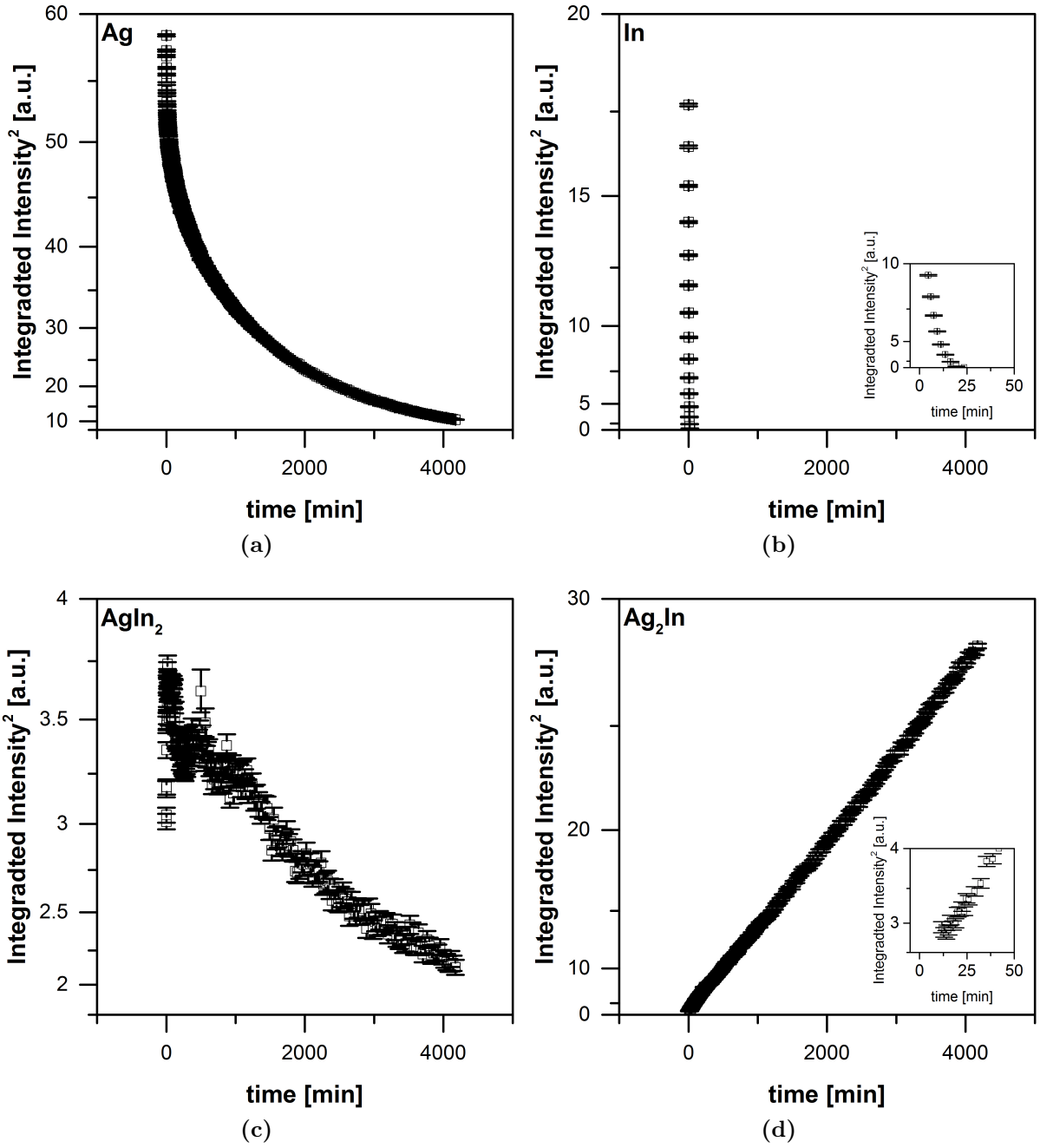

Fig. 4.11: Squared integrated intensities of the Ag, In, $AgIn_2$ and Ag_2In phases obtained from the XRD patterns (see caption of Fig. 4.8), recorded during aging at 70 °C. The first regime (cf. Figs. 4.8, 4.9 and 4.10) can no longer be observed.

the incidence angle first reflections from Ag_2In appear, followed by reflections from Ag. No In reflection can be detected, as the In layer had already reacted completely during RT aging. The successive occurrence of the mentioned diffraction peaks upon increasing the angle of incidence strongly suggests that in the second regime Ag_2In grows as a layer between $AgIn_2$ on top (at the surface) and Ag below (towards the substrate).

4.3.3 Reaction and Diffusion Constants

To obtain reaction constants of the formation of the IMCs, the thicknesses of the IMC layers have been calculated from the integrated intensities of the 111 Ag and 101 In reflections, since the two IMC layers could not clearly be distinguished in the SEM images. From the amounts of Ag and In that have reacted, the thicknesses of the $AgIn_2$ and Ag_2In IMC layers can be obtained as follows. The following reaction is considered (note that ideal stoichiometric compositions have been adopted for the IMCs, see also footnote in Section 4.1):

$$AAg + BIn \rightarrow X\mathrm{Ag_9In_4} + Y\mathrm{AgIn_2}, \tag{4.1}$$

where A and B are the number of Ag and In atoms per unit area of the surface of the specimen that have reacted to form X and Y formula units of Ag_9In_4 and $AgIn_2$, respectively, per unit area of the surface of the specimens. X an Y can then be calculated, using the law of mass conservation, according to:

$$X = \frac{2A - B}{14} \tag{4.2}$$

and

$$Y = \frac{9B - 4A}{14}. \tag{4.3}$$

Using the densities and molar volumes for Ag (10.5 g cm^{-3} and 107.868 g mol^{-1} [7]) and In (7.31 g cm^{-3} and 114.82 g mol^{-1} [7]) A and B can be calculated in turn from the thicknesses of the Ag and In layers that have reacted to form the IMCs.

Since no In is present at the end of the aging process, the total reacted thickness of the In layer at this point is 500 nm. Knowing the initial thickness of the Ag layer (500 nm), the amount (thickness) of the Ag layer that has reacted at the end of the aging process can be obtained from the relative decrease of the integrated intensity of the Ag 111 reflection. However, a small amount of $AgIn_2$ was already present in the as-deposited state (see Figs. 4.2 and 4.3). Therefore, the integrated intensity of the Ag peak in the as-deposited state does not correspond to 500 nm of Ag. The thickness of the Ag layer in the as-deposited state (i.e. about 17 min after the onset of the In deposition) can be assessed by backwards linearly extrapolating the integrated intensity of the Ag 111

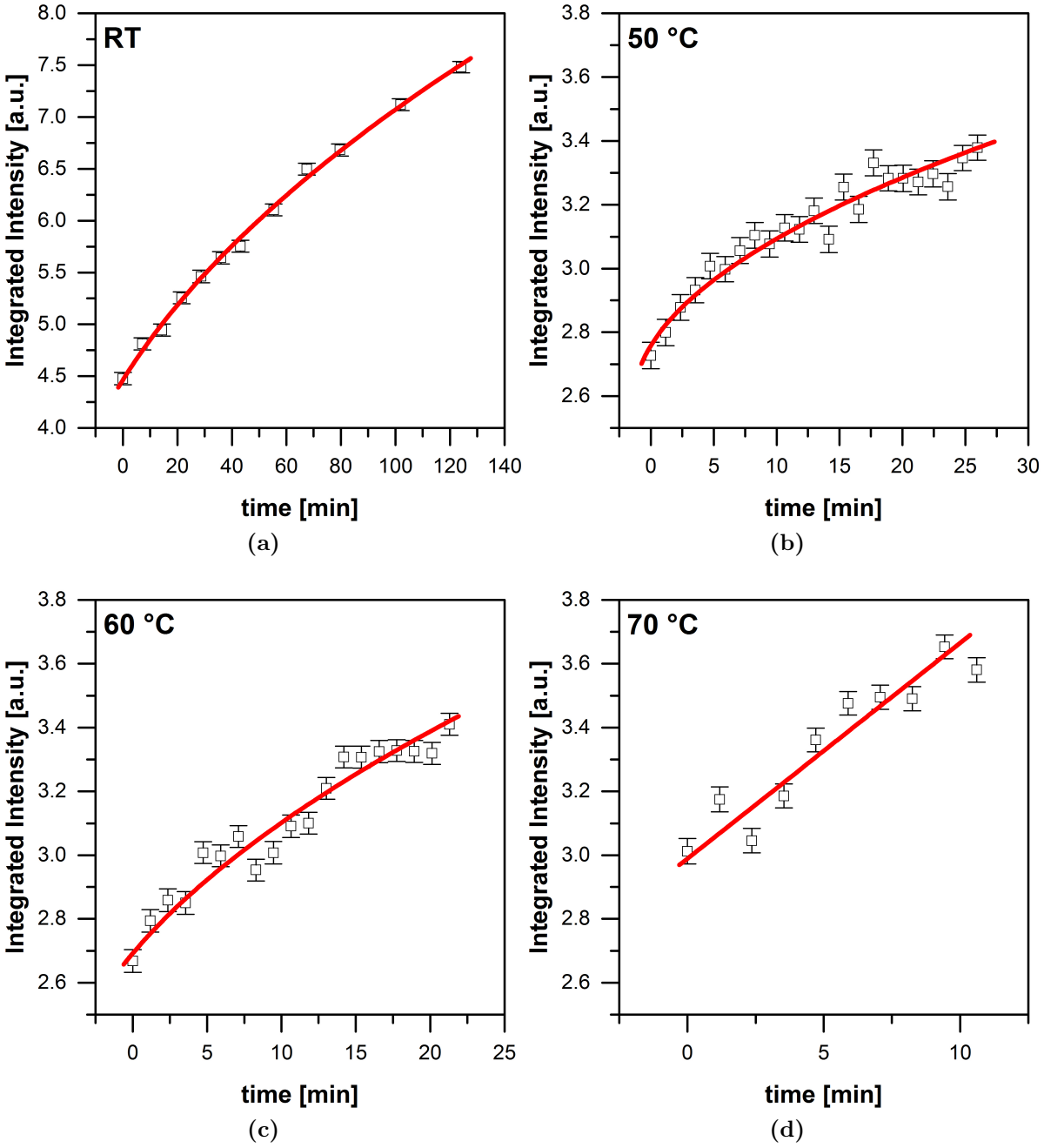

Fig. 4.12: Integrated intensities of the sum of the $AgIn_2$ 202 and 130 reflections in the first regime. The data can best be described by a mixed growth mode, containing contributions of interface- as well as diffusion-controlled growth. The red lines show the fit to the data based on the equations for a mixed growth mode as given in Ref. [76].

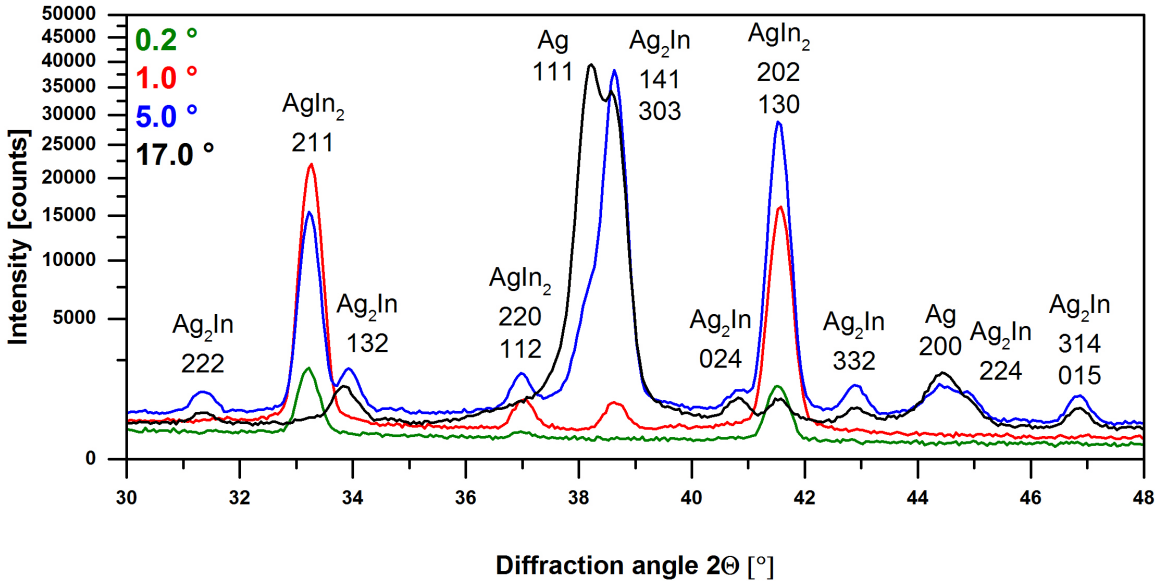

Fig. 4.13: XRD patterns recorded in grazing incidence geometry with incidence angles of 0.2°, 1.0°, 5.0° and 17.0°. The patterns have been recorded on the sample that has been aged for 100 h at RT. It follows that the top layer is $AgIn_2$ followed by Ag_2In and Ag.

peak to the onset of the In deposition (i.e. about 17 min before obtaining the first XRD pattern) where the Ag layer thickness *does equal 500 nm*. The thickness of the Ag layer in the as-deposited state (i.e. about 17 min after the onset of In deposition) then follows from the decrease of the integrated intensity between the extrapolated value (start of In deposition) and the value in the as-deposited state (after about 17 min). This is the initial estimate for the thickness of the Ag sublayer in the as-deposited state (see iterative procedure indicated immediately below).

The amounts of the IMCs formed per unit area of the surface of the specimen, expressed in the numbers of formula units X and Y, *at the end of the aging time* can now be calculated using Eqs. 4.2 and 4.3; only at this point of time the value of B is known: the In layer has reacted completely and hence B corresponds to 500 nm of In. Furthermore, the value for A at the end of the aging time follows from the relative decrease of the integrated intensity of the Ag 111 reflection at the end of the aging time. Subsequently, using the number of formula units of IMC per unit cell (4 in both cases) and the volume of the respective unit cells (0.97133 nm^3 for Ag_2In [66] and 0.2661 nm^3 for $AgIn_2$ [150]), the thicknesses of the IMC layers at the end of the aging time can be calculated straightforwardly. Now the thicknesses of the IMC layers, at any point of time, follows from the relative change of the integrated intensities of the reflections of the IMCs with respect to their integrated intensities at the end of the aging time.

A second estimate for the thickness of the Ag sublayer in the as-deposited (i.e. about 17 min after the onset of the In deposition) can now be obtained from the thickness of

the $AgIn_2$ IMC layer in the as deposited state (where no Ag_2In is present) as follows: The difference of the total number of Ag atoms (per unit area of the surface of the specimens), corresponding to an Ag layer of 500 nm thickness, and the number of Ag atoms (per unit area of the surface of the specimens) used for the formation of the $AgIn_2$ layer in the as-deposited state, corresponds to the number of Ag atoms (per unit area of the surface of the specimens) contained in the Ag layer in the as-deposited state and thus provides a new estimate for the Ag layer thickness in the as-deposited state. Using this new value for the Ag layer thickness in the as-deposited state, the thicknesses of the IMC layers at the end of the aging time, where A and B are obtained as described above, can again be calculated and thus the IMC layer thicknesses at any point of time are available (see above). This procedure is repeated until the value of the thickness of the Ag layer in the as-deposited state shows no further significant change upon repeating the procedure. As a final result it follows that 86 nm of the Ag layer had already reacted in the as-deposited state.

In case of the XRD patterns, recorded at elevated temperatures, the absorption of the X-rays due to the evacuated Be-dome has to be accounted for. To quantitatively asses and correct for this effect, a frame has been recorded in the as-deposited state before each heating-up procedure, where it is known that the Ag layer thickness is 414 nm (500 nm - 86 nm, see above). Hence the value of the integrated intensity of Ag 111 reflection in this frame corresponds to 414 nm of Ag. The Ag layer thickness as function of annealing time then follows from the relative decrease of the Ag 111 reflection during the aging procedure. The IMC layer thicknesses *at the end of the aging time* are again calculated as described above, thereby providing access to the values for the IMC layer thicknesses as a function of annealing time (see above).

The thicknesses of the $AgIn_2$ and the Ag_2In IMCs finally obtained with this procedure are shown as function of aging/annealing time of the various temperatures in Figs. 4.14a and 4.14b, respectively. The overall composition of the bilayer specimens corresponds to about 60 at.% Ag (obtained using the densities and molar masses of Ag and In [7]). According to the Ag-In phase diagram [73] at 1 atm, a composition of 60 at.% Ag corresponds to a 2 phase mixture of about 25 at.% $AgIn_2$ and 75 at.% Ag_2In. The obtained thicknesses for the $AgIn_2$ and Ag_2In layers at the end of the aging procedure are in good agreement with this prediction, recognizing that some unreacted Ag is left in the bilayer specimens, thereby lending support to the procedure applied to calculate product-layer thicknesses as function of aging/annealing time.

During the second (slower) stage of Ag_2In growth at RT and during the growth of Ag_2In at elevated temperatures, clearly a parabolic growth of Ag_2In persists (see plots of squared layer thickness vs. time in Fig. 4.15). This is compatible with diffusion-

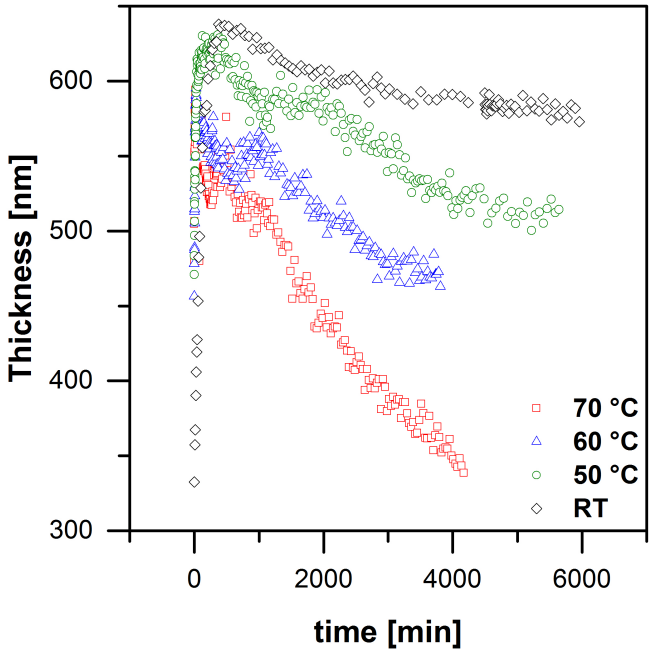

(a)

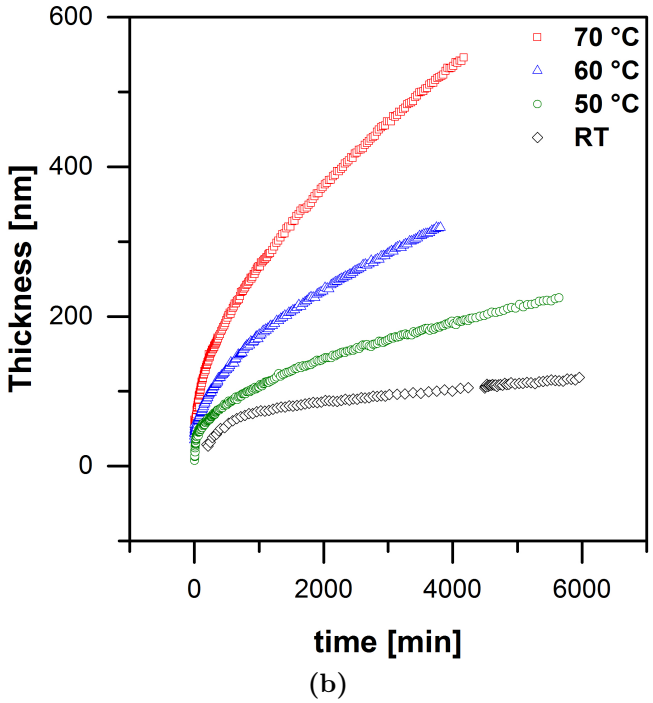

(b)

Fig. 4.14: Thicknesses of the $AgIn_2$ IMC (a) and the Ag_2In IMC (b) as function of time at various aging temperatures.

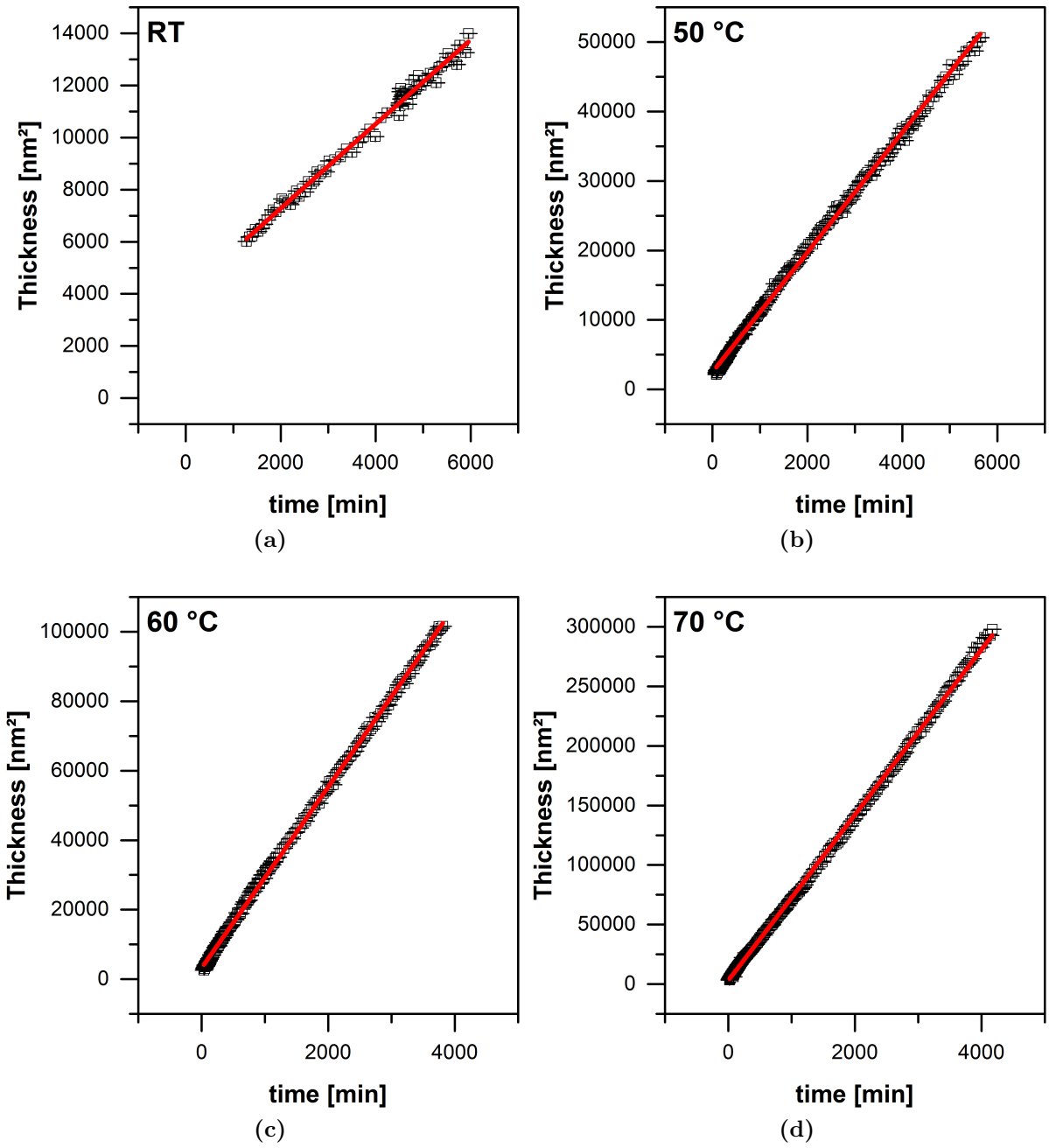

Fig. 4.15: Squared thicknesses of the Ag_2In IMC obtained during the continued aging/annealing in the second growth regime at various temperatures. Evidently, diffusion-controlled growth prevails. The slopes of the straight, red lines fitted to the data provide values for the parabolic growth constant k_{Diff}.

Table 4.1: Parabolic rate constants k_{Diff} and associated interdiffusion coefficients obtained for Ag_2In growth in the second kinetic regime, the corresponding activation energy Q^{Ag_2In} and the preexponential factor $D_0^{Ag_2In}$.

T [K]	RT	50 °C	60 °C	70 °C
k_{Diff} [nm min$^{-1/2}$]	0.6356	1.4682	2.5501	4.1728
D [10^{-14} cm^2 s^{-1}]	0.223 ± 0.002	1.190 ± 0.003	3.591 ± 0.006	9.616 ± 0.015
Q^{Ag_2In}		60.5 ± 9.2 kJ mol^{-1}		
$D_0^{Ag_2In}$		$1.1 \pm 3.9 \cdot 10^{-4}$ cm^2 s^{-1}		

controlled growth. In order to obtain the parabolic growth constants of the diffusion process:

$$k_{\mathrm{Diff}} = \frac{\Delta x^2}{2t}, \tag{4.4}$$

where Δx is the thickness of the IMC and t is the time, straight lines were fitted to the data in Fig. 4.15. From the parabolic rate constants an average interdiffusion coefficient for the Ag_2In IMC can be determined adopting a procedure as described in Ref. [84], based on the treatment of interdiffusion, as provided in Ref. [151], for binary systems exhibiting IMCs with narrow homogeneity ranges and planar interfaces. In the present case the grazing incidence XRD measurements (see Fig. 4.13 and the corresponding discussion) indicate that the bilayer specimens have a layered structure and the homogeneity ranges of the ordered Ag_2In and $AgIn_2$ IMCs [73] fulfill the assumption of a narrow homogeneity range. Further the treatment of Ref. [84] assumes that there is only a limited solubility in the terminal phases, which is justified for the present case, as In has practically no solubility for Ag and XRD stress measurements performed in this work show that no In is taken up by the Ag layer (see below). Then the average interdiffusion coefficient for the present stacking sequence $AgIn_2$ / Ag_2In / Ag can be determined according to (cf Eq. (5) in Ref. [84]):

$$\tilde{D}_{av}^{Ag_2In} = \frac{(c_{Ag_2In} - c_{AgIn_2})(c_{Ag} - c_{Ag_2In})}{(c_{Ag} - c_{AgIn_2})\Delta c_{Ag_2In}} k_{\mathrm{Diff}}, \tag{4.5}$$

where c_{Ag_2In}, c_{AgIn_2} and c_{Ag} are the average mole fractions of Ag in the Ag_2In (9/13) (see footnote in Section 4.1), $AgIn_2$ (1/3) and Ag (1) phases, respectively, and Δc_{Ag_2In} is the concentration difference over the cross-section of the Ag_2In IMC (about 1 at.% [65, 73]). As indicated by the strain-free lattice parameter of the Ag layer (see Section 4.3.4), no significant amount of In had dissolved in the Ag layer and hence $c_{Ag} = 1$.

The obtained parabolic growth constants, as well as the interdiffusion coefficients determined using Eq. 4.5, have been listed in Table 4.1 for the the different aging temperatures.

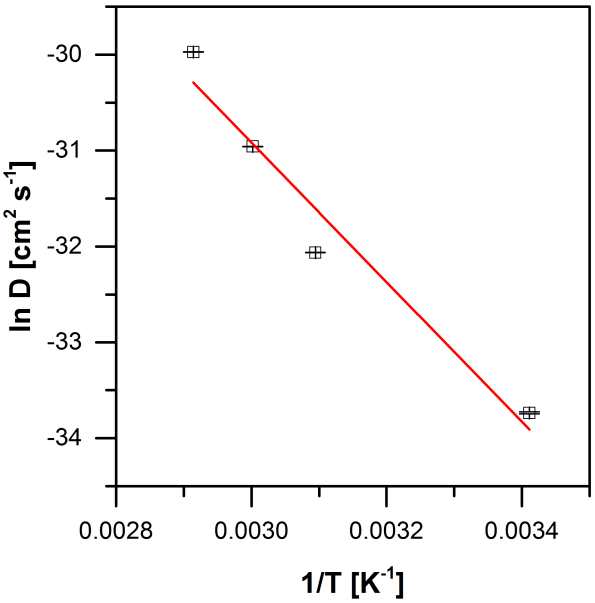

Fig. 4.16: Arrhenius type plot of the interdiffusion coefficients of the Ag_2In IMC.

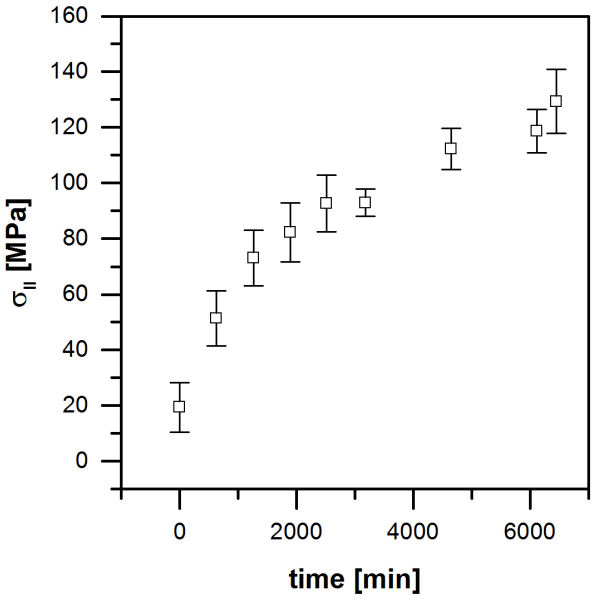

Fig. 4.17: Development of the residual stress parallel to the surface, σ_{II}, in the Ag layer as a function of RT aging time.

The diffusion coefficients are shown in Fig. 4.16 as a function of T^{-1}. The activation energy of the diffusion process , as determined from the of the slope of the straight line fitted to the data in Fig. 4.16, equals 60.5 ± 9.2 kJ mol^{-1}.

4.3.4 Stress Development in the Ag Layer

For the stress measurements the Ag 311 peaks were initially measured from ψ =0 ° to ψ =60 ° in 7.5 ° steps, where ψ is the angle between the surface normal of the specimen and the diffraction vector. The measurements were repeated at 3 different ϕ angles, where ϕ is the angle of rotation around the specimen-surface normal, each with an offset of 45 ° with respect to the previous measurement. No significant differences were observed between the results of the measurements at variable ϕ at constant ψ, implying that the plane state of stress is rotationally symmetric: $\sigma_{II} = \sigma_{11} = \sigma_{22}$. A straight line was fitted to the data in the plots of the Ag 311 lattice spacing vs. $sin^2\psi$ and the stress was determined using the $sin^2\psi$ method, as described in Section 4.2.2.

On the basis of the above results, it was decided to measure at only two ψ values; ψ =0 ° and ψ =60 ° for the time-resolved stress measurements upon aging/annealing, in order to decrease the measurement time. The stress development as a function of aging time at RT is shown in Fig. 4.17. In the as-deposited state a tensile stress of about 20 MPa is present. This stress can be well ascribed to elastic accommodation of the thermal mismatch of the Ag layer and the Si substrate, arising upon cooling from the deposition temperature to RT:

$$\sigma_T = \frac{E}{1-\nu}(\alpha_{Si} - \alpha_{Ag})\Delta T, \tag{4.6}$$

where E and ν are the Young's modulus and Poisson ratio of the Ag layer, α_{Ag} and α_{Si} are the thermal expansion coefficients of Ag and Si, respectively, ΔT is the temperature difference between RT and the deposition temperature, which is about -13 °C for the deposition of the Ag layer [147]. Eq. 4.6 yields a value of 27 MPa using the elastic constants and thermal expansion coefficients listed in Ref. [7].

During aging at RT, the tensile stress in the Ag layer increases. After about 1000 min of RT aging, this tensile stress increase slows down. This correlates with the change of growth mode of the Ag_2In IMC (see Fig. 4.8d and Section 4.3.2), which also occurs at about 1000 min at RT.

The value obtained for the stress-free lattice parameter of Ag, determined in the X-ray stress analysis by interpolation at the stress-free direction in the d_ψ-$sin^2\psi$ plot [149], does not change during aging at RT and amounts to 4.086 Å, which well agrees with the value of pure Ag ($a_0 = 4.086$ Å) [152] (see discussion below Eq. 4.5). This shows that no In is taken up by the Ag layer during the aging process.

4.4 Discussion

4.4.1 First Kinetic Regime

The first IMC that forms in the bilayer specimens is $AgIn_2$ (see Section 4.3.1). This can be ascribed to thermodynamic and/or kinetic constraints.

The enthalpies of formation at RT from the elements for the $AgIn_2$ and Ag_2In IMCs are -3.5 kJ mol^{-1} and -4.3 kJ mol^{-1} per mole atoms of IMC, respectively [79]. As both IMCs have an ordered structure, the contribution of the entropy of formation from the elements to the Gibbs energy of formation from the elements is very small and the enthalpies of formation can be identified with the Gibbs energies of formation from the elements [124].

Ag diffuses interstitially and thus very fast in In, whereas In diffuses substitutionally and thus relatively slow in Ag. Further, In has practically no solubility for Ag at RT, whereas about 20 at.% In can dissolve in principle in Ag at RT [73]. Hence, it is most likely that IMC formation initiates inside the In layer (see also Ref. [153]). Then, in order to compare the energies released upon formation of both IMCs, the Gibbs energy of formation of IMC *per Ag atom* of IMC has to be considered. It thus follows that in case of the $AgIn_2$ IMC -10.5 kJ per mole of Ag atoms is released, whereas in case of the Ag_2In -6.2 kJ per mole of Ag atoms is released. Hence *initial* formation of $AgIn_2$ inside the original In layer is preferred, as observed. Similar reasoning was also used to explain the results obtained upon IMC formation in the Ag-Sn system [147].

Additionally, it seems possible that nucleation of the $AgIn_2$ IMC is associated with a smaller nucleation barrier, as compared to nucleation of the Ag_2In IMC: (i) the volume per mole In is larger in case of the Ag_2In IMC [66] as compared to the $AgIn_2$ IMC [150], while both values are larger than the molar volume of the In layer [154]. It follows that the volume misfit upon IMC formation inside the In layer is larger in case of the Ag_2In IMC compared to the $AgIn_2$ IMC, favoring initial formation of $AgIn_2$ inside the original In layer; (ii) further Ag_2In has a much more complex crystal structure: the $AgIn_2$ IMC has an ordered tetragonal structure (space group $I4/mcm$, $CuAl_2$-type) with 12 atoms per unit cell occupying 2 different Wyckoff positions [150], whereas Ag_2In has an ordered cubic structure (space group $P\bar{4}3m$, Cu_9Al_4-type) with 52 atoms per unit cell occupying 8 different Wyckoff positions [66].

As the Ag_2In IMC readily forms in the second regime (see Section 4.3.2), its initial suppression in the first regime may have a *kinetic* origin as well. For binary diffusion couples [76] (see also the treatment presented in Ref. [147]) it could be shown, as a matter of principle, that as long as formation of a first IMC is interface-controlled, the formation of a second IMC can be suppressed. Only if the the formation of the first IMC

becomes diffusion-controlled and a critical thickness is surpassed, a second IMC can form. In accordance with Ref. [76], a model system is considered of two IMC layers possibly growing between the elemental layers. The concentrations of the elemental (terminal) layers are assumed to be constant during IMC growth. In the present case the model system is given by Ag|Ag_2In|$AgIn_2$|In. Three different cases of IMC growth can be distinguished [76], depending on the ratio r of the fluxes of the Ag atoms across the Ag_2In ($j^{Ag}_{Ag_2In}$) and $AgIn_2$ ($j^{Ag}_{AgIn_2}$) IMC layers:

$$r = \frac{j^{Ag}_{Ag_2In}}{j^{Ag}_{AgIn_2}}. \tag{4.7}$$

The three different growth regimes are separated by specific values, r_1 and r_2, for the flux ratio r:

$$r_1 = \frac{(1+\gamma)(\alpha-\beta)}{(1+\beta)(\alpha-\gamma)} \tag{4.8}$$

and

$$r_2 = \frac{(1+\gamma)(\beta-\delta)}{(1+\beta)(\gamma-\delta)}, \tag{4.9}$$

here α, β, γ and δ represent the number of Ag atoms per In atom for the Ag, Ag_2In, $AgIn_2$ and In phases, respectively. It follows for the three different growth regimes of the IMCs:

$$r < r_1 \rightarrow AgIn_2 \text{ grows; } Ag_2In \text{ shrinks} \tag{4.10a}$$

$$r_1 < r < r_2 \rightarrow AgIn_2 \text{ grows; } Ag_2In \text{ grows} \tag{4.10b}$$

$$r > r_2 \rightarrow AgIn_2 \text{ shrinks; } Ag_2In \text{ grows.} \tag{4.10c}$$

Using pure Ag and In, as well as stoichiometric Ag_2In and $AgIn_2$, values for r_1 and r_2 of 0.5 and 2.0 respectively, are obtained.

In the initial stages of IMC growth both IMCs have a vanishing thickness and consequently, are always growing interface-controlled. In this case the flux ratio r is given by [76]:

$$r = \frac{\Delta c^{eq}_{Ag_2In} \kappa^{eff}_{Ag_2In}}{\Delta c^{eq}_{AgIn_2} \kappa^{eff}_{AgIn_2}}, \tag{4.11}$$

where $\kappa^{eff}_{Ag_2In}$ and $\kappa^{eff}_{AgIn_2}$ are the effective reaction rate constants for describing the reactions at the interfaces of the Ag_2In and $AgIn_2$ IMCs, respectively (cf. Eqs. (4), (5) and (7) in Ref. [76]). $\Delta c^{eq}_{Ag_2In}$ and $\Delta c^{eq}_{AgIn_2}$ are the equilibrium concentration differences across the Ag_2In and $AgIn_2$ IMC layers, respectively (i.e. "so-called" local equilibrium is assumed at the interfaces of the IMCs).

Table 4.2: Comparison of diffusion coefficients D and activation energies Q as obtained in the present work as as presented in the literature.

Ref.	Process	D [$cm^2\ s^{-1}$]	Q [$kJ\ mol^{-1}$]
This work	Ag_2In interdiffusion	$2.23 \pm 0.02 \cdot 10^{-15}$ at RT	60.5 ± 9.2
[2]	Ag_2In interdiffusion	$1.1 \cdot 10^{-16}$ at RT	-
[28]	Ag_2In interdiffusion	$4.6 \cdot 10^{-11}$ at 150 °C	-
[22]	Ag_2In interdiffusion	-	44.9
[71]	Ag in In diffusion	$1.49 \cdot 10^{-14}$ at RT	53.6
[72]	In in Ag diffusion	$2.01 \cdot 10^{-31}$ at RT	170.1
[2]	$AgIn_2$ interdiffusion	$1.7 \cdot 10^{-15}$ at RT	-
[26]	$AgIn_2$ interdiffusion	$4.9 \cdot 10^{-13}$ at RT	44.4
[28]	$AgIn_2$ interdiffusion	$5.3 \cdot 10^{-13}$ at RT	44.4
[25]	Ag–In diffusion	$1.1 \cdot 10^{-16}$ at RT	41.5
[25]	Ag–In diffusion (grain boundary)	$3.9 \cdot 10^{-11}$ at RT	32.8

Note that in case of Ref. [25] it is not clear to which type of diffusion process the data should be referred to, as inappropriate models were used for the calculation of the diffusion coefficients.

During the very initial stage of the first regime, where interface-controlled growth of $AgIn_2$ prevails, Eq. 4.11 can be used to estimate the flux ratio r. As both Ag_2In and $AgIn_2$ are ordered IMCs with a more or less fixed stoichiometry, $\Delta c^{eq}_{Ag_2In}$ and $\Delta c^{eq}_{AgIn_2}$ are expected to be small and of the same magnitude (see Ref. [73]). However, $\kappa^{eff}_{Ag_2In}$ is expected to be significantly lower than $\kappa^{eff}_{AgIn_2}$, due to the larger volume misfit and much more complex crystal structure of Ag_2In compared to $AgIn_2$ (see above). Therefore, a r value smaller than $r_1 = 0.5$ is expected in the initial stages of the first regime and hence only the $AgIn_2$ IMC can be observed (see Eq. 4.10a).

A mixed growth mode is observed for $AgIn_2$ in the first regime (see Section 4.3.2), indicating that a very initial dominance of interface-controlled growth gets lost soon. However, the Ag_2In IMC remains kinetically suppressed, as the critical thickness of $AgIn_2$ is not surpassed, since this would require a *fully*-diffusion-controlled growth of $AgIn_2$.

The non-occurrence of fully diffusion-controlled growth for $AgIn_2$, suggests that the interdiffusion coefficients are very large in this IMC[3]. This can be related to its crystal structure. The structure consists of alternating layers of In and Ag atoms, when viewed along the c-axis. Ag and In atoms can therefore diffuse independently in directions

[3]The kinetic equation for the mixed growth mode [76] reduces to purely interface-controlled growth in case of large interdiffusion coefficients.

parallel to these layers without disturbing the ordered nature of the crystal structure of the IMC.

Even for specimens containing considerably more In as compared to Ag, as used in Refs. [2, 23, 25, 26], no Ag_2In IMC was observed.

In contrast with the results of the present work, diffusion-controlled growth of $AgIn_2$ was claimed in Refs. [2, 25, 26, 28] (the corresponding interdiffusion coefficients have been listed in Table 4.2). However, the analysis in Refs. [2, 25, 26, 28] was based on a plot of IMC layer thickness vs. $t^{1/2}$. Such plots should not be used for this purpose as they are sensitive to the choice of $t = 0$ (i.e. the onset of the diffusion-controlled growth). Instead a plot of squared IMC thickness vs. t should be used. The observed difference in growth mode for the $AgIn_2$ IMC between the present work and Refs. [2, 25, 26] could also be caused by the lower time resolution, as compared to the present work, used in the previous investigations, which might mask the presence of a mixed or even an interface-controlled growth regime.

4.4.2 Second Kinetic Regime

In the second regime, where no pure In is present, the amount of the $AgIn_2$ cannot increase further, as all In has been consumed. As long as pure Ag is left, the only reaction that can occur in this stage is the formation of Ag_2In from Ag and $AgIn_2$[4]. In specimens of similar relative layer thicknesses as in the current work, investigated in Refs. [2, 23], the Ag_2In IMC was readily observed also once no In reflections could be observed anymore in the XRD patterns, agreeing with the results of the present work.

The growth of Ag_2In is clearly diffusion-controlled (see Fig. 4.15), already suggesting that the interdiffusion coefficients of Ag_2In are smaller than the interdiffusion coefficients of $AgIn_2$, that showed a mixed growth mode, (see above). Due to the complex crystal structure of the Ag_2In IMC, the Ag and In atoms cannot move independently without disturbing the ordered nature of the crystal structure. One may thus expect a larger activation energy of the diffusion process in Ag_2In as compared to $AgIn_2$. Yet the value obtained for the activation energy of the interdiffusion in Ag_2In (60.5 ± 9.2 kJ mol^{-1} c.f. Section 4.3.3) is relatively small: The value for interstitial Ag diffusion in In is 53.5 kJ mol^{-1} [71], and the value for substitutional In diffusion in Ag is 170.1 J mol^{-1} [72]. This might indicate that the relatively fast diffusion mechanism in the Ag_2In IMC is carried by interstitial diffusion of the Ag atoms.

[4]The small amount of Ag_2In that was found at the higher temperatures in the first regime (where the In layer is still present) is probably due to the slight lateral inhomogeneity of the In sublayer thickness: the In layer can have completely reacted at the locations where the In layer is relatively thin (see Fig. 4.1 and its discussion), while the In layer is basically still present in the specimens.

The value of the RT interdiffusion coefficient of Ag_2In, as determined in Ref. [2] (see Table 4.2), is slightly smaller compared to the value obtained in the current work, whereas the value of the activation energy of the diffusion process, determined in the current work, is slightly larger than the one obtained in Ref. [22].

The change in growth mode of the Ag_2In IMC that is observed at RT (cf. Fig. 4.8d), can be interpreted as that the IMC initially grows interface-controlled or with a mixed growth mode and only later changes to the (slower) diffusion-controlled growth mode. Alternatively, it can be suggested that at the lowest temperature (RT) grain-boundary diffusion could also play a role and that the first fast mode could be dominated by this process. Then, if grain growth takes place upon aging at RT, the density of grain boundaries decreases, and a transition to a slower, volume diffusion controlled, growth mode can take place. At the higher temperatures the contribution of grain boundary-diffusion is less significant, as compared to that of volume diffusion, and thus the first, fast growth mode is not observed. It is noted that the change in growth mode of the Ag_2In IMC at RT, discussed here, was not observed in previous studies, due to their lower time resolution.

4.4.3 Tensile Stress Development

The tensile stress development in the the bilayer specimens at RT reflects the amount of IMCs formed in the specimens: in the initial stage a rapid increase (growth of $AgIn_2$ followed by fast growth of Ag_2In) and after about 1000 min a distinct decrease of stress increase (slower growth of Ag_2In). Considering the molar volumes of In [154], Ag [155], $AgIn_2$ [150] and Ag_2In [66], it follows that the formation of $AgIn_2$ from Ag and In, as well as the formation of Ag_2In from $AgIn_2$ and Ag, leads to an overall volume decrease. Conceiving the substrate as a rigid body and elastic accommodation of the layer-system / substrate misfit, it follows straightforwardly that a tensile stress must develop in the layer-system upon IMC development, as observed.

4.5 Conclusions

The precise sequence of the formation of IMCs and their growth modes in Ag–In bilayer specimens with In on top could be revealed due to the high time-resolution and fast data recording of the applied 2D XRD detector.

The reaction diffusion in the Ag–In bilayers is characterized by two kinetic regimes. The first regime is observed as long as the In layer has not been consumed: here an $AgIn_2$ IMC layer forms from Ag and In. In the second regime, which starts once the In layer has reacted completely, the Ag_2In IMC emerges.

IMC formation upon aging/annealing most likely initiates inside the In layer, due to the high mobility and the negligible solubility of Ag in the In layer. Then formation of $AgIn_2$ is thermodynamically preferred over Ag_2In, as indicated by a comparison of the Gibbs energies of formation per mole Ag. The formation of Ag_2In is also kinetically suppressed, due to the mixed interface / diffusion-controlled growth mode of $AgIn_2$. Only after all In has been consumed Ag_2In can be formed from the remaining $AgIn_2$ and the excess Ag.

The growth of $AgIn_2$ in the first regime is controlled by the reaction at the interfaces as well as the diffusional fluxes through the IMC layer, leading to a mixed growth mode.

The first, faster, growth mode of Ag_2In at RT indicates either at least partial interface control of the reaction, or a relatively high contribution of grain-boundary diffusion.

The second, slower growth mode of Ag_2In is diffusion-controlled and is observed at all temperatures studied. An interdiffusion coefficient of $D = 1.1 \pm 3.9 \cdot 10^{-4}$ cm^2 s^{-1} exp(-60.5 ± 9.2 kJ mol^{-1}R^{-1}T^{-1}) was derived from the Ag_2In IMC growth-constant data, suggesting rate control by interstitial diffusion in Ag_2In.

As a result of the IMC formation and the associated volume changes tensile stresses parallel to the surface develop in the bilayer specimens.

4.6 Acknowledgements

The authors thank Dr. G. Richter (Max Planck Institute for Intelligent Systems) for providing access to the thermal evaporation apparatus. The authors are also grateful to U. Eigenthaler (Max Planck Institute for Intelligent Systems) for the preparation of cross-sections of the bilayers for SEM analysis in the Dual-Beam instrument.

Chapter 5

Redetermination of the Crystal Structure of the Ag_3Sn Intermetallic Compound

P.J. Rossi[1], N. Zotov[1] and E.J. Mittemeijer[1,2]

[1] *Max Planck Institute for Intelligent Systems (formerly Max Planck Institute for Metals Research), Heisenbergstraße 3, D-70569 Stuttgart, Germany*

[2] *Institute for Materials Science, University of Stuttgart, Heisenbergstraße 3, D-70569 Stuttgart, Germany*

Abstract

Ambiguity exists in the literature on the crystal structure of Ag_3Sn: no agreement on neither the type of orthorhombic distortion nor the presence of ordering exists. Therefore, the exact crystal structure of Ag_3Sn has been reinvestigated using high resolution X-ray powder diffraction. By applying Rietveld refinements, it could be shown that Ag_3Sn is orthorhombic, with an ordered crystal structure of β-Cu_3Ti-type (space group $Pmmn$). The lattice parameters of a Sn-rich and an Ag-rich sample are $a = 4.78233(1)$ Å, $b = 5.99752(1)$ Å, $c = 5.16393(1)$ Å and $a = 4.78291(2)$ Å, $b = 5.98854(2)$ Å, $c = 5.15686(2)$ Å, respectively. The lattice parameters indicate a ϰ-type orthorhombic distortion.

5.1 Introduction

Two intermetallic compounds (IMCs), Ag_4Sn and Ag_3Sn, are known for the Ag-Sn system [54, 52]. Both compounds can be classified as Hume-Rothery electron compounds [47]. The Ag_4Sn IMC has a simple Mg-type hexagonal structure (space group $P6_3/mmc$). The structure of the Ag_3Sn IMC is related to the Mg-type hexagonal structure by an orthorhombic distortion of the hexagonal unit cell. Two different types of orthorhombic distortion can be discerned, i.e. a λ-type ($2c/b > \sqrt{3}$) distortion and a ϰ-type ($2c/b < \sqrt{3}$) distortion, as defined by Burkhardt and Schubert [57], which are shown in Fig. 5.1. The relations between the different structures are discussed in detail in the present work.

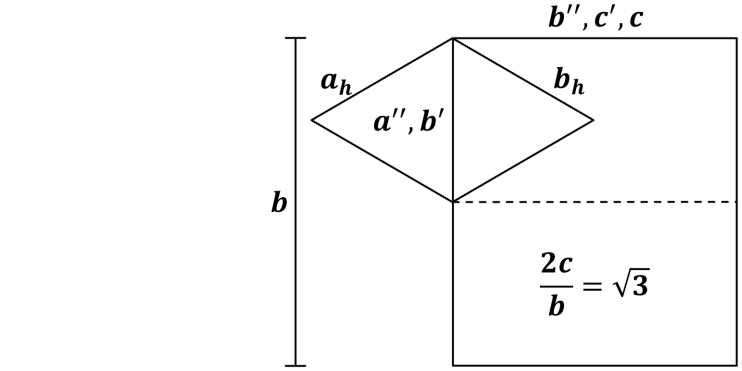

(a) undistorted

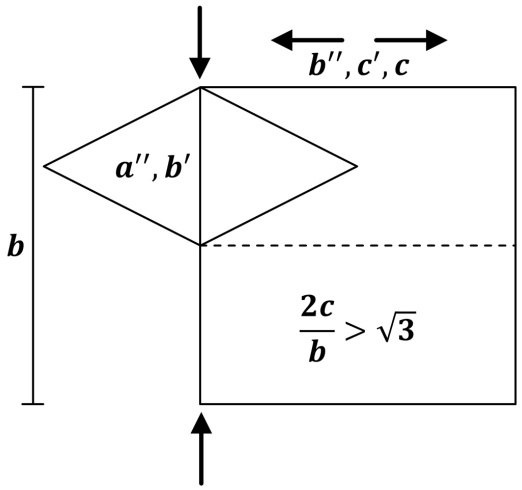

(b) λ-type distortion

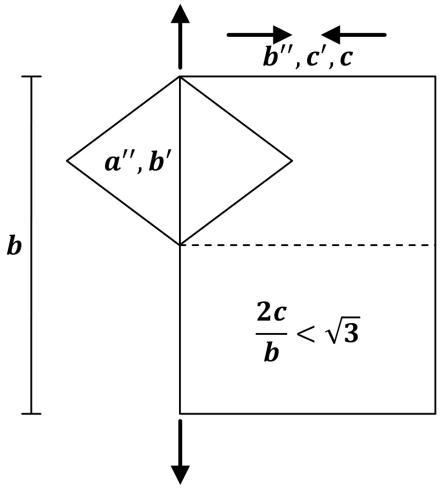

(c) ϰ-type distortion

Fig. 5.1: Relations of the hexgonal and orthorhombic unit cells and the two types of orthorhombic distortion of the hexagonal structure; unit cells are shown as projection along the hexagonal c_h axis. (a) shows the undistorted unit cells, (b) shows the λ-type distortion and (c) shows the ϰ-type distortion.

The Ag_3Sn phase readily forms in all Ag-Sn based Pb-free solders [39]; knowledge of the crystal structure of the Ag_3Sn phase is essential for understanding the behavior of Ag-Sn based solders.

The crystal structure of Ag_3Sn is controversially discussed in the available literature: (i) different types of orthorhombic distortion have been claimed to occur and (ii) disagreement prevails regarding the whether or not occurring of ordering on the Wyckoff sites in the Ag_3Sn structure.

Preston [55] obtained powder diffraction patterns from the filings of an ingot with a composition of 73.15 at.% Ag; 26.85 at.% Sn. The respective amounts of Ag and Sn were molten and annealed at 451 °C, 392 °C and 336 °C for 14 days each. The reflections in the powder diffraction patterns were compatible with a Mg-type hexagonal close packed structure. On the basis of Preston's results, Hume-Rothery [156] suggested an ordered hexagonal structure, which takes the stoichiometry of Ag_3Sn into account.

Nial et al. [56] were the first to suggest an orthorhombic structure for Ag_3Sn, as splitting of fundamental, hexagonal reflections was observed in powder diffraction patterns along with a $\varkappa$-type distortion. The presence of ordering could not be clarified by Nial et al. [56], due to the small differences in the atomic scattering factors of both elemental constituents. In the absence of ordering the structure corresponds to the disordered β-TiCu-type, space group *Cmcm*.

Burkhardt and Schubert [57] suggested an ordered structure based on the analogy with Cu_3Ge, which has a similar valence electron concentration.

An ordered structure with λ-type distortion (β-Cu_3Ti-type, space group *Pmmn*) was proposed by Fairhurst and Cohen [58], as weak superstructure reflections were found in this work indicating the presence of ordering. Fairhurst and Cohen [58] prepared Ag_3Sn powder as well as single crystals. Single crystals were prepared from melts with 58 at.% Sn. The melt was slowly cooled from 500 °C to 300 °C. As a next step the samples were quenched to 25 °C, which resulted in a mixture of solid Sn and Ag_3Sn. Ag_3Sn single crystals were freed from the obtained ingot by using concentrated HCl. The powder preparation is not detailed in this work. The powder was annealed at 300 °C for 15.5 h. Lattice parameters were obtained from discrete reflections in the powder patterns. The lattice parameters show a λ-type distortion. Superstructure reflections were observed using precession camera films applying long exposures (3 to 5 days). Hence the ordered β-Cu_3Ti-type structure was accepted for the Ag_3Sn phase. Atomic positions and anisotropic temperature factors were obtained by refinements of a trial structure. The trial structure was obtained on the basis of obtaining a close packed structure with Ag and Sn atoms. Refinements were done with integrated intensities of 55 peaks recorded on a single-crystal diffractometer.

A disordered structure with ϰ-type distortion (β-TiCu-type, space group space group *Cmcm*) was proposed by Ellner and Mittemeijer [60], as only splitted hexagonal reflections and no superstructure reflections were found. Ellner and Mittemeijer [60] prepared powders by melting the respective amounts of Ag and Sn in evacuated silica ampules filled with Ar. Several compositions in 1 at.% steps from $Ag_{73}Sn_{27}$ to $Ag_{76}Sn_{24}$ were prepared. The mixtures were homogenized at 350 °C for 1 day. The filed powder was annealed at 350 °C for 5 min. The weak superstructure reflections (see Section 5.3.2) were most probably simply missed in this work, due to short exposure times used.

Rönnebro et al. [61] studied the Li uptake in Ag-Sn mixtures for applications as anode materials in rechargeable Li-ion batteries. Ag-Sn mixtures were subjected to mechanical alloying. After the first alloying step Li chips were added and ball milling was continued to study the Li uptake of the alloyed Ag-Sn mixtures. Since Ag_3Sn was also present in the products, modeling occurred by Rietveld refinements. The structure proposed by Fairhurst and Cohen [58] was most probably chosen as starting point for these refinements. The refined Ag_3Sn structure corresponds to the ordered β-Cu_3Ti-type structure with the ϰ-type orthorhombic distortion. Moreover, no evidence for superstructure peaks can be observed in the published X-ray diffraction patterns (XRD), and their potential presence was not considered in this work.

In view of the above discussed conflicting reports on the crystal structure of Ag_3Sn, especially on the presence or absence of ordering and the type of orthorhombic distortion, this work intends to determine definitively the crystal structure of Ag_3Sn on the basis of Ag_3Sn powder specimens of precisely defined composition using high-resolution powder diffraction data, obtained at multiple wavelengths, in combination with Rietveld refinements.

5.2 Experimental

5.2.1 Specimens Preparation

Two Ag_3Sn powder specimens were prepared in order to reveal the dependence of the lattice parameters on composition: a Sn-rich sample possessing a small amount of pure Sn in excess to that of Ag_3Sn and an Ag-rich sample possessing a small amount of Ag_4Sn in addition to Ag_3Sn. In this way lattice parameters could be obtained on both the Sn-rich and the Ag-rich borders of the Ag_3Sn homogeneity range (between about 24 at.% Sn and 25 at. at room temperature% [54]). The alloys were prepared by encapsulating the respective amounts of Ag (4N, Lesker) and Sn (5N, Preussag) in silica ampules under an Ar atmosphere. The ampoules were heated to 700 °C and held for 1 h to melt the

raw materials and to produce a homogeneous liquid. The liquidus temperature at these compositions is about 665 °C [54]. The ampoules were subsequently slowly cooled to 490 °C in the course of 6 days in 10 °C steps. Next, slow cooling was continued in 1 °C steps from 490 °C to 470 °C within 6 days. Slow cooling was necessary as segregation effects occurred in fast quenched samples, which were difficult to remove during a subsequent homogenizing, annealing treatment. The ampoules were held and the solidified alloys thus (further) homogenized at 470 °C for 28 days. These long annealing times were necessary in order to obtain homogeneous cast alloys and to well establish the ordering of Ag and Sn. After the homogenizing treatment, a water quenching was applied while simultaneously fracturing the silica ampoule. In case of the Sn-rich sample powder was prepared from the bulk ingot by filing, using a diamond file, while mortar and pestle were used in case of the Ag-rich sample. The powders were sieved with 25 μm sieves. After sieving, the powders were again put into silica ampoules under an Ar atmosphere. To relief the stresses caused by the filing as well as the mortar and pestle process, the powders were annealed for 1 h at 400 °C, followed by water quenching. The exact compositions of the powders were determined using inductively coupled plasma optical electron spectroscopy (ICP-OES) with the following results: composition of 74.4 ± 0.8 at.% Ag; 26.6 ± 0.3 at.% Sn for the Sn-rich sample and a composition of 75.1 ± 0.8 at.% Ag; 24.9 ± 0.3 at.% Sn for the Ag-rich sample.

5.2.2 X-ray Diffraction Experiments

High-resolution XRD patterns of the Ag_3Sn powder were recorded with a Philips (PANalytical) MPD diffractometer in Bragg-Brentano geometry using Cu-Kα_1 radiation. The diffractometer was equipped with a X'Celerator linear position sensitive detector (PSD) covering a 2θ range of 2.214° (where 2θ is the diffraction angle). The Cu-Kα_1 radiation was obtained using a (111) curved Ge single crystal Johannson monochromator placed in the incident beam (see Chapter 12 of Mittemeijer and Welzel [100]). The tube was operated at 40 kV and 40 mA. The radiation emerged from a (12 x 0.4) mm spot under a take-off angle of 6°. A divergence slit of 0.25° and an anti-scatter slit of 5.0 mm were used. The illuminated area on the sample was restricted by a 20 mm mask. A 0.02 rad Soller slit was placed in the diffracted beam path. For the measurements the powder was put on a Si (5 1 1) substrate using isopropanol. XRD patterns were recorded from 10.0° 2θ to 155.0° 2θ with a step size of the measurement points of 0.004° in 2θ. The acquisition time at each measurement point was 50 s. The XRD patterns were recorded repeatedly and the intensities at every measurement point with the same 2θ value were summed up. In total 47 patterns (in repetition) were recorded in case of the Sn-rich spec-

Table 5.1: Experimental conditions for the X-ray diffraction experiments. LP denotes the refinable Lorentz-Polarization parameter.

	Cu-K$_{\alpha 1}$	**Ag-K$_{\alpha 1}$**
wavelength [Å]	1.540592	0.559421
LP parameter	27.3	9.825
2θ range [°]	10.0-155.0	2.0-59.5
data points in the refinement	36249	2394

imen and 6 patterns (in repetition) were recorded in case of the Ag-rich sample. More patterns were recorded for the Sn-rich specimen, as especially this specimen was used for the determination of the crystal structure of Ag_3Sn. It is noted that the powder, as put on the Si (511) substrate, revealed some preferred orientation.

In order to minimize the influence of the (weak) preferred orientation on the integrated intensities and to obtain more reflections of significant intensity at high 2θ angles, especially for the refinements of the temperature factors, XRD patterns were additionally recorded employing Ag-radiation in case of the Sn-rich sample. To this end a Stoe Stadi-P diffractometer was used, operating in transmission Debye-Scherrer geometry using Ag-Kα_1 radiation. Monochromatization was achieved with a Ge (111) monochromator in the incident beam. The patterns were recorded with a Dectris Mythen PSD, covering a 2θ range of 2°. A capillary with an inner diameter of 0.5 mm was used that contained the powder. XRD patterns were recorded from 2.0° 2θ to 59.5° 2θ with a step size of the measurement points of 0.024° in 2θ. The acquisition time at each measurement point was 17400 s. Details of the XRD measurements have been summarized in Table 5.1.

Rietveld refinements were done using the Topas 4.2 software (Bruker AG). The patterns obtained with Cu-Kα_1 radiation and with Ag-Kα_1 radiation were refined *simultaneously*. Lattice parameters, atomic positions and temperature factors were constrained to have the same values for both radiations. In addition, the temperature factors were constrained to have the same values for the same type of atom. Peak shapes were modeled using Pseudo-Voigt profiles of Thompson, Cox, and Hastings [157], modified by Young and Desai [158]. The background was fitted using Chebychev polynomials up to the 27 order. Preferred orientation was modeled using spherical harmonics up to the 8th order according to Järvinen [159]. Peak-shift corrections due to specimen displacement and zero error were performed. Further, the effects of the Lorentz-Polarization (LP) factor and surface roughness (microabsorption), according to the model of Pitschke, Mattern, and Hermann [160] in case of the patterns obtained with Cu-Kα_1 radiation in Bragg-Brentano geometry, were accounted for. The peak-shape, preferred orientation and peak-shift parameters were refined *separately* for each radiation.

5.3 Results and Discussion

5.3.1 Crystal Structure of Ag_3Sn, Group-Subgroup relations

The different structural types, appearing in the literature, for the description of the Ag_3Sn structure can be related on the basis of a group-subgroup scheme [161], see Fig. 5.2. The relations between the axis of the undistorted unit cells are apparent from Fig. 5.2 and are illustrated in Fig. 5.1, which shows the projections of the unit cells along the hexagonal c_h axis of the Ag_3Sn(h) structure (see what follows).

The structure of the ordered Ag_3Sn phase can be derived from a hypothetical hexagonal high-temperature disordered Ag_3Sn phase (denoted Ag_3Sn (h) above and hereafter). This aristotype (the basic high-symmetry structure type) Ag_3Sn(h), in which Ag and Sn randomly occupy the $2c$ position with fractional occupancies 3/4 and 1/4, respectively, is isotypical with Mg (space group $P6_3/mmc$). Ellner and Mittemeijer [60] claim that the Ag_3Sn(h) phase can be obtained by liquid quenching (the known stable phase diagram of the Ag-Sn system does not give evidence for its existence [54, 52]). The basal plane axes of the unit cell of the Ag_3Sn(h) have been indicated by a_h and b_h in Fig. 5.1 (a). The first step of the symmetry reduction is a "translationengleiche" transition of index 3 (t3) to the centered orthorhombic space group *Cmcm*. In this structure the Ag and Sn atoms randomly occupy the $4c$ Wyckoff positions. This structure has been proposed for Ag_3Sn by Nial et al. [56] as well as Ellner and Mittemeijer [60]. The structure type corresponds to β-TiCu. The axes in the $a-b$ plane of the unit cell are indicated by a'' and b'' in Figs. 5.1 (b) and (c). The next, second symmetry reduction is a "klassengleiche" transition of index 2 (k2) to the orthorhombic space group *Pmma*. The transition leads to the splitting of the $4c$ position into the $2e$ and $2f$ positions, which are randomly occupied by Ag and Sn atoms. The axes in the $b-c$ plane of the unit cell haven been indicated by b' and c' in Figs. 5.1 (b) and (c). This structure has not been proposed so far for Ag_3Sn. The next, third symmetry reduction is again a "klassengleiche" transition of index 2 (k2) to the space group *Pmmn*. As a consequence, the $2f$ position splits into the positions $2a$ and $2b$. The splitting enables ordering of the Ag and Sn atoms such that the Ag atoms occupy the $4e$ positions, as well as the $2b$ positions, whereas the Sn atoms occupy only the $2a$ positions. This leads to the β-Cu_3Ti-type structure for Ag_3Sn, as proposed by Fairhurst and Cohen [58] and Rönnebro et al. [61]. The axes in the $b-c$ plane of the unit cell of this structure have been indicated by b and c in Figs. 5.1 (b) and (c). The ordering leads to a doubling of the b'-axis, $b = 2b'$. Note that Fairhurst and Cohen [58] and Rönnebro et al. [61] have chosen the setting of the axes in such a way that the a-axis in the *Pmmn* unit cell corresponds to the hexagonal a_h axis and the b-axis corresponds to the hexagonal c_h-axis; in that case the occupied Wyckoff positions are $2a$, $2b$ and $4f$.

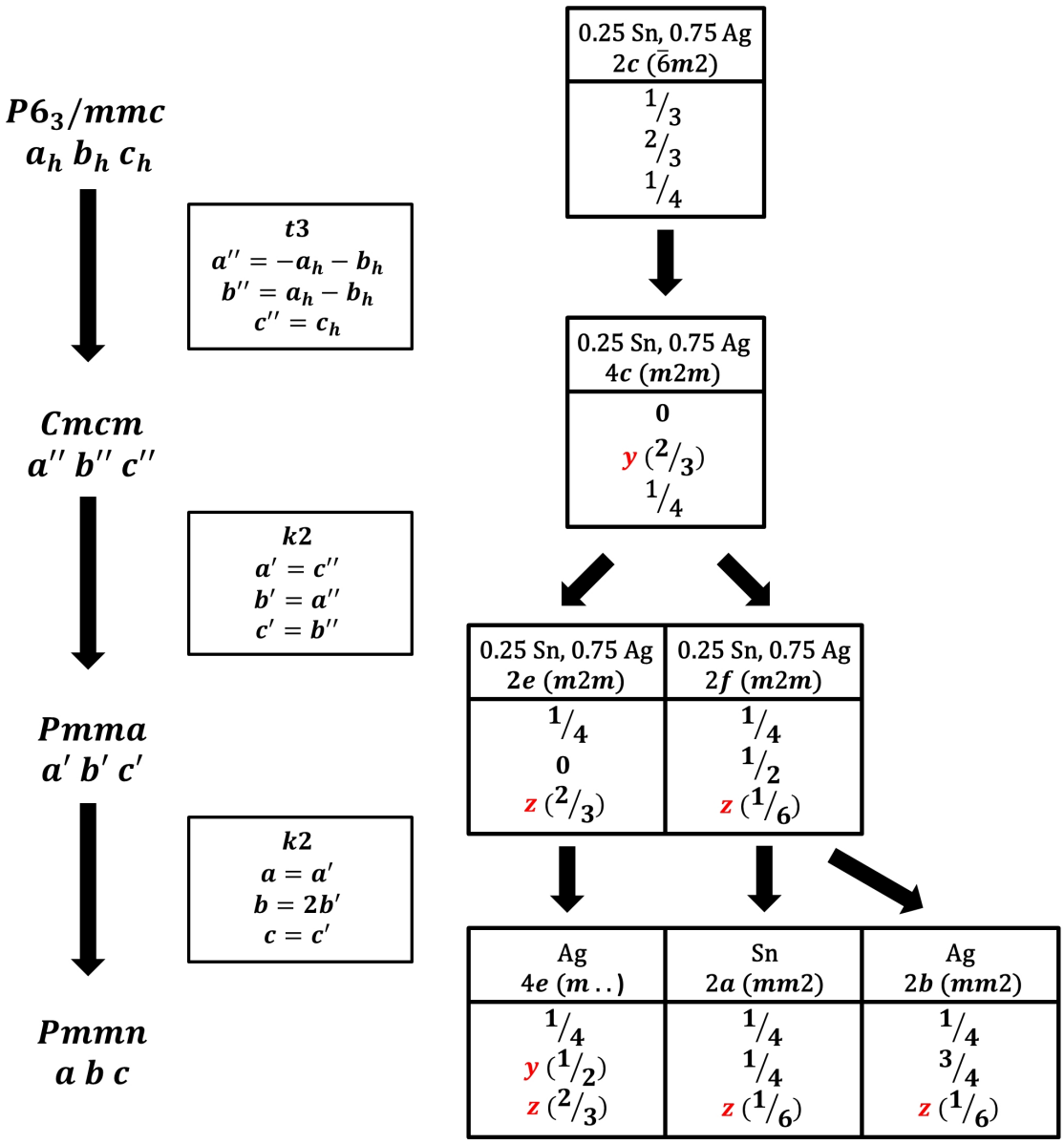

Fig. 5.2: Symmetry relations of the hexagonal and orthorhombic space groups. Ideal hexagonal positions have been given in parenthesis. Fractional coordinates, not fixed by symmetry, are indicated in red. The occupancy and the site symmetry of the different Wyckoff positions have been indicated too. See text for further details.

In the present work the axes have been chosen according to the symmetry relations of the space groups [161] (see Fig. 5.2).

Additionally, an orthorhombic distortion of the unit cell can be present in the *Cmcm*, *Pmma* and *Pmmn* space groups. Two different types of distortion are possible, as indicated in Fig. 5.1. They can be described by the ratio of specific axis of the unit cells, i.e. $2c/b$ for the *Pmmn* space group. For $2c/b < \sqrt{3}$ a so-called $\varkappa$-type distortion is obtained, whereas for $2c/b > \sqrt{3}$ a so-called λ-type distortion is obtained. For $2c/b = \sqrt{3}$ no orthorhombic distortion is present. The type of distortion has important consequences for the diffraction patterns. If a orthorhombic distortion is present all but the (h 0 0) fundamental hexgonal reflections split up into two separate reflections of different intensity. The type of distortion determines if the reflection with higher intensity appears on the high 2θ side or the low 2θ side of the doublet. The knowledge of the type of distortion of the Ag_3Sn structure is important for correctly indexing the Ag_3Sn reflections in a given diffraction pattern. This especially holds, if additional phases are present and an overlap of the individual peaks can occur. Nial et al. [56], Ellner and Mittemeijer [60] as well as Rönnebro et al. [61] concluded that a $\varkappa$-type distortion is present, whereas Fairhurst and Cohen [58] deduced the presence of a λ-type distortion. Note that the relations of the axes of the unit cells of the $P6_3/mmc$ and *Cmcm* space groups, as indicated in Fig. 5.1 and Fig. 5.2, are strictly valid only if no distortion is present; nevertheless they serve to indicate the relations between the different space groups.

In the orthorhombic space groups some atomic positions are not fixed by symmetry; these have been indicated (in red) by y and z in Fig. 5.2. However, "ideal hexagonal positions" can be indicated for these positions, if the atoms are assigned to the positions of the hypothetical Ag_3Sn(h) phase and stay there upon the above discussed "transformations" to the different orthorhombic unit cells. The values of these "ideal hexagonal positions" are shown in brackets in Fig. 5.2. Obviously, if no orthorhombic distortion is present and all atoms adopt "ideal hexagonal positions" and occupy these randomly, all structures discussed above become identical to Ag_3Sn(h).

In the *Pmmn* space group the deviations of (only) the y and z atomic positions from the "ideal hexagonal positions" (corresponding to the $P6_3/mmc$ space group) lead to the presence of weak reflections (in addition to the fundamental hexagonal reflections, which are splitted if an orthorhombic distortion is present). Therefore, from the sole presence of weak reflections it cannot be concluded if an ordered or statistical occupation of the Wyckoff sites persists. In case of an ordered occupancy of the Wyckoff sites, the intensities of the weak reflections possess contributions from both the displacements and the ordering. This can be exposed by explicit formulation of the structure factors of the weak superstructure reflections. As an example, the structure factor for the (111) reflection is

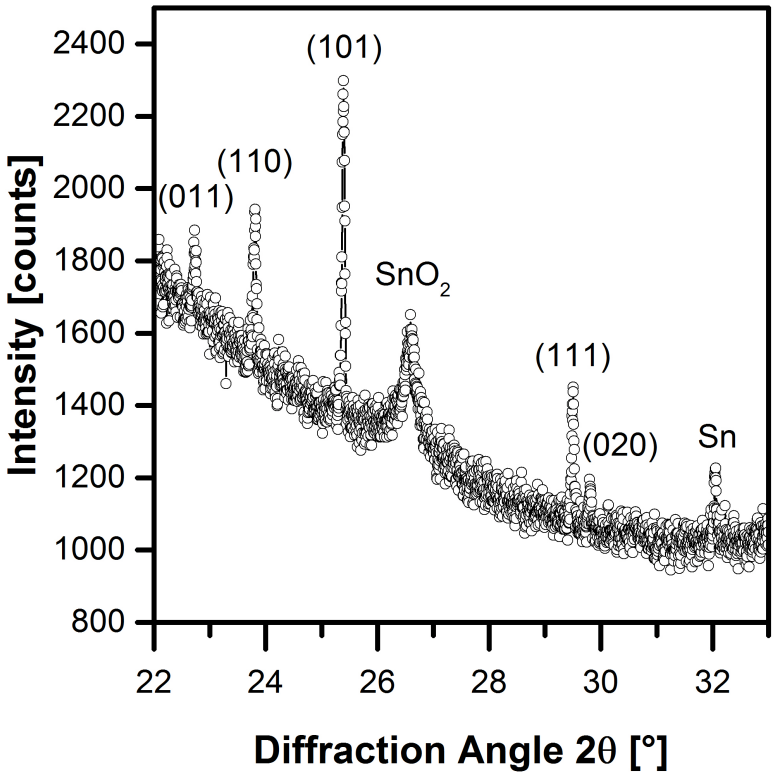

Fig. 5.3: Low-angle part of the XRD pattern, measured with Cu-$K_{\alpha 1}$ radiation, showing the presence of weak (superstructure) reflections. The pattern was obtained from the Sn-rich sample.

chosen, as it incorporates the effect of the shifts on all y and z atomic positions. For the ordered β-Cu_3Ti-type structure the structure factor of the (111) reflection (F_{111}) can be written, as a function of the "ideal hexagonal positions" and the atomic shifts from these positions, as follows:

$$\begin{aligned}
F_{111} =& f_{\mathrm{Ag}} 8 \sin(2\pi\frac{1}{4}) \sin(2\pi(\frac{1}{2}+\Delta y_{4e})) \cos(2\pi(\frac{2}{3}+\Delta z_{4e})) \\
&+ f_{\mathrm{Ag}} 8 \sin(2\pi\frac{1}{4}) \sin(2\pi(-\Delta y_{4e})) \cos(2\pi(\frac{2}{3}+\Delta z_{4e})) \\
&+ f_{\mathrm{Ag}} 8 \sin(2\pi\frac{3}{4}) \sin(2\pi(\frac{1}{2}-\Delta y_{4e})) \cos(2\pi(\frac{1}{3}-\Delta z_{4e})) \\
&+ f_{\mathrm{Ag}} 8 \sin(2\pi\frac{3}{4}) \sin(2\pi(\Delta y_{4e})) \cos(2\pi(\frac{1}{3}-\Delta z_{4e})) \\
&+ f_{\mathrm{Ag}} 8 \sin(2\pi\frac{1}{4}) \sin(2\pi\frac{3}{4}) \cos(2\pi(\frac{1}{6}+\Delta z_{2b})) \\
&+ f_{\mathrm{Ag}} 8 \sin(2\pi\frac{3}{4}) \sin(2\pi\frac{1}{4}) \cos(2\pi(\frac{5}{6}-\Delta z_{2b})) \\
&+ f_{\mathrm{Sn}} 8 \sin(2\pi\frac{1}{4}) \sin(2\pi\frac{1}{4}) \cos(2\pi(\frac{1}{6}+\Delta z_{2a})) \\
&+ f_{\mathrm{Sn}} 8 \sin(2\pi\frac{3}{4}) \sin(2\pi\frac{3}{4}) \cos(2\pi(\frac{5}{6}-\Delta z_{2a})),
\end{aligned} \tag{5.1}$$

where f_{Sn} and f_{Ag} are the atomic scattering factors of Sn and Ag, respectively. Δy and Δz are the atomic shifts for the y and z positions in the [010] and [001] directions from the ideal hexagonal positions at the $2a$, $2b$ and $4e$ sites.

In case of only ideal hexagonal positions (all Δy and Δz values are zero), it follows:

$$F_{111} = 8(f_{\mathrm{Sn}} - f_{\mathrm{Ag}}), \tag{5.2}$$

Hence, the structure factor vanishes ($F_{111} = 0$) and no (111) reflection can be observed for a statistical occupation of the Wyckoff sites, where both structure factors, f_{Sn} and f_{Ag}, in (5.2) have to be replaced by:

$$f_{\mathrm{stat}} = 0.25 f_{\mathrm{Sn}} + 0.75 f_{\mathrm{Ag}}. \tag{5.3}$$

However, in the presence of individual shifts for the y and z positions on the $2a$, $2b$ and $4e$ sites, a different situation arises. Arbitrarily adopting $\Delta z_{2a} = 0.01, \Delta z_{2b} = 0.02, \Delta y_{4e} = -0.03$ and $\Delta z_{4e} = 0.04$ the following structure factor is obtained:

$$F_{111} = 8(0.8893 f_{\mathrm{Sn}} - 0.9766 f_{\mathrm{Ag}}). \tag{5.4}$$

It can be seen that even for the case of a statistical occupation of the Wyckoff sites a weak (111) reflection can be observed:

$$F_{111} = 8(0.8893 f_{\mathrm{stat}} - 0.9766 f_{\mathrm{stat}}) = 8(-0.0873 f_{\mathrm{stat}}). \tag{5.5}$$

5.3.2 Rietveld Refinements

In case of the Sn-rich sample, weak reflections of pure Sn were present, in addition to the reflections of Ag_3Sn, whereas in the case of the Ag-rich sample weak reflections of Ag_4Sn were present in addition to the reflections of Ag_3Sn. The pure Sn phase partially transformed to SnO_2 during room temperature storage of the samples. The Sn-rich sample was chosen for the determination of the crystal structure of the Ag_3Sn phase, as the observed Sn and SnO_2 reflections do not overlap significantly with any of the Ag_3Sn reflections and therefore do not influence the Rietveld refinements.

The XRD pattern obtained with Cu-K_{α_1} radiation from the Sn-rich sample clearly shows the splitting of the hexagonal reflections due to an orthorhombic distortion. Furthermore, many weak reflections are present in addition to the fundamental, splitted hexagonal reflections. A selected number of those weak reflections are shown in Fig. 5.3. Several of the weak reflections have odd k Miller indices, if they are labeled in the *Pmmn* space group. This immediately rules out that the crystal structure of Ag_3Sn can

Table 5.2: Comparison of the results of Rietveld refinements adopting either the ordered or the disordered structural model of Ag_3Sn. Fit criteria are given in weighted pattern residuals (R_{wp}), Bragg factor (R_{Bragg}) and goodness of fit (GOF).

fit criterion	ordered	disordered
	Cu-radiation	
R_{wp} [%]	5.7	5.8
R_{Bragg} [%]	2.6	2.7
GOF	2.7	2.8
	Ag-radiation	
R_{wp} [%]	5.8	6.0
R_{Bragg} [%]	1.0	1.1
GOF	7.3	7.5
	combined	
R_{wp} [%]	5.7	5.9
GOF	3.2	3.2

be described on the basis of either the space group *Cmcm*, as proposed by Nial et al. [56] and Ellner and Mittemeijer [60], or the space group *Pmma* (cf. Fig. 5.2). It follows that the *Pmmn* space group, having a unit cell with $b = 2b' = 2a''$, has to be used to describe the structure.

The presence of the weak reflections does not necessarily indicate that an ordered structure is present (see Section 5.3.1). Therefore, two structural models have to be distinguished. One structural model adopts a random distribution of Ag and Sn over the $2a$, $2b$ and $4e$ sites, whereas the other structural model is based on compositional ordering with Ag on the $4e$ and $2b$ sites and Sn on the $2a$ sites. To determine which of these models reflects physical reality, Rietveld refinements were carried out for both models using the XRD patterns of both radiations (cf. Section 5.2.2) obtained from the Sn-rich sample. The resulting R_{wp}, R_{Bragg} as well as GOF parameters can be compared for both structural models in Table 5.2. R_{wp}, R_{Bragg} and GOF values are consistently smaller for the ordered structural model. Althought the differences between the values for the GOF, R_{wp} and R_{Bragg} parameters, as obtained for both structural models are not large, the inadequacy of the disordered model can be clearly demonstrated when comparing the intensities of the weak (superstructure) reflections: see Fig. 5.4. The complete Rietveld refinements of the Sn-rich sample are shown in Figs. 5.5 (a) and (b) (The SnO_2 peaks present in the diffraction patterns were modeled with an TiO_2-type structure (space group $P4_2/mnm$) according to Vegard [162]). The atomic positions and temperature factors for the ordered structural model, as determined by the *simultaneous*

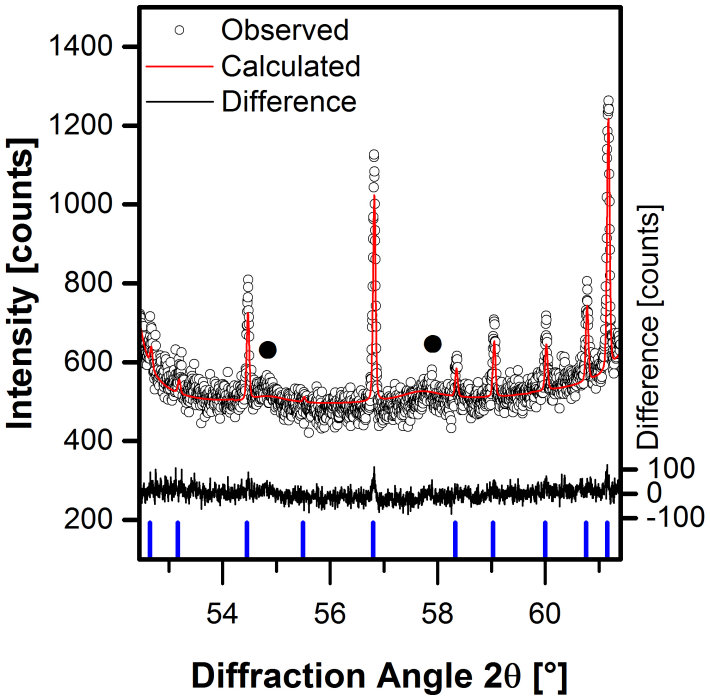

(a)

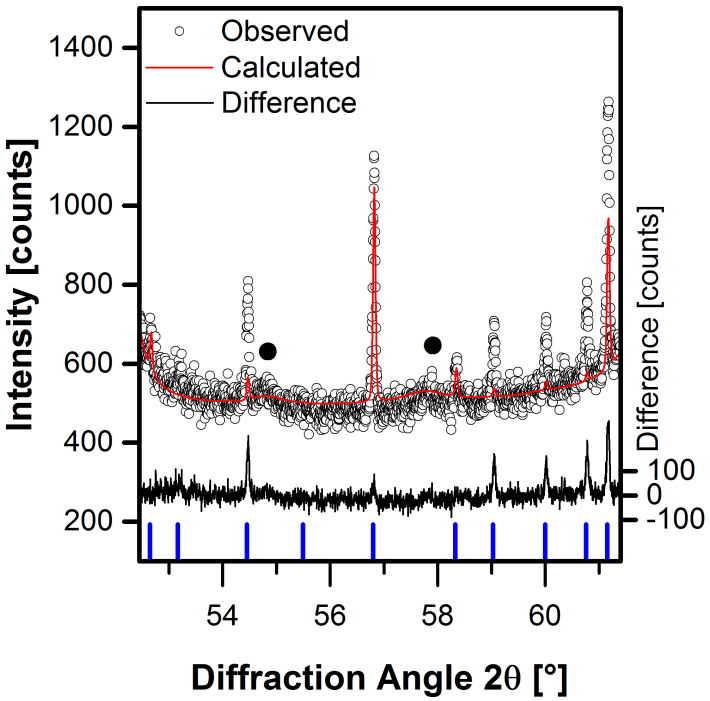

(b)

Fig. 5.4: Comparison of the refined diffraction patterns of the Sn-rich sample obtained with Cu-K_{α_1} radiation: (a) shows the ordered and (b) shows the disordered model structure. The symbol • indicates positions of reflections due to SnO_2.

Table 5.3: Structural parameters obtained, adopting the ordered structural model for Ag_3Sn, from Rietveld refinements simultaneously applied to the diffraction patterns recorded with Cu-Kα_1 and Ag-Kα_1 radiations.

atom	**site**	***x***	***y***	***z***	***occ.***	***B***
Ag	$4e$	1/4	0.5003(1)	0.6638(1)	1	0.57(1)
Ag	$2b$	1/4	3/4	0.1728(2)	1	0.57(1)
Sn	$2a$	1/4	1/4	0.1701(1)	1	0.33(2)

refinement of both (Cu-Kα_1 and Ag-Kα_1) XRD patterns of the Sn-rich sample, have been listed in Table 5.3. The three occupancies were refined and converged to 1.

Nevertheless, a *partial* disorder is in principal possible: either, (i) Ag atoms on the $4e$ site and occupancies of 1/2 for Sn and Ag on $2a$ and $2b$ sites, or (ii) occupancies of 1/2 for Sn and Ag on $4e$ sites and Ag on $2a$ and $2b$ sites would satisfy the stoichiometry of the Ag_3Sn IMC. Rietveld refinements show that, as in case of the disordered structure, several of the observed weak reflections are not properly modeled using structural models with such occupancies. However, upon closer investigation of the background in Fig. 5.5, a distinctive structure can be seen. It may be suggested that this diffuse intensity is caused by a weak partial substitutional disorder.

The proposal of Ellner and Mittemeijer [60] of a random occupation of Wyckoff sites could be simply due to too short counting times applied by Ellner and Mittemeijer [60], as it was already pointed out by Nial et al. [56] that superstructure reflections will be of very low intensity, due to the similarities of the atomic scattering factors of Ag and Sn. In the present work very long counting times were used in order to be able to observe the superstructure reflections.

Lattice parameters were obtained from the Rietveld refinements of the diffraction patterns recorded from both the Ag-rich specimen and the Sn-rich specimen (the Ag_4Sn that was additionally present in the Ag-rich specimen was modeled with an Mg-type (space group $P6_3/mmc$) hexagonal structure according to King and Massalski [51]). For both specimens, the lattice parameters are in agreement with a $\varkappa$-type orthorhombic distortion. This shows that the type of orthorhombic distortion is not a function of composition, which might have explained the different types of distortion that were proposed in the previous literature for Ag_3Sn. A comparison of the lattice parameters determined in this work, for the Ag-rich specimen and the Sn-rich specimen, with the lattice parameters reported by Nial et al. [56] and Ellner and Mittemeijer [60], for the compositions richest in Ag and richest in Sn, is provided by Table 5.4. Note the correspondences of the different axis, as provided by the discussion in the previous subsection (cf. Section 5.3.1) and shown in Fig. 5.1.

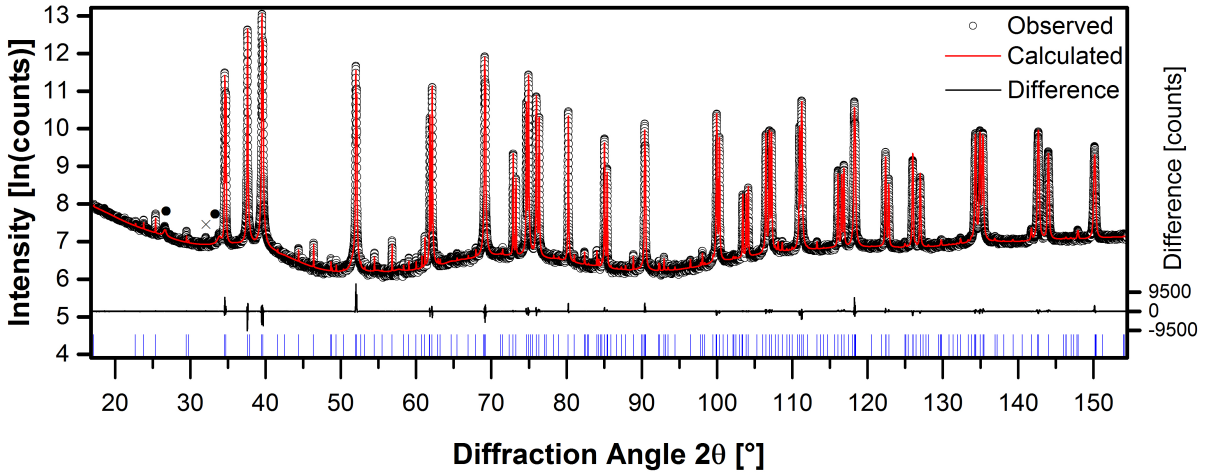

(a)

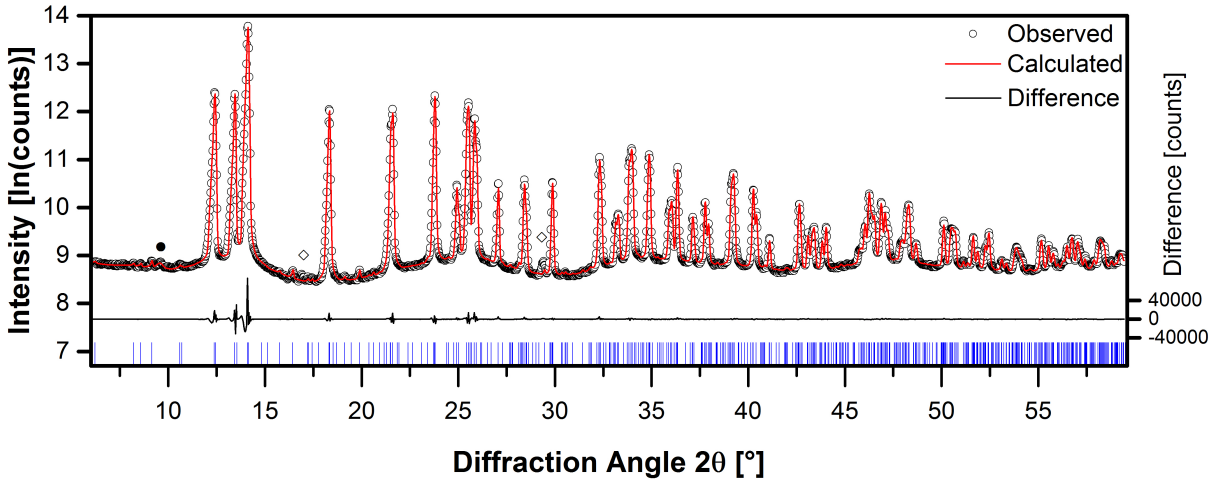

(b)

Fig. 5.5: XRD patterns obtained from the Sn-rich sample using Cu-K_{α_1} (a) and Ag-K_{α_1} (b) radiation. The XRD patterns have been refined simultaneously with the β-Cu_3Ti-type structural model. The symbols • and × indicate observed weak reflections by SnO_2 and Sn, respectively. The symbol ◇ indicates additional peaks which are artifacts due to radiation scattered by the goniometer.

Table 5.4: Comparison of the lattice parameters obtained from Rietveld refinements, with the ordered model structure for Ag_3Sn in the present study, with literature data. Refer to text and Figs. 5.1 and 5.2 for the relations between the lattice parameters.

lattice parameters [Å]		**distortion**
present work		
Ag-rich	Sn-Rich	
$a = 4.78291(2)$	$a = 4.78233(1)$	
$b = 5.98854(2)$	$b = 5.99752(1)$	$\varkappa$-type
$c = 5.15686(2)$	$c = 5.16393(1)$	
[56]		
Ag-rich	Sn-Rich	
$c'' \triangleq a = 4.7712$	$c'' \triangleq a = 4.7712$	
$2a'' \triangleq b = 5.970$	$2a'' \triangleq b = 5.988$	$\varkappa$-type
$b'' \triangleq c = 5.144$	$b'' \triangleq c = 5.154$	
[60]		
Ag-rich	Sn-rich	
$c'' \triangleq a = 4.785(1)$	$c'' \triangleq a = 4.783(1)$	
$2a'' \triangleq b = 5.988(1)$	$2a'' \triangleq b = 5.997(1)$	$\varkappa$-type
$b'' \triangleq c = 5.159(1)$	$b'' \triangleq c = 5.1635(1)$	

The present work shows unambiguously that the Ag_3Sn structure has a $\varkappa$-type distortion. The λ-type distortion was only observed by Fairhurst and Cohen [58]. The lattice parameters reported by Fairhurst and Cohen [58] were obtained from selected powder diffraction reflections, using the extrapolation by Nelson and Riley [163]. Some of those reflections were reported by Fairhurst and Cohen [58] to be of low intensity and poorly defined. Therefore the use of those peaks for lattice-parameter determination could have lead to erroneous values, leading to the incorrect suggestion of a λ-type distortion. Additional experiments applying concentrated HCl on Ag_3Sn powders, done in the present work, led to the transformation of Ag_3Sn to Ag_4Sn. It can therefore be suggested that the use of concentrated HCl by Fairhurst and Cohen [58] (see Section 5.1) led to non-equilibrium lattice parameters of the Ag_3Sn phase, explaining the seemingly observed λ-type distortion.

5.3.3 Conclusions

The crystal structure of Ag_3Sn has been reinvestigated using high-resolution X-ray powder diffraction employing Cu-Kα_1 and Ag-Kα_1 radiations and applying Rietveld refinements.

- Numerous very weak superstructure reflections were observed upon applying very long counting times, in addition to the splitted fundamental hexgonal reflections, thereby excluding the crystal structure of space group *Cmcm*, as previously proposed.
- The crystal structure of Ag_3Sn can be described by the ordered β-Cu_3Ti-type (space group *Pmmn*).
- The lattice-parameter values indicate a $\varkappa$-type orthorhombic distortion.

5.4 Acknowledgements

The authors thank Prof. Dr. R. E. Dinnebier (Max Planck Institute for Solid State Research) for providing the Debye-Scherrer diffractometer, as well Mrs. C. Stefani (Max Planck Institute for Solid State Research) for the diffraction measurements in Debye-Scherrer geometry. The authors are also grateful for the helpful discussions with Prof. Dr. A. Leineweber (Max Planck Institute for Intelligent Systems).

Chapter 6

Summary

6.1 Summary

Only few systems exist, which allow the investigation of interdiffusion and IMC formation at ambient temperatures. A large scientific interest exists in these systems, since they give insight to the extraordinarily fast diffusional processes operating already at room temperature. Furthermore, such systems are technologically important as a basis for modern Pb-free solders. However, scientific investigations of the fundamental processes of interdiffusion and IMC is relatively scarce in some of the systems, as i.e. in the Ag–Sn and Ag–In systems. Therefore, interdiffusion, IMC formation and the associated microstructural changes in Ag–Sn as well as Ag–In thin-film bilayer specimens were investigated in the present thesis.

The investigation of thermally evaporated Ag–Sn bilayer specimens, as presented in Chapter 2, showed that IMCs develop readily even at room temperature. Interestingly it was also shown that the type of IMCs present in the as-deposited state depends on the stacking sequence of the individual sublayers: only Ag_4Sn is present in "Ag on top of Sn" type bilayers, while predominantly Ag_3Sn, along with a small amount of Ag_4Sn, was present for "Sn on top of Ag" type bilayers.

The microstructure of the two types of bilayer is also distinctly different. Whereas in case of the "Sn on top of Ag" type bilayers the Sn and Ag sublayers show dense microstructures, large macroscopic voids are present within the Sn sublayer in case of the "Ag on top of Sn" type bilayers. The voids are caused by the Kirkendall effect, which occurs due to a large diffusional flux of Sn into the Ag layer.

The large diffusional flux only occurs in case of the "Ag on top of Sn" type bilayers, due to the large differences in surface energies of Ag and Sn. The surface energy of Ag is only about half that of Sn, hence the energy of the system is reduced if the Sn atoms segregate on the surface of the growing Ag layer. This causes an additional driving force, apart from the negative Gibbs energy of mixing, for Sn diffusion into the Ag layer.

The uptake of Sn into the growing Ag layer lowers the stacking fault energy of Ag in case of the "Ag on top of Sn" type bilayers and leads to a heavily faulted microstructure

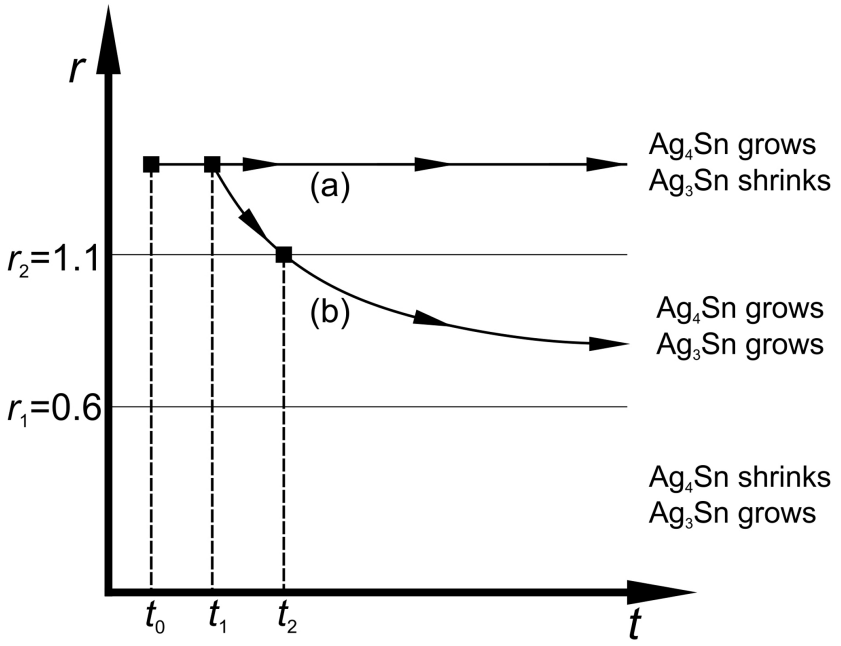

Fig. 6.1: Development of the flux ratio r during deposition of the Ag–Sn bilayer samples. For the "Ag on top of Sn" type bilayers flux ratio remains constant at least until the as-deposited state, due to the prevailing interface controlled growth of Ag_4Sn (a). Therefore, the Ag_3Sn IMC remains kinetically suppressed. For the "Sn on top of Ag" type bilayers (b) IMC growth eventually changes to diffusion controlled growth (at time t_1), decreasing the flux ratio r and enabling the formation of Ag_3Sn along with Ag_4Sn.

of the Ag layer, containing distinctive planar faults. The microstructural defects and the diffusional flux of Sn into the Ag layer are reflected by a diffuse intensity band, which could be observed between the Ag (200) and the Ag_4Sn (011) reflections in XRD patterns of the as-deposited state.

Recognizing the diffusional fluxes during deposition of the bilayer specimens, the energy released upon nucleation of the IMCs was assessed on a thermodynamic basis. In case of the "Ag on top of Sn" type bilayers, the IMCs are expected to form inside the Ag layer, due to the diffusional flux of Sn into the Ag layer. Then in order to estimate energy release upon nucleation of the IMCs from the solid solution of Sn in Ag, the amount of Gibbs energy released *per mole reacting Sn* has to be considered. To this end the partial Gibbs energies of Ag and Sn in the solid solution were estimated and the Gibbs energies per mole of reacting Sn were calculated. The calculations showed that initial nucleation of Ag_4Sn is thermodynamically preferred. However, in case of the "Sn on top of Ag" type bilayers, the large mobility of the Ag atoms inside the Sn layer, due to the interstitial diffusion mechanism, favors nucleation of the IMCs inside the Sn sublayer. As Sn has practically no solubility for Ag, the Gibbs energy release *per mole reacting Ag*, upon nucleation of the IMCs from pure Ag and Sn, was considered in this case. The

calculations showed that in this case more energy is released per Ag atom upon nucleation of Ag_3Sn compared to Ag_4Sn. Hence initial nucleation of Ag_3Sn is thermodynamically preferred in the "Sn on top of Ag" type bilayers.

In order to fully explain the results of the Ag–Sn bilayers, kinetic considerations had to be taken into account as well. On the basis of a kinetic model for IMC growth in binary diffusion couples, as proposed in the literature, the IMCs present in the as-deposited state of the Ag–Sn bilayers could be explained. In the initial stages of IMC growth in the Ag–Sn system, where the growth kinetics are controlled by the reactions at the interfaces of the IMC layers, the flux ratio r of the Ag atoms in the Ag–Sn bilayer specimens is such that only the Ag_4Sn IMC can be observed (see Fig. 6.1, at time t_0). The formation of Ag_4Sn is so fast that the growth of Ag_3Sn in this stages is kinetically suppressed. With increasing thickness of the growing Ag_4Sn layer, the growth kinetics is eventually controlled by the diffusional flux through the IMC layer (t_1 in Fig. 6.1). The flux ratio r will decrease, which eventually enables the formation of Ag_3Sn along with Ag_4Sn (t_2 in Fig. 6.1). This situation describes the "Sn on top of Ag" type bilayers in the as-deposited state (see (b) in Fig. 6.1).

On the other hand in the "Ag on top of Sn" type bilayers the diffusional flux is increased, due to the additional driving force caused by the surface energy difference. Hence, the growth of Ag_4Sn remains interface-controlled, at least until the as-deposited state (see (a) in Fig. 6.1). Consequently, only Ag_4Sn is observed for this kind of bilayers.

The textures of the individual sublayers also depend on the stacking sequence of the evaporated Ag–Sn bilayers. Thermal evaporation favors the nucleation of grains with their most densely packed planes parallel to the substrate surface, correspondingly, both the Sn and Ag sublayers have {100} and {111} fibre textures, respectively. However the Ag top sublayer shows a {100} fibre-texture, due to coherent/epitaxial growth of Ag grains on the underlying Sn grains.

Contrary to the Ag–Sn bilayers deposited by thermal evaporation, the IMCs present in the as-deposited state of magnetron sputtered Ag–Sn bilayers did not depend on the stacking sequence of the sublayers (see Chapter 3). Predominantly Ag_3Sn is present in both stacking sequences of the sputtered Ag–Sn bilayers. The results could be explained in terms of the different atomistic processes of both deposition methods. Compared to the thermally evaporated particles, the sputtered particles posses a much greater kinetic energy, leading to the formation of an increased intermixed zone in the sputtered layers, as compared to the thermally evaporated layers. The additional driving force for Sn diffusion, due to the surface energy difference, is therefore not present in the sputtered "Ag on top of Sn" bilayers, as the intermixing already leads to a reduction of the surface energy of Ag. Consequently, the increased diffusional flux of Sn into the Ag layer is

absent in the sputtered "Ag on top of Sn" bilayers and macroscopic Kirkendall voids cannot be observed. Additionally, high energetic sputtered Ag atoms create defects on the surface of the Sn bottom layer, acting as possible nucleation sites for the IMCs. The nucleation barrier for the ordered (see below) Ag_3Sn IMC is reduced, due to this additional nucleation sites. Furthermore, magnetron sputtering produces microstructures without stacking faults, while such stacking faults are present in thermally evaporated layers and favor the formation of the hexagonal Ag_4Sn IMC. The combination of all of the above mentioned effect leads to the preferred formation of Ag_3Sn instead of Ag_4Sn in magnetron sputtered "Ag on top of Sn" bilayers. In contrast to the thermally evaporated layers, the reduction of the nucleation barriers and the constant bombardment of the growing sublayers with high energetic particles leads to weakly or even untextured magnetron sputtered films.

In Chapter 4 the kinetics of IMC formation in the Ag–In system were investigated at room- as well as at elevated temperatures. As for the Ag–Sn system, the IMCs present in the as-deposited state of the Ag–In bilayer specimens depends on the stacking sequence of the sublayers. Only $AgIn_2$ is present in case of the "In on top of Ag" type bilayers, whereas $AgIn_2$ as well as Ag_2In are present in "Ag on top of In" type bilayers. The surface energies of Ag and In are similar as in case of the Ag–Sn system. Again the surface energy of In as about half that of Ag, suggesting a similar explanation for this effect as holds for the Ag–Sn bilayer specimens.

For the investigations of the kinetics of IMC formation only "In on top of Ag" type bilayers were used, as the presence of only one IMC in the as-deposited state simplifies the kinetic analysis. A 2 dimensional XRD detector was used to achieve a high time resolution, which was not available in previously published works. The XRD patterns revealed the presence of 2 distinct growth regimes, coinciding with the presence/absence of the In sublayer in the bilayer specimens. In the first growth regime $AgIn_2$ grows between the Ag and In sublayers. In the second growth regime, which starts once the In layer has reacted completely, Ag_2In forms and grows between the Ag and $AgIn_2$ layers.

Due to the fast interstitial diffusion mechanism of the Ag atoms inside In, it seems likely that in the first growth regime the IMCs nucleate inside the In layer. Since the In layer has practically no solubility for Ag, the Gibbs energy change upon IMC formation can be estimated similar to the "Sn of top of Ag" bilayers (see above). It was shown that more energy is released *per mole reacting Ag* upon the formation of $AgIn_2$ as compared to the formation of Ag_2In, favoring the initial formation of this IMC. However, the second growth regime clearly showed the nucleation and growth of Ag_2In, indicating a kinetic origin of the suppression of Ag_2In in the first growth regime. And indeed it was shown, using the same kinetic model, that has been applied to the Ag–Sn system, that $AgIn_2$

probably grows so fast that no Ag_2In can be observed initially. Only the depletion of the In layer eventually enables the formation of Ag_2In in the second growth regime.

The growth mode of $AgIn_2$ in the first growth regime could neither be described by fully diffusion-controlled kinetics, nor by fully interface-controlled kinetics. However, a mixed growth mode with contributions from the diffusion processes as well as the reactions of the interface could adequately describe the growth of $AgIn_2$. This is in contrast to the diffusion-controlled growth that has been observed in the available literature on the $AgIn_2$ growth kinetics. Two different growth modes of Ag_2In were observed at room temperature. The second, later occurring slower growth mode, which is the only growth mode observed at elevated temperatures, is clearly diffusion-controlled with a diffusion coefficient of $D = 1.1 \pm 3.9 \cdot 10^{-4}$ cm^2 s^{-1} exp(-60.5 ± 9.2 kJ mol^{-1}R^{-1}T^{-1}). The initial faster growth mode of Ag_2In is most likely again a mixed growth mode.

The formation of the IMCs leads to the development of residual tensile stresses in the "In on top of Ag" bilayer specimens. The tensile stress develops due to the volume increase associated with the formation of the IMCs.

Due to the conflicting results, published in the available literature, about the presence of ordering as well as the type of orthorhombic distortion (λ-type or ϰ-type) in the crystal structure of the Ag_3Sn IMC, a discussion of the various reported crystal structures in terms of their group-subgroup relations, unit cells and orthorhombic distortions was given in Chapter 5. In order to determine the correct crystal structure of Ag_3Sn, powder specimens were prepared and measured with high-resolution powder XRD. Attention has been paid to the preparation of the powder specimens, in order to obtain powders suitable for XRD without preparation artifacts. A prolonged annealing procedure was necessary in order to obtain homogenized bulk ingots in thermodynamic equilibrium. This showed that some of the inconsistencies in the available literature could well be due to improper homogenizing treatments. Some experiments showed that chemical treatment of the Ag_3Sn powder specimens, altered their composition. Such treatments were used in another investigation to obtain Ag_3Sn specimens. This might explain why a differing distortion type was obtained in this work as compared to the majority of the remaining works.

The XRD measurements were performed using long counting times in connection with one dimensional position sensitive detectors in order to obtain diffraction patterns with high signal-to-background ratios. The diffraction patterns showed the presence of additional weak (superstructure) reflections in addition to the (splitted) fundamental hexagonal reflections. It was shown that in case of the Ag_3Sn IMC these additional weak reflection are not necessarily caused by an order occupation of the Wyckoff positions. Deviations of individual atoms from so-called "ideal hexagonal" positions can also cause

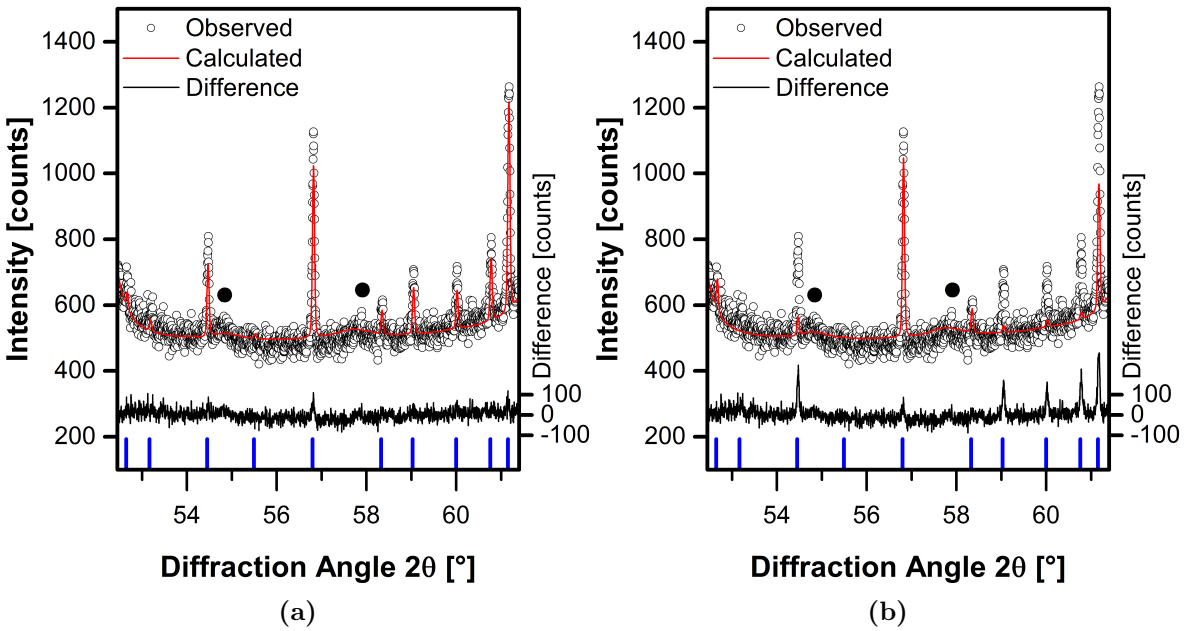

Fig. 6.2: Comparison of the refined diffraction patterns: (a) shows the refinement using the ordered and (b) shows the refinement using the disordered model structure. It can clearly be seen that an ordered model structure is necessary in order to adequately model all of the reflections. The symbol • indicates positions of reflections due to SnO_2.

the occurrence of these additional weak reflections. However, using Rietveld refinements, it was unambiguously shown that an ordered occupation of the Wyckoff positions is necessary in order to adequately describe the obtained XRD patterns (see Fig. 6.2).

Consequently, the results of the refinements clearly show that the crystal structure of Ag_3Sn is an ordered β-Cu_3Ti-type (space group *Pmmn*) with a ϰ-type orthorhombic distortion. Specimens of different compositions were investigated in order to demonstrate that the distortion type is not a function of composition.

6.2 Zusammenfassung

Nur wenige Systeme eignen sich für die Untersuchung von Interdiffusion und intermetallischer Phasenbildung bei Umgebungstemperaturen. Solche Systeme sind von großem wissenschaftlichen Interesse, da sie Einblicke in die außergewönlich schnellen Diffusionsvorgänge bieten, die bereits bei Raumtemperatur aktiv sind. Weiterhin sind diese Systeme technisch relevant, da sie sich als Basis für Pb-freie Lote eignen. In einigen dieser Systeme, wie z.B. Ag–Sn und Ag–In, existieren jedoch nur wenige wissenschaftliche Untersuchungen der grundlegenden Vorgänge von Interdiffusion und intermetallischer Phasenbildung. Deshalb wurde in der vorliegenden Arbeit Interdiffusion, die Bildung intermetallischer Phasen und die damit verbundene Änderung der Mikrostruktur in Ag–Sn und Ag–In Doppelschichten dünner Filme untersucht.

In Kapitel 2 wurde gezeigt, dass sich in thermisch aufgedampften Ag–Sn Doppelschichten intermetallische Phasen bereits bei Raumtemperatur deutlich ausbilden. Es konnte ebenfalls gezeigt werden, dass die Art der direkt nach der Abscheidung vorkommenden Phasen von der Stapelsequenz der jeweiligen Subschichten abhängt: bei Doppelschichten der Art „Ag auf Sn" ist nur Ag_4Sn vorhanden, während bei Doppelschichten der Art „Sn auf Ag" hauptsächlich Ag_3Sn neben einer kleinen Menge an Ag_4Sn vorhanden sind.

Die Mikrostruktur unterscheidet sich ebenfalls deutlich zwischen den beiden Arten der Doppelschichten. Während die Subschichten der „Sn auf Ag" Doppelschichten eine dichte Mikrostrukture ausbilden, befinden sich in der Sn Subschicht der „Ag auf Sn" Doppelschichten makroskopisch große Poren. Die Poren entstehen durch den Kirkendall-Effekt, der durch einen starken Diffusionsfluss von Sn in die Ag-Schicht verursacht wird.

Dieser starke Diffusionsfluss in den „Ag auf Sn" Doppelschichten entsteht durch die unterschiedlichen Oberflächenenergieen von Ag und Sn. Da die Oberflächenenergie von Ag nur halb so groß ist wie die Oberflächenenergie von Sn, kann die Energie des Systems durch Segregation von Sn auf der Oberfläche der sich im Wachstum befindlichen Ag-Schicht erniedrigt werden. Neben der negativen Mischungs-Gibbsenergie bedingt dies eine zusätzliche Triebkraft für die Diffusion von Sn in die Ag-Schicht.

Im Fall von den „Ag auf Sn" Doppelschichten, erniedrigt die Inkorporation von Sn in die wachsende Ag-Schicht die Stapelfehlerenergie von Ag und führt zu einer stark gestörten Mikrostruktur mit charakteristischen Flächenbaufehlern. Die gestörte Mikrostruktur und der Diffusionsfluss von Sn in die Ag-Schicht führen zum Auftreten eines diffusen Intensitätsbands zwischen dem Ag (200) und dem Ag_4Sn (011) Reflex in den direkt nach der Abscheidung aufgenommenen Röntgenbeugungsdiagrammen.

Unter Zuhilfenahme der Diffusionsflüsse während der Abscheidung der Doppelschichten konnte die Energieänderung bei der Keimbildung der intermetallischen Phasen abge-

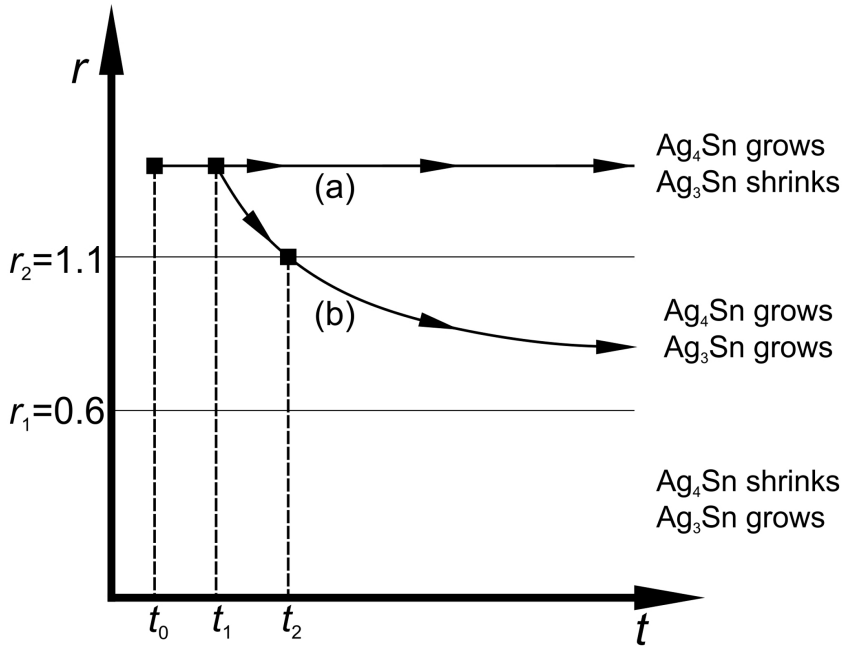

Abbildung 6.3: Verlauf des Verhältnisses der Flüsse r während der Abscheidung der Ag–Sn Doppelschichten. Im Falle der „Ag auf Sn" Doppelschichten bleibt das Verhältnis der Flüsse durch das vorherrschende, diffusionskontrollierte Wachstum von Ag_4Sn zumindest bis direkt nach der Abscheidung konstant (a). Somit bleibt die intermetallische Phase Ag_3Sn kinetisch unterdrückt. Im Falle der „Sn auf Ag" Doppelschichten (b) wird das Wachstum der Intermetalliken letztendlich diffusionskontrolliert (Zeitpunkt t_1), was das Verhältnis der Flüsse r herabsetzt und die Bildung von Ag_3Sn neben Ag_4Sn ermöglicht.

schätzt werden. Wegen des Diffusionsflusses von Sn in die Ag-Schicht, im Falle der „Ag auf Sn" Doppelschichten kann davon ausgegangen werden, dass sich die intermetallische Phasenbildung in der Ag-Schicht abspielt. Um in diesem Fall die Energieänderung bei der Keimbildung der intermetallischen Phasen aus dem Mischkristall von Sn in Ag abschätzen zu können, muss die Gibbs-Energieänderung *pro Mol reagierendem Sn* betrachtet werden. Hierzu wurden die partiellen Gibbs-Energien von Ag und Sn im Mischkristall abgeschätzt und damit die Gibbs-Energieänderung pro Mol reagierendem Sn berechnet. Die Berechnungen zeigten, dass die anfängliche Keimbildung von Ag_4Sn thermodynamisch bevorzugt ist. Bedingt durch den interstitiellen Diffusionsmechanismus ist die hohe Mobilität der Ag Atome in der Sn-Schicht sehr hoch, dadurch wird im Falle der „Sn auf Ag" Doppelschichten die intermetallische Phasenbildung bervorzugt in der Sn Schicht stattfinden. Da Ag praktisch unlöslich in Sn ist, wurde in diesem Fall die Gibbs-Energieänderung bei der Keimbildung der intermetallischen Phasen *pro Mol reagierendem Ag* aus reinem Ag und Sn betrachtet. Die Berechnungen zeigten, dass verglichen mit der Keimbildung von Ag_4Sn, bei der Keimbildung von Ag_3Sn mehr Energie frei wird. Folglich ist im Falle der „Sn auf Ag" Doppelschichten die anfängliche Keimbildung von Ag_3Sn bevorzugt.

Um die Ergebnisse der Ag–Sn Doppelschichten vollständig erklären zu können, mussten kinetische Betrachtungen ebenfalls mit einbezogen werden. Basierend auf einem kinetischen Modell für das Wachstum intermetallischer Phasen in binären Diffusionspaaren, dass bereits in der Literatur vorgeschlagen wurde, konnten die nach dem Abscheiden vorhandenen intermetallischen Phasen in den Ag–Sn Doppelschichten erklärt werden. Im anfänglichen Stadium der Bildung der intermetallischen Phasen bestimmen die Reaktionen an den Grenzflächen der Intermetallikschichten die Wachstumskinetik. In diesem Stadium nimmt das Verhältnis der Flüsse der Ag Atome, r, im Ag–Sn System einen solchen Wert an, dass allein die intermetallische Phase Ag_4Sn beobachtet wird (vergl. Abb. 6.3, zum Zeitpunkt t_0). Die Ag_4Sn-Bildung läuft so schnell ab, dass das Wachstum von Ag_3Sn in diesem Stadium kinetisch unterdrückt wird. Letztendlich bestimmt, mit zunehmender Dicke der wachsenden Ag_4Sn-Schicht, der Diffusionsfluss durch diese Intermetallikschicht die Wachstumskinetik (Zeitpunkt t_1 in Abb. 6.3). Nun nimmt das Verhältnis der Flüsse r ab, was schließlich die Bildung von Ag_3Sn neben Ag_4Sn ermöglicht (Zeitpunkt t_2 in Abb. 6.3). Dieser Sachverhalt beschreibt die „Sn auf Ag" Doppelschichten direkt nach der Abscheidung (vergl. (b) in Abb. 6.3).

Durch die zusätzliche Triebkraft, hervorgerufen durch die unterschiedlichen Oberflächenenergien, ist jedoch der Diffusionsfluss in den „Ag auf Sn" Doppelschichten erhöht. Dadurch bleibt das Wachstum von Ag_4Sn mindestens bis direkt nach der Abscheidung grenzflächenkontrolliert (vergl. (a) in Abb. 6.3). Folglich kann für diese Art der Doppelschichten nur Ag_4Sn beobachtet werden.

Die Texturen der jeweiligen Subschichten hängen ebenfalls von der Stapelsequenz der aufgedampften Ag–Sn Doppelschichten ab. Beim thermischen Verdampfen wird die Keimbildung von Kristalliten mit dichtest gepackten Ebenen parallel zur Oberfläche des Substrats bevorzugt, entsprechend besitzen die Sn und Ag Subschichten jeweils eine {100} und {111} Fasertextur. Durch kohärentes/epitaktisches Wachstum von Ag Kristalliten auf darunterliegenden Sn Kristalliten haben Ag Oberflächenschichten jedoch eine {100} Fasertextur.

Im Gegensatz zu den thermisch aufgedampften Doppelschichten, hängen die intermetallischen Phasen die direkt nach der Abscheidung vorhanden sind, in magnetrongesputterten Doppelschichten nicht von der Stapelsequenz der Subschichten ab (vergl. Kapitel 3). In beiden Stapelsequenzen der Ag–Sn Doppelschichten ist hauptsächlich Ag_3Sn vorhanden. Die Ergebnisse können durch die unterschiedlichen atomaren Prozesse beider Abscheidungsmethoden erklärt werden. Verglichen mit den thermisch verdampften Partikeln besitzen die gesputterten Partikel eine viel höhere kinetische Energie. Im Vergleich zu thermisch aufgedampften Schichten führt dies zur Bildung eines größeren Durchmischungsgebiets in den gesputterten Schichten. Dadurch, dass die erhöhte Durchmischung

schon zu einer reduktion der Oberflächenenergie von Ag führt, ist in gesputterten „Ag auf Sn" Schichten keine zusätzliche Triebkraft für die Sn Diffusion vorhanden. Infolgedessen ist der erhöhte Diffusionsfluss von Sn in die Ag-Schicht in gesputterten „Ag auf Sn" Doppelschichten nicht vorhanden und die makroskopischen Kirkendallporen können nicht entstehen. Weiterhin können die hochenergetischen, gesputterten Partikel Defekte auf der Oberfläche der Sn-Subschicht verursachen, welche als mögliche Keimbildungszentren für die intermetallischen Phasen agieren können. Aufgrund dieser zusätzlichen Keimbildungszentren verringert sich die Keimbildungsbarrriere der geordneten Ag_3Sn Intermetallik. Weiterhin führt Magnetronsputtern zu stapelfehlerfreien Mikrostrukturen, während solche Stapelfehler in thermisch aufgedampften Schichten vorhanden sind und die Bildung der hexagonalen Ag_4Sn Intermetallik bevorzugen. Die Kombination all dieser besprochenen Effekte führt zur bevorzugten Bildung von Ag_3Sn anstatt von Ag_4Sn in magnetrongesputterten „Ag auf Sn" Doppelschichten. Im Gegensatz zu den thermisch aufgedampften Schichten, führt die Erniedrigung der Keimbildungsbarrieren und der dauerhafte Partikelbeschuss der wachsenden Unterschichten zu nur schwach- oder untexturierten magnetrongesputterten Filmen.

In Kapitel 4 wurde die Kinetik der Bildung intermetallischer Phasen im Ag–In System bei Raum- und erhöten Temperaturen untersucht. Wie im Ag–Sn System, hingen im Ag–In System die direkt nach der Abscheidung vorhandenen intermetallischen Phasen von der Stapelsequenz der Subschichten ab. In „In auf Ag" Doppelschichten ist nur $AgIn_2$ vorhanden, während in „Ag auf In" Doppelschichten sowohl $AgIn_2$ als auch Ag_2In vorhanden sind. Die Oberflächenenergien verhalten sich ähnlich wie im Ag–Sn System. Wiederum ist die Oberflächenenergie von In ungefähr halb so groß wie diese von Ag, was eine ähnliche Erklärung wie im Ag–Sn system für diesen Effekt nahelegt.

Für die Untersuchung der Kinetik der intermetallischen Phasenbildung wurden nur „In auf Ag" Doppelschichten benutzt, da das Vorhandensein nur einer einzelenen intermetallischen Phase direkt nach der Abscheidung die kinetische Analyse vereinfacht. Ein zweidimensionaler Röntgendetektor wurde verwendet um eine hohe zeitliche Auflösung zu erreichen, diese war in den bisher veröffentlichten Arbeiten nicht verfügbar. Aus den Röntgenbeugungsdiagrammen wurde ersichtlich, dass zwei unterschiedliche kinetische Wachstumsstadien vorhanden sind, die mit der Präsenz/Absenz der In-Schicht in den Doppelschichten übereinstimmen. Im ersten Wachstumsstadium wächst $AgIn_2$ zwischen der Ag- und der In-Schicht. Im zweiten Wachstumsstadium, das beginnt wenn die In-Schicht komplett reagiert hat, bildet sich Ag_2In und wächst zwischen der Ag- und der $AgIn_2$-Schicht.

Bedingt durch den schnellen interstitiellen Diffusionsmechanismus der Ag Atome in In, findet die Keimbildung der intermetallischen Phasen wahrscheinlich in der In-Schicht statt. Da die In-Schicht praktisch keine Löslichkeit für Ag besitzt, kann die Änderung

der Gibbsenergie bei der Keimbildung der intermetallischen Phase analog zu den „Sn auf Ag" Doppelschichten abgeschätzt werden (siehe oben). Es wurde gezeigt, dass bei der Bildung von $AgIn_2$ mehr Energie *pro Mol reagierendem Ag* frei wird, als bei der Bildung von Ag_2In, was die anfängliche Bildung von $AgIn_2$ bevorzugt. Im zweiten Wachstumsstadium konnte jedoch die Bildung und das Wachstum von Ag_2In beobachtet werden, was darauf hindeutet, dass die Unterdrückung von Ag_2In im ersten Wachstumsstadium einen kinetischen Ursprung hat. Tatsächlich konnte mit demselben kinetischen Modell, das für das Ag–Sn System verwendet wurde, gezeigt werden, dass $AgIn_2$ wahrscheinlich so schnell wächst, dass anfänglich kein Ag_2In beobachtet werden kann. Nur der Abbau der In-Schicht ermöglicht letztendlich die Bildung von Ag_2In im zweiten Wachstumsstadium.

Der Wachstumsmodus von $AgIn_2$ im ersten Wachstumsstadium konnte weder durch eine diffusionskontrollierte Wachstumskinetik, noch durch eine grenzflächenkontrollierte Wachstumskinetik beschrieben werden. Durch einen gemischten Wachstumsmodus, der sowohl Beitrage von den Diffusionsprozessen also auch von den Reaktionen an den Grenzflächen enthält, konnte das Wachstums von $AgIn_2$ adäquat beschrieben werden. In der vorhandenen Literatur wurde jedoch bisher nur diffusionskontrolliertes Wachstum von $AgIn_2$ beschrieben. Von Ag_2In konnten bei Raumtemperatur zwei unterschiedliche Wachstumsmodi beobachtet werden. Der zweite, langsamere Wachstumsmodus der später auftritt und der einzigste Wachstumsmodus ist, der bei erhöhten Temperaturen boebachtet wird, ist zweifelsfrei Diffusionskontrolliert mit einem Diffusionskoeffizienten von $D = 1.1 \pm 3.9 \cdot 10^{-4}\ \mathrm{cm^2\ s^{-1}} \exp(-60.5 \pm 9.2\ \mathrm{kJ\ mol^{-1} R^{-1} T^{-1}})$. Der Erste, schnellere Wachstumsmodus von Ag_2In ist höchstwahrscheinlich wieder ein gemischter Wachstumsmodus.

Die Bildung der intermetallischen Phasen führt zu Zugeigenspannungen in den „In auf Ag" Doppelschichten. Die Zugspannungen entwickeln sich durch die Volumenzunahme die mit der Bildung der intermetallischen Phasen verbunden ist.

Aufgrund der widersprüchlichen Ergebnisse in den bisher veröffentlichten Arbeiten bezüglich des Vorhandenseins einer geordneten Besetzung und des Typs der orthorhombischen Verzerrung (λ-Typ oder ϰ-Typ) in der Kristallstruktur von Ag_3Sn, wurden diese veröffentlichten Kristallstrukturen, mithilfe ihrer Gruppen-Untergruppen Beziehungen, Elementarzellen und orthorhombischer Verzerrung, in Kapitel 5 diskutiert. Zur Ermittlung der korrekten Kristallstruktur von Ag_3Sn, wurden Pulverproben hergestellt und mittels hochauflösender Röntgenpulverdiffraktometrie untersucht. Die Pulverpräparation wurde mit großer Sorgfalt durchgeführt, um für Röntgenpulverdiffraktometrie geignete Pulver ohne Präparationsartefakte zu erhalten. Damit homogenisierte Massivproben im thermodynamischen Gleichgewicht erhalten wurden, war eine ausgedehnte Glühbehandlung nötig. Dies lieferte einen Hinweis darauf, dass einige der widersprüchlichen Ergebnisse in den bisher veröffentlichten Arbeiten durchaus eine Folge einer unzureichenden

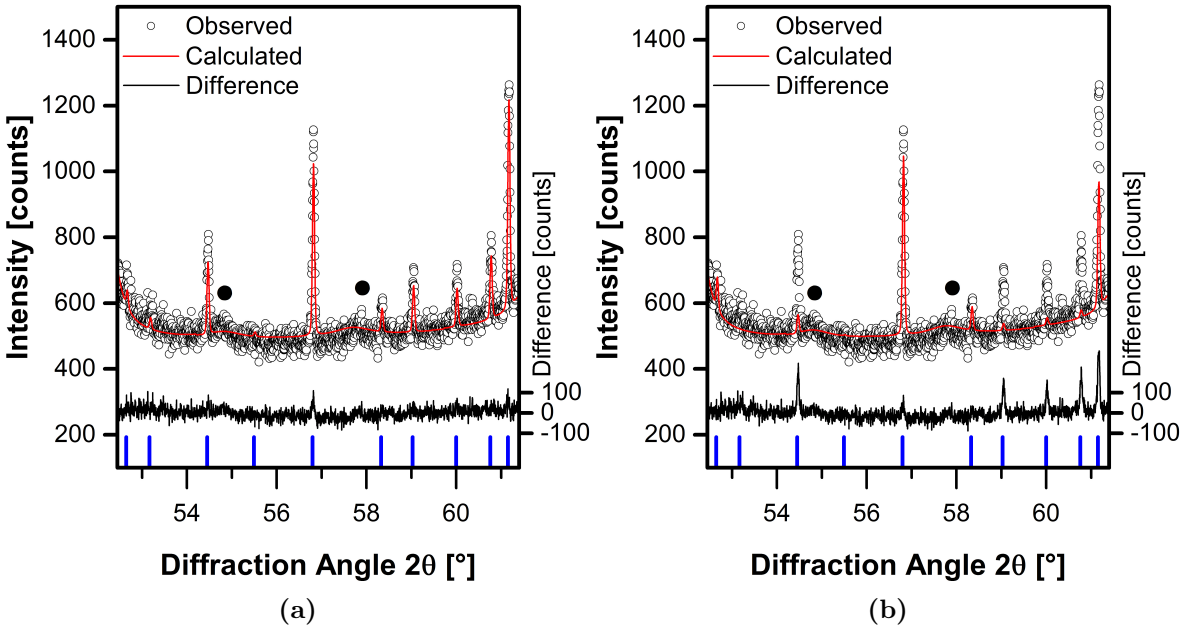

Abbildung 6.4: Vergleich der modellierten Beugungsdiagramme: (a) zeigt eine Modellierung mittels einer geordneten und (b) zeigt eine Modellieren mittels einer ungeordneten Modellstruktur. Es ist klar ersichtlich, dass eine geordnete Modellstruktur notwendig ist, um alle Reflektionen angemessen beschreiben zu können. Das • Symbol weist auf Reflektionen hin die von SnO_2 hervorgerufen werden.

Homogenisierungsbehandlung sein könnten. Einige Ergebenisse zeigen, dass die Zusammensetzung der Ag_3Sn-Pulver durch chemische Behandlung verändert werden konnte. Ein solches Verfahren wurde in einer anderen Arbeit angewendet, um Ag_3Sn-Proben zu erhalten. Dies könnte erklären, warum dort eine von anderen Arbeiten abweichende orthorhombische Verzerrung erhalten wurde.

Um Beugungsdiagramme mit hohem Signal-Rausch Verhältnis zu erhalten, wurden bei den Röntgendiffraktometriemessungen hohe Zählzeiten in Verbindung mit einem eindimensionalen ortsaufgelösten Detektor verwendet. Neben den (gespaltenen) fundamentalen hexagonalen Reflektionen konnten zusätzliche schwache (Überstruktur-)Reflexe in den Beugungsdiagrammen beobachtet werden. Es wurde gezeigt, dass diese zusätzlichen Reflexe im Falle der Ag_3Sn-Intermetallik nicht notwendigerweise durch eine geordnete Besetzung der Wyckofflagen hervorgerufen werden. Das Auftreten der zusätzlichen schwachen Reflexe kann auch durch Abweichungen einzelner Atome von sogenannten „ideal hexagonalen" Positionen hervorgerufen werden. Mittels der Rietveldmethode wurde jedoch zweifelsfrei gezeigt, dass eine geordnete Besetzung der Wyckofflagen nötig ist, um die erhaltenen Beugungsdiagramme angemessen beschreiben zu können (vergl. Abb. 6.4).

Die Ergebnisse der Rietveld-Methode zeigten somit deutlich, dass Ag_3Sn eine geordnete Kristallstruktur des β-Cu_3Ti-Typs (Raumgruppe *Pmmn*) mit orthorhombischer Verzer-

rung des $\varkappa$-Typs hat. Um zu beweisen dass die Art der Verzerrung nicht von der Zusammensetzung abhängt, wurden Proben unterschiedlicher Zusammensetzung gemessen.

Bibliography

[1] P. Shewmon. *Diffusion in Solids*. The Minerals, Metals & Materials Society, Warrendale, 1989.

[2] Ž. Marinković and V. Simić. Kinetics of reaction at room temperature in thin silver-metal couples. *Thin Solid Films*, 195(1-2):127–136, 1991.

[3] H. Mehrer. *Diffusion in Solids*. Springer, Heidelberg, 2007.

[4] C. Matano. On the relation between the diffusion-coefficients and concentrations of solid metals (the nickel-copper system). *Jpn. J. Phys.*, 8:109–113, 1933.

[5] L.S. Darken. Diffusion, mobility and their interrelation through free energy in binary metallic systems. *Trans. Am. Inst. Min. Metal. Eng.*, 175:184–201, 1948.

[6] A.D. Smigelskas and E.O. Kirkendall. Zinc diffusion in alpha-brass. *Trans. Am. Inst. Min. Metal. Eng.*, 171:130–142, 1947.

[7] W.F. Gale and F.C. Totemeier. *Smithells Metals Reference Book*. Elsevier Butterworth Heinemann, Oxford, 2004.

[8] Milton Ohring. *Materials Science of Thin Films*. Academic Press, Burlington, 2002. ISBN 978-0-12-524975-1.

[9] C. V. Thompson. Secondary grain growth in thin films of semiconductors: Theoretical aspects. *J. Appl. Phys.*, 58:763–772, 1985.

[10] L.B. Freund. Stability of a dislocation threading a strained layer on a substrate. *J. App. Mech.-T. ASME*, 54:553–557, 1987.

[11] W.D. Nix. Mechanical properties of thin films. *Metal. Trans. A*, 20:2217–2245, 1989.

[12] C.J. Kircher. Metallurgical properties and electrical characteristics of palladium silicide-silicon contacts. *Solid State Electron.*, 14:507–513, 1971.

[13] E.J. Mittemeijer. *Fundamentals of Materials Science*, chapter 8, pages 339–368. Springer, Heidelberg, 2010.

[14] K.N. Tu. Interdiffusion in thin films. *Annu. Rev. Mater. Res.*, 15:147–176, 1987.

[15] W. K. Warburton and D. Turnbull. "Fast" diffusion in alloys. *Thin Solid Films*, 25:71–76, 1975.

[16] V. Simić and Ž. Marinković. Room-temperature reactions in thin metal couples. *J. Mater. Sci.*, 33:561–624, 1998.

[17] S. Nakahara and R.J. McCoy. Kirkendall void formation in thin-film diffusion couples. *Appl. Phys. Lett.*, 37(1):42–44, 1980.

[18] S. Nakahara, R.J. McCoy, L. Buene, and J.M. Vandenberg. Room temperature interdiffusion studies of Au/Sn thin film couples. *Thin Solid Films*, 84:185–196, 1981.

[19] D. Gregersen, L. Buene, T. Finstad, O. Lønsjø, and T. Olsen. A diffusion marker in Au/Sn thin films. *Thin Solid Films*, 78:95–102, 1981.

[20] V. Simić and Ž. Marinković. Thin film interdiffusion of Au and Sn at room temperature. *J. Less.-Common Met.*, 51(1):177–179, 1977.

[21] N.-C. Lee. Lead-free soldering - where the world is going. *Adv. Microelectron.*, 26: 29–35, 1999.

[22] Y.M. Liu and T.H. Chuang. Interfacial reactions between $In_{10}Ag$ solders and Ag substrates. *J. Electron. Mater.*, 29:1328–1332, 2000.

[23] V. Simić and Ž. Marinković. Room temperature interactions in Ag-metals thin film couples. *Thin Solid Films*, 61:149–160, 1979.

[24] S. K. Sen, A. Ghorai, A. K. Bandyopadhyay, and S. Sen. Interfacial reactions in bimetallic Ag-Sn thin film couples. *Thin Solid Films*, 155:243–253, 1987.

[25] R. Roy and S.K. Sen. The kinetics of formation of intermetallics in Ag/In thin film couples. *Thin Solid Films*, 197:303–318, 1991.

[26] W. Keppner, R. Wesche, J. Klas, and G. Schatz. Studies of compound formation at Cu-In, Ag-In and Au-In interfaces with perturbed γ-γ angular correlactions. *Thin Solid Films*, 143:201–215, 1986.

[27] P. Wodniecki, B. Wodniecka, M. Marszalek, Z. Mazgaj, and B. Kubica. The Ag-In intermetallic compound formation from Ag and In electrodeposited layers observed by PAC. *Hyperfine Interact.*, 60:841–844, 1990.

[28] B. Wodniecka, P. Wodniecki, and A.Z. Hrynkiewicz. PAC studies of AgIn2 and Ag2In growth kinetics at the Ag-In interface. *Hyperfine Interact.*, 78:323–326, 1993.

[29] European Commission. Directive 2002/95/EC of the European Parliament and of the Council of 27 January 2003 on the restriction of the use of certain hazardous substances in electrical and electronic equipment. *Off. J. Eur. Union*, L37:19–23, 2003.

[30] J. Stein, S. Rehm, U. Welzel, W. Huegel, and E.J. Mittemeijer. The role of silver in mitigation of whisker formation on thin tin films. *J. Electron. Mater.*, 43:4308–4316, 2014.

[31] K Suganuma. Advances in lead-free electronics soldering. *Curr. Opin. Solid State Mater. Sci.*, 5:55 – 64, 2001.

[32] S. Sommadossi, W. Gust, and E.J. Mittemeijer. Characterization of the reaction process in diffusion-soldered Cu/In-48 at.% Sn/Cu joints. *Mater. Chem. Phys.*, 77: 924–929, 2003.

[33] S. Sommadossi, W. Gust, and E.J. Mittemeijer. Phase characterisation and kinetic behaviour of diffusion soldered Cu/In/Cu interconnections. *Mater. Sci. Technol.*, 19:528–534, 2003.

[34] W.R. Osório, L.C. Peixoto, L.R. Garcia, N. Mangelinck-Noël, and A. Garcia. Microstructure and mechanical properties of Sn-Bi, Sn-Ag and Sn-Zn lead-free solder alloys. *J. Alloys Compd.*, 572:97–106, 2013.

[35] T.-M. Korhonen and J.K. Kivilahti. Thermodynamics of the Sn-In-Ag solder system. *J. Electron. Mater.*, 27:149–158, 1998.

[36] K. Kanlayasiri, M. Mongkolwongrojn, and T. Ariga. Influence of indium addition on characteristics of Sn-0.3Ag-0.7Cu solder alloy. *J. Alloys Compd.*, 485:225–230, 2009.

[37] H.L. Reynolds, S.H. Rang, and J.W. Morris Jr. The creep behavior of In-Ag eutectic solder joints. *J. Electron. Mater.*, 28:69–75, 1999.

[38] A.N. Campbell, R. Wagemann, and R.B. Ferguson. The silver-indium system: thermal analysis, photomicrography, electron microprobe, and X-ray powder diffraction results. *Can. J. Chem.*, 48:1703–1715, 1970.

[39] D.W. Henderson, T. Gosselin, A. Sarkhel, S.K. Kang, W.-K. Choi, D.-Y. Shih, C. Goldsmith, and K.J. Puttlitz. Ag_3Sn plate formation in the solidification of near ternary eutectic Sn-Ag-Cu alloys. *J. Mater. Res.*, 17:2775–2778, 2002.

[40] J.O.G. Parent, D.D.L. Chung, and I.M. Bernstein. Effects of intermetallic formation at the interface between copper and lead-tin solder. *J. Mater. Sci.*, 23:2564–2572, 1988.

[41] P.L. Tu, Y.C. Chan, and J.K.L. Lai. Effect of intermetallic compounds on the thermal fatigue of surface mount solder joints. *IEEE Trans. Compon. Packag. Manuf. Technol. Part B*, 20:87–93, 1997.

[42] S.-H. Kim, J.-Y. Kim, J. Yu, and T.Y. Lee. Residual stress and interfacial reaction of the electroplated Ni-Cu alloy under bump metallurgy in the flip-chip solder joint. *J. Electron. Mater.*, 33:948–957, 2004.

[43] R.W. Chuang and C.C. Lee. Silver-indium joints produced at low temperature for high temperature devices. *IEEE T. Compon. Pack. T.*, 25:453–458, 2002.

[44] P.J. Wang, C.-H. Sha, and C.C. Lee. Effect of Ag grain size on high temperature joint formation in Ag-In system. In *Proceedings - Electronic Components and Technology Conference*, pages 781–788, 2010.

[45] K.S. Kim, S.H. Huh, and K. Suganuma. Effects of intermetallic compounds on properties of Sn-Ag-Cu lead-free soldered joints. *J. Alloys Compd.*, 352:226–236, 2003.

[46] N. Mookam and K. Kanlayasiri. Effect of soldering condition on formation of intermetallic phases developed between Sn-0.3Ag-0.7Cu low-silver lead-free solder and Cu substrate. *J. Alloys Compd.*, 509:6276–6279, 2011.

[47] W. Hume-Rothery. *The Structure of Metals and Alloys*. The Metals and Metallurgy Trust of the Insitute of Metals and the Institutin of Metallurgists, London, 1962.

[48] T.B. Massalski and U. Mizutani. Electronic structure of Hume-Rothery phases. *Prog. Mater. Sci.*, 22:151–262, 1978.

[49] G.V. Raynor and T.B. Massalski. The lattice spacings of close-packed hexagonal 3 2 electron compounds. *Acta Metal.*, 3:480–486, 1955.

[50] T.B. Massalski and H.W. King. The lattice spacing relationships in H.C.P. ϵ and η phases in the systems Cu-Zn, Ag-Zn; Au-Zn and Ag-Cd. *Acta Metal.*, 10:1171–1181, 1962.

[51] H. W. King and T. B. Massalski. Lattice spacing relationships and the electronic structure of H.C.P. ζ phases based on silver. *Philos. Mag.*, 6:669–682, 1961.

[52] I. Karakaya and W. T. Thompson. The Ag-Sn (silver-tin) system. *Bull. Alloy Ph. Diagr.*, 8:340–347, 1987.

[53] G.J. Petrenko. Über die Legierungen des Silbers mit Blei und Zinn. *Z. Anorg. Chem.*, 53:200–211, 1907.

[54] A.J. Murphy. Constitution of the alloys of silver and tin. *J. Inst. Met.*, 35:107–129, 1926.

[55] G.D. Preston. Constitution of the alloys of silver and tin. *J. Inst. Met.*, 35:118, 1926.

[56] O Nial, A Almin, and A Westgren. Röntgenanalyse der Systeme Gold-Antimon und Silber-Zinn. *Z. Phys. Chem. B-Chem. E.*, 14:81–90, 1931.

[57] W. Burkhardt and K. Schubert. Über messingartige Phasen mit A3-verwandter Struktur. *Z. Metallkd.*, 50:442–452, 1959.

[58] C. W. Fairhurst and J. B. Cohen. The crystal structures of two compounds found in dental amalgam: Ag_2Hg_3 and Ag_3Sn. *Acta Crystallogr. Sect. B: Struct. Sci.*, 28: 371–378, 1972.

[59] C.H. MacGillavry and D. Rieck, editors. *International Tables for X-Ray Crystallography Volume III*. Kynoch Press, Birmingham, 1968.

[60] M. Ellner and E. J. Mittemeijer. In situ and ex situ investigation of the displacive phase transformations $Ag_3Sn(h) \rightarrow Ag_3Sn(l)$ and $Ag_3Sb(h) \rightarrow Ag_3Sb(l)$. *Z. Kristallogr.*, 218:675–682, 2003.

[61] E. Rönnebro, J. Yin, A. Kitano, M. Wada, and T. Sakai. Comparative studies of mechanical and electrochemical lithiation of intermetallic nanocomposite alloys for anode materials in Li-ion batteries. *Solid State Ionics*, 176:2749–2757, 2005.

[62] A. Nylandsted Larsen and G. Weyer. Mössbauer spectroscopy of isotope separator implanted ^{119}Sn in fcc metals. *J. Phys. F: Met. Phys.*, 9:27–37, 1979.

[63] F. Weibke and H. Eggers. Das Zustandsdiagramm des Systems Silber-Indium. *Z. Anorg. Allg. Chem.*, 222:145–160, 1935.

[64] V.M. Goldschmidt. On distances between atoms in metals. *Z. Phys. Chem.-Stoch. Ve.*, 133:397–419, 1928.

[65] E. Hellner and F. Laves. Kristallchemie des In und Ga in Legierungen mit einigen Übergangselementen (Ni, Pd, Pt, Cu, Ag und Au). *Z. Naturforsch. A, Astrophys., Phys., phys. Chem.*, 2:177–183, 1947.

[66] E. Hellner. Das Zweistoffsystem silber-indium. *Z. Metallkd.*, 42:17–19, 1951.

[67] O. Uemura and T. Satow. Order-Disorder Transition of Ag_3In. *T. Jpn. I. Met.*, 14: 199–201, 1973.

[68] T. Satow, O. Uemura, and S. Yamakawa. X-Ray Diffraction and Electrical Resistivity Study of Ag_2In and High Temperature Ag_3In Phases. *T. Jpn. I. Met.*, 15: 253–255, 1974.

[69] B. Predel. Numerical data and functional relationships in science and technology. In O. Madelung, editor, *Group IV Physical Chemistry*, volume 5 Phase Equilibria, Crystallographic and Thermodynamic Data of Binary Alloys, chapter Ag-In (Silver-Indium). Landold-Börnstein, Heidelberg, 1991.

[70] E.A. Owen and E.W Roberts. Factors affecting the limit of solubility of elements in copper and silver. *Philos. Mag.*, 27:294–327, 1939.

[71] T.R. Anthony and D. Turnbull. Interstitial diffusion of gold and silver in indium. *Phys. Rev.*, 151:495–498, 1966.

[72] C.T. Tomizuka and L. Slifkin. Diffusion of cadmium, indium, and tin in single crystals of silver. *Phys. Rev.*, 96:610–615, 1954.

[73] M. Hansen and K. Anderko. *Constitution of Binary Alloys*. McGraw-Hill, New York, 1958.

[74] E.J. Mittemeijer. *Fundamentals of Materials Science*, chapter 9, pages 371–461. Springer, Heidelberg, 2010.

[75] J Philibert. Interplay of diffusion and interface processes in multiphase diffusion. *Defect Diffus. Forum*, 95-98:493–506, 1993.

[76] U. Gösele and K. N. Tu. Growth kinetics of planar binary diffusion couples: "Thin-film case" versus "bulk cases". *J. Appl. Phys.*, 53:3252–3260, 1982.

[77] R.M. Walser and R.W. Bené. First phase nucleation in silicon-transition-metal planar interfaces. *Appl. Phys. Lett.*, 28:624–625, 1976.

[78] R.W. Bené. First nucleation rule for solid-state nucleation in metal-metal thin-film systems. *Appl. Phys. Lett.*, 41:529–531, 1982.

[79] R. Pretorius, T.K. Marais, and C.C. Theron. Thin film compound phase formation sequence: An effective heat of formation model. *Mater. Sci. Rep.*, 10:1–83, 1993.

[80] Y.Y. Geguzin, Y.S. Kaganovskiy, L.M. Paritskaya, and V.I. Solunskiy. Kinetics of the motion of the interface during mutual diffusion in a two-component system. *Phys. Met. Metallogr.*, 47:127–138, 1979.

[81] J.M. Poate and K.N. Tu, editors. *Thin Films, Interdiffusion and Reactions*, chapter 10, pages 359–406. Wiley-Interscience, New York, 1978.

[82] G. Ottaviani. Review of binary alloy formation by thin film interactions. *J. Vac. Sci. Technol.*, 16:1112–1119, 1979.

[83] B. Gollas, J. H. Albering, K. Schmut, V. Pointner, R. Herber, and J. Etzkorn. Thin layer in situ XRD of electrodeposited Ag/Sn and Ag/In for low-temperature isothermal diffusion soldering. *Intermetallics*, 16:962–968, 2008.

[84] C. Wagner. The evaluation of data obtained with diffusion couples of binary single-phase and multiphase systems. *Acta Metal.*, 17:99–107, 1969.

[85] J.A. Thornton. Influence of substrate temperature and deposition rate on structure of thick sputtered Cu coatings. *J. Vac. Sci. Technol.*, 12:830–835, 1975.

[86] B.A. Movchan and A.V. Demchishin. Study of structure and properties of thick vacuum condensates of nickel, titanium, tungsten, aluminium oxide and zirconium dioxide. *Phys. Met. Metallogr.*, 28:83–90, 1969.

[87] John A. Thornton. Influence of apparatus geometry and deposition conditions on the structure and topography of thick sputtered coatings. *J. Vac. Sci. Technol.*, 11:666–670, 1974.

[88] H.T.G Hentzell, C.R.M. Grovenor, and D.A. Smith. Grain structure variation with temperature for evaporated metal films. *J. Vac. Sci. Technol. A: Vac., Surf., Films*, 2:218–219, 1984.

[89] E. Lugscheider, C. Barimani, C. Wolff, S. Guerreiro, and G. Doepper. Comparison of the structure of PVD-thin films deposited with different deposition energies. *Surf. Coat. Technol.*, 86-87:177–183, 1996.

[90] Y. Golan, L. Margulis, and I. Rubinstein. Vacuum-deposited gold films. I. Factors affecting the film morphology. *Surf. Sci.*, 264:312–326, 1992.

[91] S. Blackwell, R. Smith, S.D. Kenny, and J.M. Walls. Modeling evaporation, ion-beam assist, and magnetron sputtering of thin metal films over realistic time scales. *Phys. Rev. B: Condens. Matter Mater. Phy.*, 86:035416–1–035416–12, 2012.

[92] K.L. Chopra. Growth of sputtered vs evaporated metal films. *J. Appl. Phys.*, 37: 3405–3410, 1966.

[93] L.I. Maissel and R. Glang. *Handbook of Thin Film Technology.* McGraw-Hill, New York, 1970.

[94] D.A. Glocker and S. Ismat Shah. *Handbook of Thin Film Process Technology.* Institute of Physics Publishing, Boca Raton, 1998.

[95] C.V. Thompson and R. Carel. Stress and grain growth in thin films. *J. Mech. Phys. Solids*, 44:657–673, 1996.

[96] L. Dong and J. Srolovitz. Study on texture evolution and properties of silver thin films prepared by sputtering deposition. *J. Appl. Phys.*, 84:5261–5269, 1998.

[97] M.B. Stearns, C.H. Lee, C.-H. Chang, and A.K. Petford-Long. Magnetic, X-ray and TEM studies of several multilayer systems. In *Metallic Multi-Layers and Epitaxy. Proceedings of a Symposium*, pages 55–75, 1988.

[98] C. L. Bauer and A. G. Jordan. Study of Interfacial Reactions in Bimetallic Thin-Film Couples by Contact Resistance Measurements. *Phys. Stat. Sol. (A)*, 47:321–328, 1978.

[99] S. Bader, W. Gust, and H. Hieber. Rapid formation of intermetallic compounds interdiffusion in the CuSn and NiSn systems. *Acta Metall. Mater.*, 43(1):329–337, 1995.

[100] E.J. Mittemeijer and U. Welzel, editors. *Modern Diffraction Methods.* Wiley-VCH, Weinheim, 2012.

[101] R. A. Young. *The Rietveld Method.* Oxford University Press, Oxford, 1995.

[102] K. Levenberg. A method for the solution of certain problems in least squares. *Q. Appl. Math.*, 2:164–168, 1944.

[103] W. Marquardt. An algorithm for leat-squares estimation of nonlinear parameters. *J. Soc. Ind. Appl. Math.*, 11:431–441, 1963.

[104] L.A. Giannuzzi and F.A. Stevie, editors. *Introduction to Focused Ion Beams.* Springer Science & Business Media, New York, 2005.

[105] B. F. Dyson. Diffusion of gold and silver in tin single crystals. *J. Appl. Phys.*, 37: 2375–2377, 1966.

[106] W. Tang, A. He, Q. Liu, and D.G. Ivey. Room temperature interfacial reactions in electrodeposited Au/Sn couples. *Acta Mater.*, 56:5818–5827, 2008.

[107] K.A. Reinhardt and W. Kern, editors. *Handbook of Silicon Wafer Cleaning Technology (Materials Science and Process Technology).* Willian Andrew Inc., Norwich, 2007.

[108] P.J. Rossi, N. Zotov, and E.J. Mittemeijer. Redetermination of the crystal structure of Ag_3Sn. *Z. Kristallogr.*, 231:1–9, 2015.

[109] A.W. Ruff Jr. and L.K. Ives. Dislocation node determinations of the stacking fault energy in silver-tin alloys. *Acta Metal.*, 15:189–198, 1967.

[110] R.P.I. Adler and C.N.J. Wagner. X-Ray diffraction study of the effects of solutes on the occurrence of stacking faults in silver-base alloys. *J. Appl. Phys.*, 33:3451–3458, 1962.

[111] J.P. Hirth and J. Lothe. *Theory of Dislocations.* Wiley, New York, 1982.

[112] G. Gottstein. *Physical Foundations of Materials Science.* Springer, Heidelberg, 2004.

[113] J. Greiser, P. Müllner, and E. Arzt. Abnormal growth of "giant" grains in silver thin films. *Acta Mater.*, 49:1041–1050, 2001.

[114] J. Yu and J.Y. Kim. Effects of residual S on Kirkendall void formation at Cu/Sn-3.5Ag solder joints. *Acta Mater.*, 56:5514–5523, 2008.

[115] F.R. de Boer, R. Boom, and W.C.M. Mattens. *Cohesion in Metals.* North-Holland, Amsterdam, 1988.

[116] L. Vitos, A.V. Ruban, H.L. Skriver, and J. Kollár. The surface energy of metals. *Surf. Sci.*, 411:186–202, 1998.

[117] T.C. Frank and J.L. Falconer. Surface compositions of copper-silicon alloys. *Appl. Surf. Sci.*, 14:359–374, 1983.

[118] A. Cros, M.O. Aboelfotoh, and K.N. Tu. Formation, oxidation, electronic, and electrical properties of copper silicides. *J. Appl. Phys.*, 67:3328–3336, 1990.

[119] M. Ibrahim, Z. Balogh, P. Stender, R. Schlesiger, G.-H. Greiwe, G. Schmitz, B. Parditka, G.A. Langer, A. Csik, and Z. Erdélyi. On the influence of the stacking sequence in the nucleation of Cu_3Si: Experiment and the testing of nucleation models. *Acta Mater.*, 76:306–313, 2014.

[120] C. Largeron, E. Quesnel, and J. Thibault. Interface growth mechanism in ion beam sputtering-deposited Mo/Si multilayers. *Philos. Mag.*, 86:2865–2879, 2006.

[121] P.J. Rossi, N. Zotov, and E.J. Mittemeijer. 9th European Conference on Residual Stresses (ECRS-9). In *Abstract book*, page 41, Troyes, France, 2014.

[122] H. Flandorfer, U. Saeed, C. Luef, A. Sabbar, and H. Ipser. Interfaces in lead-free solder alloys: Enthalpy of formation of binary Ag-Sn, Cu-Sn and Ni-Sn intermetallic compounds. *Thermochim. Acta*, 459:34–39, 2007.

[123] O.J. Kleppa. A calorimetric investigation of the system silver-tin at 450° C. *Acta Metal.*, 3:255–259, 1955.

[124] R. Pretorius, C.C. Theron, A. Vantomme, and J.W. Mayer. Compound phase formation in thin film structures. *Crit. Rev. Solid State Mater. Sci.*, 24:1–62, 1999.

[125] K.J. Puttlitz and K.A. Stalter. *Handbook of Lead-Free Solder Technology for Microelectronic Assemblies*, chapter 1, pages 20–23. Marcel Dekker Inc, Boca Raton, 2004.

[126] Y. Lu, N. Zhang, L. An, X. Li, and D. Xia. Synthesis of high dispersed intermetallic Ag_4Sn/C and its enhanced oxygen reduction reaction activity. *J. Power Sources*, 240:606–611, 2013.

[127] S.L. Zhu, L. Tang, Z.D. Cui, Wei Q., and X.J. Yang. Preparation of copper-coated β-SiC nanoparticles by electroless plating. *Surf. Coat. Technol.*, 205:2985–2988, 2011.

[128] Y.H. Jo, I. Jung, N.R. Kim, and H.M. Lee. Synthesis and characterization of highly conductive Sn–Ag bimetallic nanoparticles for printed electronics. *J. Nanopart. Res.*, 14:1–10, 2012.

[129] T.B. Massalski, H. Okamoto, P.R. Subramanian, and L. Kacprzak, editors. *Binary Alloy Phase Diagrams*. ASM International, Ohio, 1990.

[130] P.T. Vianco, J.J. Martin, R.D. Wright, and P.F. Hlava. Solid-state interface reactions between silver and 95.5Sn–3.9Ag–0.6Cu and 63Sn–37Pb solders. *Metall. Mater. Trans. A*, 38:2488–2502, 2007.

[131] B. Horváth, B. Illés, and T. Shinohara. Growth of intermetallics between Sn/Ni/Cu, Sn/Ag/Cu and Sn/Cu layered structures. *Thin Solid Films*, 556:345–353, 2014.

[132] A. Lis, M.S. Park, R. Arroyave, and C. Leinenbach. Early stage growth characteristics of Ag_3Sn intermetallic compoundsduring solid-solid and solid-liquid reactions in the Ag–Sn interlayer system: Experiments and simulations. *J. Alloys Compd.*, 617:763–773, 2014.

[133] Y. He, X. Gao, Y. Zhang, and H. Xu. Electrodeposition of Sn–Ag–Cu ternary alloy from HEDTA electrolytes. *Surf. Coat. Technol.*, 206:4310–4315, 2012.

[134] A.A. Wronkowska, A. Wronkowski, K. ński, M. Senski, and Ł. Skowroński. Spectroscopic ellipsometry study of the dielectric response of Au–In and Ag–Sn thin-film couples. *Appl. Surf. Sci.*, 256:4839–4844, 2010.

[135] E.J. Mittemeijer and U. Welzel, editors. *Modern Diffraction Methods*, chapter 12, pages 391–392. Wiley-VCH, Weinheim, 2012.

[136] S. Mahieu, P. Ghekiere, D. Depla, and R. De Gryse. Biaxial alignment in sputter deposited thin films. *Thin Solid Films*, 515:1229–1249, 2006.

[137] D. Flötotto, Z.M. Wang, L.P.H. Jeurgens, E. Bischoff, and E.J. Mittemeijer. Effect of adatom surface diffusivity on microstructure and intrinsic stress evolutions during Ag film growth. *J. Appl. Phys.*, 112:043503–043508, 2012.

[138] P.C.J. Gallagher. The influence of alloying, temperature, and related effects on the stacking fault energy. *Metall. Trans.*, 1:2429–2461, 1970.

[139] G.B. Olson and M. Cohen. A general mechanism of martensitic nucleation: Part I. General concepts and the FCC $\rightarrow$ HCP transformation. *Metal. Trans. A*, 7: 1897–1904, 1976.

[140] M.J. Madou. *Fundamentals of Microfabrication and Nanofabrication, Vol. II. Manufacturing Techniques for Microfabrication and Nanofabrication.* CRC Press, Boca Raton, 2011.

[141] C.B. Alcock, V.P. Itkin, and M.K. Horrigan. Vapour pressure equations for the metallic elements: 298-2500 K. *Can. Metall. Q.*, 23:309–313, 1984.

[142] R. Fowler and E.A. Guggenheim. *Statistical Thermodynamics.* Cambridge University Press, Cambridge, 1965.

[143] G.M. Turner, I.S. Falconer, B.W. James, and D.R. McKenzie. Monte carlo calculations of the properties of sputtered atoms at a substrate surface in a magnetron discharge. *J. Vac. Sci. Technol. A: Vac., Surf., Films*, 10:455–461, 1992.

[144] M.S. Sellers, A.J. Schultz, C. Basaran, and D.A. Kofke. Atomistic modeling of β-Sn surface energies and adatom diffusivity. *Appl. Surf. Sci.*, 256:4402–4407, 2010.

[145] K.N. Tu. Interdiffusion in thin films. *Annu. Rev. Mater. Sci.*, 15:147–176, 1985.

[146] L. Karpenkopf, Frage N., A. Ripp, N. Froumin, and M.P. Dariel. Sealing technique for wafer-level integrated cavity using In-Ag multilayers. In *Progress in Biomedical Optics and Imaging - Proceedings of SPIE*, pages 63–69, 2005.

[147] P.J. Rossi, N Zotov, E. Bischoff, and E.J. Mittemeijer. Dependence of intermetallic compound formation on the sublayer stacking sequence in Ag–Sn bilayer thin films. *Acta Mater.*, 103:174–183, 2016.

[148] J. Stein, U. Welzel, W. Huegel, S. Blatt, and E.J. Mittemeijer. Aging-time-resolved in situ microstructural investigation of tin films electroplated on copper substrates, applying two-dimensional-detector X-ray diffraction. *J. Appl. Crystallogr.*, 46:1645–1653, 2013.

[149] U. Welzel, J. Ligot, P. Lamparter, A. C. Vermeulen, and E. J. Mittemeijer. Stress analysis of polycrystalline thin films and surface regions by X-ray diffraction. *J. Appl. Crystallogr.*, 38:1–29, 2005.

[150] E.E. Havinga, H. Damsma, and P. Hokkeling. Compounds and pseudo-binary alloys with the CuAl2(C16)-type structure I. Preparation and X-ray results. *J. Less.-Common Met.*, 27:169–186, 1972.

[151] F. Sauer and V. Freise. Diffusion in Binären Gemischen mit Volumenänderung. *Z. Elektrochem.*, 66(4):353–362, 1962.

[152] M.E. Straumanis and S.M. Riad. Solubility limit of indium in silver and thermal-expansion coefficients of the solid solutions. *T. Metall. Soc. AIME*, 233:964–967, 1965.

[153] R. Wesche, R. Fink, G. Krausch, R. Platzer, J. Voigt, U. Wöhrmann, and G. Schatz. Investigations of Ag(100)–In and Ag(111)–In interfaces with local probes. *Thin Solid Films*, 190:153 – 162, 1990.

[154] P. Villars and K. Girgis. Die Zustandsbilder Nb-In, Nb-Tl, Ta-In und Ta-Tl. *Z. Metallkd.*, 73:169–171, 1982.

[155] M. Ellner, K. Kolatschek, and B. Predel. On the partial atomic volume and the partial molar enthalpy of aluminium in some phases with cu and Cu_3Au structures. *J. Less.-Common Met.*, 170:171 – 184, 1991.

[156] W Hume-Rothery. Constitution of the alloys of silver and tin. *J. Inst. Met.*, 35: 127–128, 1926.

[157] P. Thompson, D. E. Cox, and J. B. Hastings. Rietveld refinement of Debye-Scherrer synchrotron X-ray data from Al_2O_3. *J. Appl. Crystallogr.*, 20:79–83, 1987.

[158] R.A. Young and P Desai. Crystallite size and microstrain indicators in Rietveld refinement. *Arch. Nauki Mater.*, 10:71–90, 1989.

[159] M. Järvinen. Application of symmetrized harmonics expansion to correction of the preferred orientation effect. *J. Appl. Crystallogr.*, 26:525–531, 1993.

[160] W. Pitschke, N. Mattern, and H. Hermann. Incorporation of microabsorption corrections in rietveld analysis. *Powder Diffr.*, 8:22–228, 1993.

[161] H Wondratschek and U Müller, editors. *International tables for crystallography*, volume A1: Symmetry relations between space groups. Wiley-Blackwell, Oxford, 2011.

[162] L Vegard. Results of crystal analysis. *Philos. Mag.*, 32:65–69, 1916.

[163] J.B. Nelson and D.P. Riley. An experimental investigation of extrapolation methods in the derivation of accurate unit-cell dimensions of crystals. *P. Phys. Soc.*, 57:160, 1945.

List of Publications

1. P.J. Rossi, N. Zotov, E. Bischoff and E.J. Mittemeijer. Dependence of Intermetallic Compound Formation on the Sublayer Stacking Sequence in Ag–Sn Bilayer Thin Films. *Acta. Mater.,* 103:174–183, 2016, Chapter 2 of this thesis. The final publication is available at www.sciencedirect.com (DOI: 10.1016/j.actamat.2015.09.042).

2. P.J. Rossi, N. Zotov and E.J. Mittemeijer. Effects of deposition method on the microstructure and intermetallic compound formation in Ag–Sn bilayers. *Surf. Coat. Tech.,* 295:88–92, 2016, Chapter 3 of this thesis. The final publication is available at www.sciencedirect.com (DOI: 10.1016/j.surfcoat.2015.10.057).

3. P.J. Rossi, N. Zotov and E.J. Mittemeijer. Kinetics of Intermetallic Compound Formation in Thermally Evaporated Ag–In Bilayers. *J. Appl. Phys.,* 120:165308-1–165308-16, 2016, Chapter 4 of this thesis. The final publication is available at www.aip.com (DOI: 10.1063/1.4966593).

4. P.J. Rossi, N. Zotov and E.J. Mittemeijer. Redetermination of the Crystal Structure of the Ag_3Sn Intermetallic Compound. *Z. Kristallogr.,* 231:1–9, 2016, Chapter 5 of this thesis. The final publication is available at www.degruyter.com (DOI: 10.1515/zkri-2015-1867).

Danksagung

Die vorliegende Arbeit entstand am Max-Planck Institut für Intelligente Systeme (ehemals Max-Planck Institut für Metallforschung), Stuttgart, und dem Institut für Materialwissenschaft der Universität Stuttgart. An dieser Stelle möchte ich mich bei allen bedanken, die zum Gelingen dieser Arbeit beigetragen haben.

Ganz besonders möchte ich meinem Doktorvater, Prof. Dr. Ir. E. J. Mittemeijer, für die Möglichkeit diese Arbeit in seiner Abteilung anfertigen zu dürfen und das mir entgegengebrachte Vertrauen danken. Erst sein außergewöhnliches Engagement und die regelmäßigen wissenschaftlichen Diskussionen, machten ein erfolgreiches Gelingen dieser Arbeit möglich. Sein Enthusiasmus und seine wissenschaftliche Begeisterung ermutigten mich stets bei der Lösung wissenschaftlicher Probleme. Die große Freiheit bei der Gestaltung dieser Arbeit schätze ich sehr.

Prof. Dr. J. Bill danke ich für die freundliche Übernahme des Mitberichts und Prof. Dr. Th. Schleid danke ich ebenfalls für die freundliche Bereitschaft den Prüfungsvorsitz zu übernehmen.

Darüber hinaus möchte ich mich bei meinem täglichen Betreuer, Dr. N. Zotov, für seine kontinuierliche Unterstützung und sein großes Interesse an dieser Arbeit bedanken. Seine stete Diskussions- und Hilfsbereitschaft trugen maßgeblich zum Gelingen dieser Arbeit bei.

Dr. E. Bischoff danke ich für die Durchführung und Diskussion der TEM Messungen. Weiterhin möchte ich U. Eigenthaler, G. Hörner, Dipl.-Ing. G. Maier und R. Völker für ihre experimentelle Unterstützung danken, sowie Prof. Dr. A. Leineweber für die hilfreichen wissenschaftlichen Diskussionen.

Mein Dank gilt auch allen Kollegen des Max-Planck Instituts für Intelligente Systeme und des Instituts für Materialwissenschaft der Universität Stuttgart, sowie insbesondere den Kollegen aus der Abteilung Mittemeijer, für ihre Unterstützung und die angenehme Arbeitsatmosphäre.

Schließlich möchte ich noch meiner Familie, Mireia und meinen Freunden für ihre Unterstützung danken.

Curriculum Vitae

Persönliche Angaben

Name	Paul Rossi
geboren am	31.08.1983 in Heidelberg

Schulbildung

1990–1994	Grundschule, Massenbachhausen
1994–2003	Gymnasium Eppingen, mit dem Abschluss der allgemeinen Hochschulreife

Hochschulbildung

2007–2012	Studium der Werkstoffwissenschaft an der Universität Stuttgart mit dem Abschluss Diplom-Ingenieur. Diplomarbeit über das Thema "Nitriding of Fe–Cr–Si alloys" bei Prof. Dr. Ir. E. J. Mittemeijer am Institut für Materialwissenschaft der Universität Stuttgart

Promotion

2012–2016	Promotion am Max-Planck-Institut fr Intelligente Systeme Stuttgart, und Institut für Materialwissenschaft der Universität Stuttgart, Thema der Dissertation: "Microstructural Changes and Intermetallic Compound Formation in Metallic Bilayers" in der Abteilung von Prof. Dr. Ir. E. J. Mittemeijer

Erklärung über die Eigenständigkeit der Dissertation

Ich versichere, dass ich die vorliegende Arbeit mit dem Titel "Microstructural Changes and Intermetallic Compound Formation in Metallic Bilayers" selbstständig vefasst und keine anderen als die angegebenen Quellen und Hilfsmittel benutzt habe; aus fremden Quellen entnommene Passagen und Gedanken sind als solche kenntlich gemacht.

Declaration of Authorship

I hereby certify that the dissertation entitled "Microstructural Changes and Intermetallic Compound Formation in Metallic Bilayers" is entirely my own work except where otherwise indicated. Passages and ideas from other sources have been clearly indicated.

Stuttgart, den 15. Juli 2016

(Paul J. Rossi)